The permeability of magma mush

ELOISE MARIE BRETAGNE

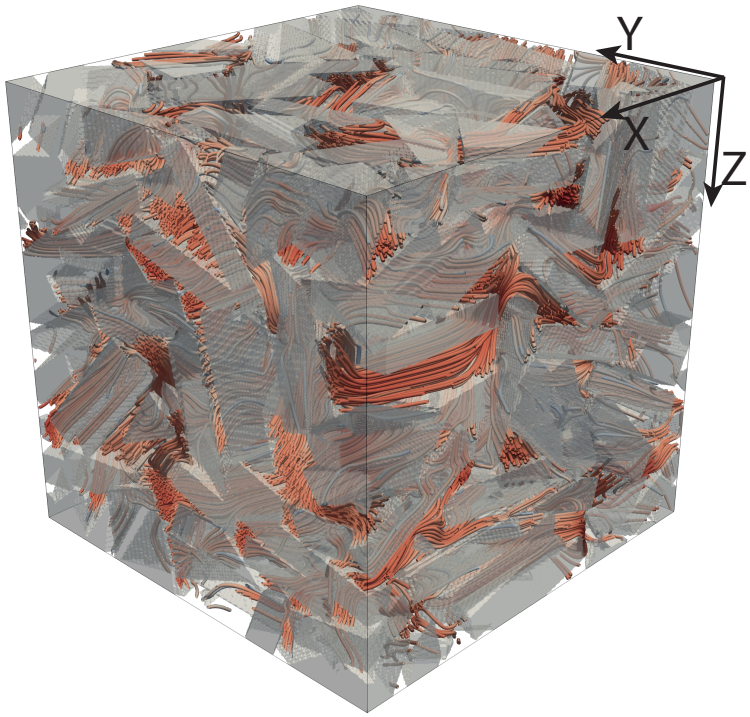

The permeability of magma mush

Verification of a permeability model using numerical and analogue methods

Eloïse Bretagne

This thesis is submitted in partial fulfilment of the requirements for the degree of Doctor of Philosophy at Durham University

Department of Earth sciences

University of Durham

January 2023

Abstract

Models for the evolution of magma mush zones are of fundamental importance for understanding magma storage, differentiation in the crust, and melt extraction processes that prime eruptions. Mush mobilisation and melt segregation are predominant mechanisms that control mush evolution yet are to date still insufficiently understood and models for these are poorly constrained. These models are underpinned by calculations of the permeability of the evolving crystal frameworks in the mush, which controls the rate of melt movement relative to crystals. To date, no mush permeability model accounts for the shape of the crystals that form the crystal-framework in the mush. Herein, we assume that mush crystals are approximately cuboidal, and using that geometric approximation, we present new models for the permeability of mush in which crystal shape parameters are a key input. First, we present an extension of the Kozeny-Carman permeability law specifically for crystal packs at their maximum packing, for which the axis lengths of the crystals are the primary input. Second, we present a model for the evolution of magma mush permeability that is valid from maximum packing down to low melt fractions, ideal for simulating permeability as mush crystalises. In all cases we use a combination of numerical approaches to generate packs of cuboids for analysis, and experimental approaches to create digital 3D scans of anisotropic crystal shapes as an analogue for crystal mush. Using a combination of Avizo 3D image analysis, and a lattice-Boltzmann simulation technique, we constrain the permeability of both the numerical and experimental samples; these data then validate our models across a wide range of parameter space applicable to real magma mush. Furthermore, we propose and validate innovative solutions for permeability that can be found using only 2D data (for example, using a thin section scan), which is useful for common situations where full 3D information may not be available for analysis. In general, our results show that if we consider melt percolation in magma mush akin to fluid flow through porous media, the complexity and anisotropy are well represented by the specific surface area of the crystals. Knowledge of the crystal shape and size are essential variables in our proposed permeability model, unless the mush displays overgrowth textures at low melt fraction, in which case the effect of shape becomes less important. Our results have key implications for melt extraction timescales and cumulate textures as well as for crustal melt segregation processes and reactive flow on the scale of mush reservoirs.

Table of contents

List of figures

List of tables

Declaration

I declare that this thesis, which I submit for the degree of Doctor of Philosophy at Durham University, is my own work, except where acknowledgement is made in the text, and not substantially the same as any work which has previously been submitted at this or any other university for any degree, diploma or other qualification.

Acknowledgements

Firstly, I would like to thank my supervisors for taking a chance on me when they accepted me as their PhD student, for fostering a thought-provoking environment and pushing me out of my comfort zone (in a good scientific way). And, of course, for all the support you have provided me over the years, be it answering all my questions at all times of the day or providing moral support in any way.

Kate, thanks for inspiring me to start the PhD and, although the project has changed a lot since we first got the funding, thanks for staying involved being part of the adventure. Although I am very glad you are fulfilled at Strathclyde, the department misses its 3D imaging expert.

Fabian, thanks for taking me under your wing and shaping the project as we see it today. I didn't believe that we would not step into the lab again after covid and am very happy that you insisted we go in a different direction "just in case". Thank you for our weekly inspiring discussions, for the enormous amount of energy you spend supporting me and for being supportive throughout the highs and the lows.

Jérémie, you joined us towards the end, but are no less important because of it. Thank you for all the help with the numerical simulations and for taking the time to explain it step by step to me. For our long and easily side-tracked discussions in Munich and all the help with the dilatometer; for my by-night tour of Munich and for showing Anabelle and I the Eisbach.

Thanks to the "mush group" for welcoming me even though I am a bit on the fringe of petrology and for all the fun we had at the mush-fest. Madeleine, Alex, Martin, Charline, Amanda, Gemma and Katie, thank you for the inspiring thought-provoking discussions and patiently answering all my questions about geochemistry. Special thanks go to Madeleine for being so patient with us and being a voice of reason for all our ideas for applications. And to Martin for indulging numerous chats about crystal shape and our different definition of aspect ratio.

Thanks everyone at LMU at made me feel welcome and the numerous coffee breaks. Thanks to Kai for the on-the-spot analysis and subsequent chats.

A big thank you to friends in the department for all the chats, drinks, fun and general feeling of belonging that we all fostered. Thanks to Simon, Guillaume, Mathieu, Katy, Miles, Tom, Chris, Jack, Erin, Dimitrios, Madeleine, Olly, Bob, Anabelle, Tammy, Nuno, Juan and more. Special thanks to Emma for hosting our plants when we didn't have a garden, to Tim for the happy coincidence of sharing two universities, to Wardy for trusting me to cut your hair in the garden, to Ilaria for many things but mostly for being such a good friend, and to Sarah for the

same reasons. And finally, to Tara, my Masters buddy. All of you have shaped my experience in Durham and you impact on my life will always stay with me.
Special shout out to my bay buddies, our girly bay was the best! Lena, Katharine, Rebecca, Pierre-Yves, Jack and Ayu: best procrastination endowment ever!
Special thanks to Charline and Ariane for your strong friendship and support, especially over the last few months. I am so glad you are in my life.
A heartfelt thank you, Kate, for all the support (#Tony), the yoga and the fun we had in Musgrave. We had two great years as housemates, and I still can't believe we didn't realise the top floor had no insulation. Thanks for putting up with me for this time. Stuck the three of us in Musgrave due to covid will always be the most unbelievable thing I have lived through. Our lunches in the garden, all the packages, running, yoga with Claire, painting Christmas baubbles two weeks before handing in… all these evoke warm memories of times shared. Can't wait to visit you in Oslo. The fact that you have your own name for my cat says it all.
To you Liz, thank you for the unfailing support you give me in all aspects of my life and for the energy you bring me. Thanks for those precious moments knitting on the beach last summer and your loving outrage in my place. I look forward to enjoying your friendship for many years to come.
An enormous thanks to Will and Hannah for all the great times in the pub, for sharing a love of fantasy and sewing. Special thanks for being Hester's foster parents when we disappear or don't have a house. To many more drinks and books!
Paola, Loïc and little Iris, thank you for all you have done for me. We grew so close so fast, I sometimes I can't believe you arrived in Durham in 2019. Thanks for lending us your house when we had none, for all the pizza and impromptu dinners, apéritif in the garage, for looking after me so well and you unflinching belief in me. Friendship with you is so easy and one I will always treasure. I can't wait to see Iris grow up and all the adventures that still await.
Lastly, a big thank you to my family, for all the support throughout my life. You have shaped the person I am today more than anyone else and for that I love you. You took a chance on me when I moved to the UK and it worked out for the best. Sophie, thank you for being so patient with me and for being so close, to the point of joining me in the UK. And thank you to Sean for the support and love you bring to my life. You know how much you mean to me.

Nomenclature

Nomenclature of symbols and abbreviations used throughout the thesis

ϕ	packing volume fraction
ϕ'	maximum packing fraction
ϕ_m	porosity, also $1-\phi$
ϕ_τ	porosity value of onset of yield strength, $\phi_\tau = 0.8\phi$
k	permeability
k_s	Stokes permeability
k_r	Reference permeability
s	Specific surface area
a, b, c	Independent orthogonal axes of cuboid
R	radius
r_1	Aspect ratio, $r_1 = c/a$
r_2	Aspect ratio, $r_2 = a/b$
C	Constant, usually $C = 5$
F_1	Feret diameter
F_2	Feret diameter
u	Fluid velocity
∇p	Pressure gradient (over height)
μ	Fluid viscosity

Chapter 1 : Introduction and wider setting

Over the last three decades, the magmatic research community has evolved from considering upper-crustal magmatic processes as originating in melt filled magma chambers, to a new approach on the scale of the entire crust, which better explains the petrological, geochemical, geophysical, volcanological and geological phenomena we associate to magma storage (Fig. 1.1A, 1.1B; Cashman et al., 2017; Cashman & Sparks, 2017). The notion of a Trans-Crustal Magmatic System (TMCS) was introduced, in which the crust is conceived as comprising a large-scale nominally open-system magma reservoir (e.g. De Paolo, 1981; Anderson, 1976; Humphreys et al., 2006) and has all the dynamic features required to explain fractionation and differentiation (Hildreth, 1981; Hildreth & Moorbath, 1988; Jackson et al., 2018; Annen et al., 2006, Sparks et al., 2019).

In the new paradigm described above, crustal reservoirs are thought to be dominated by crystal mush, a mixed system of magmatic melt and crystals where the crystals form a rigid framework through which the melt is distributed (Marsh, 1989, Bachmann & Bergantz, 2008; Cashman et al., 2017; Sparks et al., 2019). Mush is characterised by a relatively high crystal content. The lower bound of this crystal content in a mush is defined by the crystallinity above which crystal interactions, and the upper limit is when the magma is fully crystallised. This is a very broad, and potentially a poorly defined, definition, and mush is commonly considered to have at least upwards of 40 vol.% crystals (Fig. 1.1C; Marsh, 1981; Bachmann & Bergantz, 2004; Cashman et al., 2017). The consequence of this view of high-crystallinity magma reservoirs is that the viscosity of mush reservoirs is high (Marsh, 1981; Wager et al., 1960) and, as defined, mush as a whole is not able to flow, due to the crystal content exceeding the Rigid Percolation Threshold of Vigneress et al. (1996; Fig. 1.1C).

Along with this new conceptual understanding of crustal mush storage, new conceptual models to account for magma evolution and volcanic processes need to be addressed and developed. Outstanding questions that we are interested in here revolve around the general antithesis of mush being immobile due to its high viscosity. The direct observation that crystal-rich magmas do erupt is in contradiction with the rheological picture of mush as ‘locked’ and immobile (e.g. Burgisser & Bergantz, 2011; Huber et al., 2011; Zieg & Marsh, 2012; Neave et al., 2012; Bergantz & Schleicher, 2015, Bergantz et al., 2017). Here, we are therefore interested in investigating (1) the mechanisms involved in unlocking a mush to make it able to flow; and (2)

the physical processes involved in melt segregation associated with crystal-poor silicic eruptions.

Several mechanisms have been suggested to 'unlock' (the term 'locked' while speaking of the rheology of mushes is attributed to Marsh (1991)) a physically immobile mush (e.g. Sparks et al. 2019). Fluidisation of the full or partial crystal load can occur with one or a combination of the following physical processes: (1) basal intrusion of melt that 'rejuvenates' or 'defrosts' the mush and causes desegregation of the mush structure (e.g. Huppert et al., 1988; Huang et al., 2015; Cooper et al., 2016) sometimes even leading to large-scale overturn of the mush (e.g. Girard & Stix, 2009; Burgisser & Bergantz, 2011; Huber et al., 2012; Schleicher et al., 2016; Schleicher & Bergantz, 2017); (2) volatile exsolution into bubbles nucleating in the interstitial melt and the subsequent growth of bubbles that pushes aside the crystals of the mush and decreases the bulk viscosity and strength (e.g. Ruprecht et al., 2008; Bachmann & Bergantz, 2006); and (3) external forcing in the form of e.g. regional tectonics apply shear to the mush, the rigid crystal framework is damaged or localised and makes the mush able to flow (e.g Clements & Petford, 1999; Holtzman et al. 2003; Sawyer, 2000).

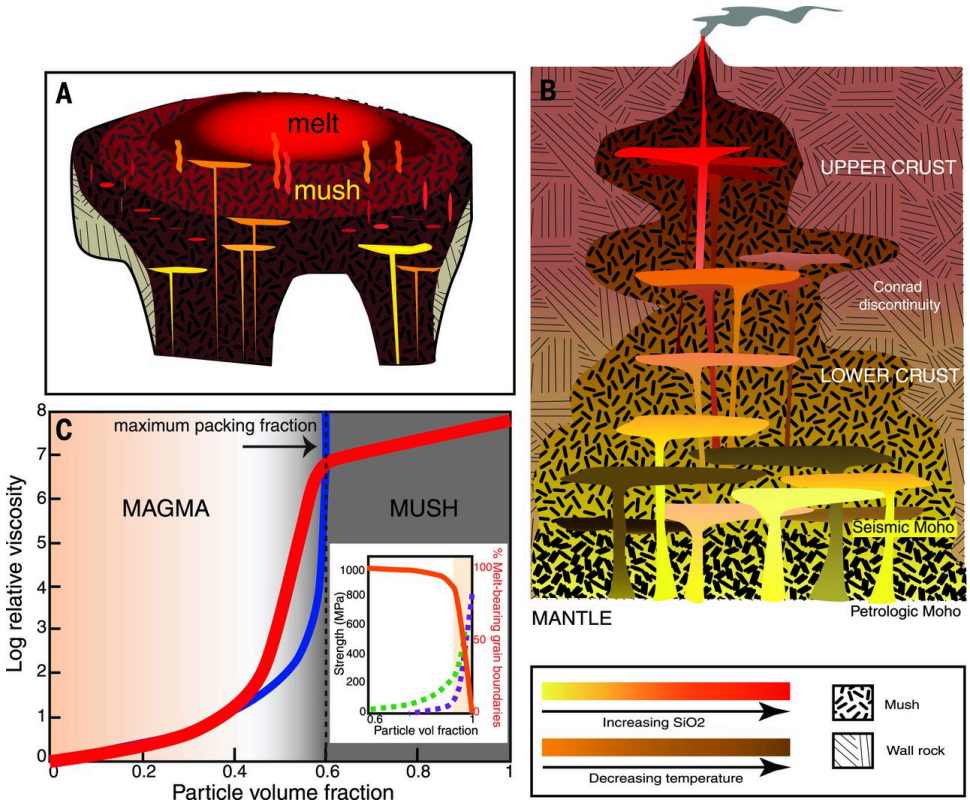

Figure 1.1: Illustration of the conceptual change in our understanding of magmatic systems. (A) represents the classic concept of the balloon shaped magma chamber filled with melt where crystals rain out to the bottom of the chamber. (B) is a schematic overview of the architecture of the TCMS, a crustal scale open system

characterised by the relatively low melt content. (C) shows the rheology of the mush, how the bulk viscosity and strength is affected by the crystal content; the blue curve is calculated using the formulation detailed in Costa et al. (2009) whereas the red one is assuming a crystal fraction of 0.6 and uses the classical Roscoe-Einstein formulation (Figure from Cashman et al. (2017))

By contrast, crystal-poor silicic eruptive materials are the product of melt segregation from the mush and not of wholesale mush unlocking (Bachmann & Bergantz 2004; Hildreth & Wilson, 2007; Wilson et al. 2021). The exact physical processes controlling melt segregation are debated (c.f. Holness 2018; Liu & Lee 2021), but predominant mechanisms put forward are: (1) magma recharge: the interstitial melt is mobilised as a batch of hotter magma enters the system (e.g. Charlier et al., 2007; Bergantz et al., 2015; Sato et al., 2017); (2) gas filter pressing: gas exsolution in the interstitial melt drives the melt out of the inter-crystal space (e.g. Bacon, 1986; Hartung et al, 2017); and (3) external forcing: the mush is subjected to a local stress field, for example, tearing and slumping of the mush on the extremities of the reservoir (Philpotts et al., 1996; Marsh, 1996; Philpotts & Dickson, 2002; Humphreys & Holness, 2010).

At this point, we note that the mechanisms for mush mobilisation and melt segregation are similar, but the latter are likely to be lesser in intensity in contrast to the former, where the rigid crystal framework needs to be broken up to entrain the crystals in the flow (e.g. Bachmann & Bergantz, 2004). For melt segregation, the crystal framework needs to remain rigid so that the melt can percolate through the inter-crystal space (e.g. Marsh, 1989; Sparks et al., 2019). The mobilisation of mush and melt are akin to flow in granular media (i.e. the crystals can move with the flow) and flow through porous media (i.e. the rigid framework of crystals is static), respectively. In this work, we focus on the melt segregation, simulating the flow of melt through the inter-crystal space as a flow through porous media.

While melt extraction remains a poorly understood process (Bachmann et al. 2007; Holness 2018), all possible mechanisms are underpinned by prediction of the permeability of the mush. Herein, we define the permeability of a mush as the measure of the efficiency with which melt can flow through the rigid crystal framework that forms the mush. For here on out, we refer to this as the 'mush permeability'. The mush crystals are considered analogous to porous media, and we model the permeability using principles of fluid dynamics for porous materials as well as percolation theory.

Understanding the flow of melt and the permeability of the mush is important for predicting melt migration and, in a broader sense, models for the evolution of these magma mush zones are of fundamental importance for magma storage timescales, differentiation in the crust, and

understanding melt extraction processes that prime eruptions (Bachmann & Bergantz, 2004; Annen, 2009; Cashman et al. 2017; Jackson et al. 2018; Sparks et al. 2019). Percolation of melts through mush can be reactive, resulting in a distillation column effect at crustal scales, and dynamic magma evolution (Annen et al., 2006; Cashman et al., 2017; Jackson et al., 2018; Sparks et al., 2019). The progression of both melt movement, and of melt-crystal reactions are rate-limited by the percolation speed through the mush. In turn, the speed of melt percolation is controlled by the permeability of the solid framework of crystals between which melts migrate (e.g. Liu and Lee, 2021). Models for crystallization or compaction predict that the permeability of mush evolves with time as melt volume fraction evolves (Bachmann and Bergantz, 2004; Jackson et al., 2018), however the specifics of this relationship remain poorly constrained.

While all crustal-scale models require permeability to compute fluxes (Bachmann & Bergantz, 2004; Jackson et al. 2018), there has been relatively little work to constrain the permeability beyond first-order scaling approaches. Previous models have used simple scaling laws for the permeability that assume all crystals are spherical and can be defined by their radius (e.g. Bachmann & Bergantz, 2004; Huber et al. 2010; Hartung et al. 2019; Floess et al. 2019; Pistone et al. 2020). However, it is reasonable to suggest that the non-spherical crystal shape exerts a first-order control on the permeability of the mush and should be taken into account for flow models.

This thesis is structured around a series of three papers that are situated in the current global context and understanding of mush mobilisation. Herein, we aim to validate a shape-dependent permeability model for a magma mush, where the crystals are numerically represented by square-edged cuboids. Therein, we explore the first-order effect of crystal aspect ratio on mush permeability for the first time. The model consists of a generalisation of the Kozeny-Carman law and suggests a better shape descriptor in the form of the measurement of the specific surface area of the crystal phase instead of requiring *a priori* intimate knowledge of the crystal shape.

We then aim to broaden the validity of the permeability model to natural anisotropic crystal shapes by using analogues materials for mush. The mush is represented here by x-ray computed tomography (ct) scans of readily available anisotropic and anisometric particles: cake topping confectionary. We use the complex anisotropic solids to test how well cuboids can represent

shapes occurring in natural mush and the potential sources of the shape information (i.e. 3D scans of mush or a 2D view via a thin section).

Finally, we aim to validate the permeability model for high crystallinity mushes where the notion of the percolation threshold becomes controlling. This is required to extend the results of this thesis to low melt fractions as mush reservoirs crystallise to high degrees of crystallinity. We test this 'low melt fraction model' on overgrown cuboids, here representing cumulate overgrowth in natural mushes.

References

Anderson, A.T., 1976. Magma mixing: petrological process and volcanological tool. *Journal of Volcanology and Geothermal Research*, *1*(1), pp.3-33

Annen, C., Blundy, J.D. and Sparks, R.S.J., 2006. The genesis of intermediate and silicic magmas in deep crustal hot zones. *Journal of Petrology*, *47*(3), pp.505-539.

Annen, C., 2009. From plutons to magma chambers: Thermal constraints on the accumulation of eruptible silicic magma in the upper crust. *Earth and Planetary Science Letters*, *284*(3-4), pp.409-416.

Bachmann, O. and Bergantz, G.W., 2004. On the origin of crystal-poor rhyolites: extracted from batholithic crystal mushes. *Journal of Petrology*, *45*(8), pp.1565-1582.

Bachmann, O. and Bergantz, G.W., 2006. Gas percolation in upper-crustal silicic crystal mushes as a mechanism for upward heat advection and rejuvenation of near-solidus magma bodies. *Journal of Volcanology and Geothermal research*, *149*(1-2), pp.85-102.

Bachmann, O. and Bergantz, G.W., 2008. Rhyolites and their source mushes across tectonic settings. *Journal of Petrology*, *49*(12), pp.2277-2285.

Bachmann, O., Oberli, F., Dungan, M.A., Meier, M., Mundil, R. and Fischer, H., 2007. 40Ar/39Ar and U–Pb dating of the Fish Canyon magmatic system, San Juan Volcanic field, Colorado: evidence for an extended crystallization history. *Chemical Geology*, *236*(1-2), pp.134-166.

Bacon, C.R., 1986. Magmatic inclusions in silicic and intermediate volcanic rocks. *Journal of Geophysical Research: Solid Earth*, *91*(B6), pp.6091-6112.

Bergantz, G.W., Schleicher, J.M. and Burgisser, A., 2015. Open-system dynamics and mixing in magma mushes. *Nature Geoscience*, *8*(10), pp.793-796.

Bergantz, G.W., Schleicher, J.M. and Burgisser, A., 2017. On the kinematics and dynamics of crystal-rich systems. *Journal of Geophysical Research: Solid Earth*, *122*(8), pp.6131-6159.

Burgisser, A. and Bergantz, G.W., 2011. A rapid mechanism to remobilize and homogenize highly crystalline magma bodies. *Nature*, *471*(7337), pp.212-215.

Cashman, K.V., Sparks, R.S.J. and Blundy, J.D., 2017. Vertically extensive and unstable magmatic systems: a unified view of igneous processes. *Science*, *355*(6331), p. 3055.

Charlier, B.L.A., Bachmann, O., Davidson, J.P., Dungan, M.A. and Morgan, D.J., 2007. The upper crustal evolution of a large silicic magma body: evidence from crystal-scale Rb–Sr isotopic heterogeneities in the Fish Canyon magmatic system, Colorado. *Journal of Petrology*, *48*(10), pp.1875-1894.

Clemens, J.D. and Petford, N., 1999. Granitic melt viscosity and silicic magma dynamics in contrasting tectonic settings. *Journal of the Geological Society*, *156*(6), pp.1057-1060.

Cooper, G.F., Wilson, C.J., Millet, M.A. and Baker, J.A., 2016. Generation and rejuvenation of a supervolcanic magmatic system: a case study from Mangakino volcanic centre, New Zealand. *Journal of Petrology*, *57*(6), pp.1135-1170.

DePaolo, D.J., 1981. Trace element and isotopic effects of combined wallrock assimilation and fractional crystallization. *Earth and planetary science letters*, *53*(2), pp.189-202.

Floess, D., Caricchi, L., Simpson, G. and Wallis, S.R., 2019. Melt segregation and the architecture of magmatic reservoirs: insights from the Muroto sill (Japan). *Contributions to Mineralogy and Petrology*, *174*(4), pp.1-15.

Girard, G. and Stix, J., 2009. Buoyant replenishment in silicic magma reservoirs: Experimental approach and implications for magma dynamics, crystal mush remobilization, and eruption. *Journal of Geophysical Research: Solid Earth*, *114*(B8).

Hartung, E., Caricchi, L., Floess, D., Wallis, S., Harayama, S., Kouzmanov, K. and Chiaradia, M., 2017. Evidence for residual melt extraction in the Takidani Pluton, Central Japan. *Journal of Petrology*, *58*(4), pp.763-788.

Hartung, E., Weber, G. and Caricchi, L., 2019. The role of H2O on the extraction of melt from crystallising magmas. *Earth and Planetary Science Letters*, *508*, pp.85-96.

Hildreth, W. and Moorbath, S., 1988. Crustal contributions to arc magmatism in the Andes of central Chile. *Contributions to mineralogy and petrology*, *98*(4), pp.455-489.

Hildreth, W. and Wilson, C.J., 2007. Compositional zoning of the Bishop Tuff. *Journal of Petrology*, *48*(5), pp.951-999.

Hildreth, W., 1981. Gradients in silicic magma chambers: implications for lithospheric magmatism. *Journal of Geophysical Research: Solid Earth*, *86*(B11), pp.10153-10192.

Holness, M.B., 2018. Melt segregation from silicic crystal mushes: a critical appraisal of possible mechanisms and their microstructural record. *Contributions to Mineralogy and Petrology*, *173*(6), pp.1-17.

Holtzman, B.K., Kohlstedt, D.L., Zimmerman, M.E., Heidelbach, F., Hiraga, T. and Hustoft, J., 2003. Melt segregation and strain partitioning: Implications for seismic anisotropy and mantle flow. *Science*, *301*(5637), pp.1227-1230.

Huang, H.H., Lin, F.C., Schmandt, B., Farrell, J., Smith, R.B. and Tsai, V.C., 2015. The Yellowstone magmatic system from the mantle plume to the upper crust. *Science*, *348*(6236), pp.773-776.

Huber, C., Bachmann, O. and Manga, M., 2010. Two competing effects of volatiles on heat transfer in crystal-rich magmas: thermal insulation vs defrosting. *Journal of Petrology*, *51*(4), pp.847-867.

Huber, C., Bachmann, O. and Dufek, J., 2011. Thermo-mechanical reactivation of locked crystal mushes: Melting-induced internal fracturing and assimilation processes in magmas. *Earth and Planetary Science Letters*, *304*(3-4), pp.443-454.

Huber, C., Bachmann, O., Vigneresse, J.L., Dufek, J. and Parmigiani, A., 2012. A physical model for metal extraction and transport in shallow magmatic systems. *Geochemistry, Geophysics, Geosystems*, *13*(8).

Humphreys, M.C.S. and Holness, M.B., 2010. Melt-rich segregations in the Skaergaard Marginal Border Series: Tearing of a vertical silicate mush. *Lithos*, *119*(3-4), pp.181-192.

Humphreys, M.C., Blundy, J.D. and Sparks, R.S.J., 2006. Magma evolution and open-system processes at Shiveluch Volcano: Insights from phenocryst zoning. *Journal of Petrology*, *47*(12), pp.2303-2334.

Huppert, H.E. and Sparks, R.S.J., 1988. The generation of granitic magmas by intrusion of basalt into continental crust. *Journal of Petrology*, *29*(3), pp.599-624.

Jackson, M.D., Blundy, J. and Sparks, R.S.J., 2018. Chemical differentiation, cold storage and remobilization of magma in the Earth's crust. *Nature*, *564*(7736), pp.405-409.

Liu, B. and Lee, C.T., 2021. Fast melt expulsion from crystal-rich mushes via induced anisotropic permeability. *Earth and Planetary Science Letters*, *571*, p.117113.

Marsh, B.D., Gunnarsson, B., Congdon, R. and Carmody, R., 1991. Hawaiian basalt and Icelandic rhyolite: indicators of differentiation and partial melting. *Geologische Rundschau*, *80*, pp.481-510.

Marsh, B.D., 1989. Magma chambers. *Annual Review of Earth and Planetary Sciences*, *17*(1), pp.439-472.

Marsh, B.D., 1996. Solidification fronts and magmatic evolution. *Mineralogical Magazine*, *60*(398), pp.5-40.

Neave, D.A., Fabbro, G., Herd, R.A., Petrone, C.M. and Edmonds, M., 2012. Melting, differentiation and degassing at the Pantelleria volcano, Italy. *Journal of Petrology*, *53*(3), pp.637-663.

Philpotts, A.R. and Dickson, L.D., 2002. Millimeter-scale modal layering and the nature of the upper solidification zone in thick flood-basalt flows and other sheets of magma. *Journal of Structural Geology*, *24*(6-7), pp.1171-1177.

Philpotts, A.R. and Carroll, M., 1996. Physical properties of partly melted tholeiitic basalt. *Geology*, *24*(11), pp.1029-1032.

Pistone, M., Baumgartner, L.P., Bégué, F., Jarvis, P.A., Bloch, E., Robyr, M., Müntener, O., Sisson, T.W. and Blundy, J.D., 2020. Felsic melt and gas mobilization during magma solidification: An experimental study at 1.1 kbar. *Frontiers in Earth Science*, *8*, p.175.

Ruprecht, P., Bergantz, G.W. and Dufek, J., 2008. Modeling of gas-driven magmatic overturn: Tracking of phenocryst dispersal and gathering during magma mixing. *Geochemistry, Geophysics, Geosystems*, *9*(7).

Sato, H., Holtz, F., Botcharnikov, R.E. and Nakada, S., 2017. Intermittent generation of mafic enclaves in the 1991–1995 dacite of Unzen Volcano recorded in mineral chemistry. *Contributions to Mineralogy and Petrology*, *172*(4), pp.1-19.

Sawyer, E.W., 2000. Grain-scale and outcrop-scale distribution and movement of melt in a crystallising granite. *Earth and Environmental Science Transactions of the Royal Society of Edinburgh*, *91*(1-2), pp.73-85.

Schleicher, J.M. and Bergantz, G.W., 2017. The mechanics and temporal evolution of an open-system magmatic intrusion into a crystal-rich magma. *Journal of Petrology*, *58*(6), pp.1059-1072.

Schleicher, J.M., Bergantz, G.W., Breidenthal, R.E. and Burgisser, A., 2016. Time scales of crystal mixing in magma mushes. *Geophysical Research Letters*, *43*(4), pp.1543-1550.

Sparks, R.S.J., Annen, C., Blundy, J.D., Cashman, K.V., Rust, A.C. and Jackson, M.D., 2019. Formation and dynamics of magma reservoirs. *Philosophical Transactions of the Royal society A*, *377*(2139), p.20180019.

Sparks, R.S.J. and Cashman, K.V., 2017. Dynamic magma systems: Implications for forecasting volcanic activity. *Elements*, *13*(1), pp.35-40.

Vigneresse, J.L., Barbey, P. and Cuney, M., 1996. Rheological transitions during partial melting and crystallization with application to felsic magma segregation and transfer. *Journal of Petrology*, *37*(6), pp.1579-1600.

Wager, L.R., Brown, G.M. and Wadsworth, W.J., 1960. Types of igneous cumulates. *Journal of Petrology*, *1*(1), pp.73-85.

Wilson, C.J., Cooper, G.F., Chamberlain, K.J., Barker, S.J., Myers, M.L., Illsley-Kemp, F. and Farrell, J., 2021. No single model for supersized eruptions and their magma bodies. *Nature Reviews Earth & Environment*, *2*(9), pp.610-627.

Zieg, M.J. and Marsh, B.D., 2012. Multiple reinjections and crystal-mush compaction in the Beacon Sill, McMurdo Dry Valleys, Antarctica. *Journal of Petrology*, *53*(12), pp.2567-2591.

Costa, A., Caricchi, L. and Bagdassarov, N., 2009. A model for the rheology of particle-bearing suspensions and partially molten rocks. *Geochemistry, Geophysics, Geosystems*, *10*(3).

Chapter 2 : Methodology

2.1 Novel 3D data acquisition approach

Textures of mushes and igneous rocks are generally studied using thin sections, implicitly assuming the 2D view is representative of the anisotropy and complexity of a natural rock sample (Carlson and Denison, 1992; Holness, 1997). There are several methods to infer or observe the true 3D view. These include indirect methods such as stereological conversion from 2D observations to 3D observations by means of understanding the probability of a particular 2D observation (e.g. Higgins, 2000; Mangler et al., 2022). But these also include more direct methods: (1) sequential sectioning of a 3D sample into successive 2D slices; and (2) X-ray computed tomography. While the former method has been applied to crystal-rich samples (e.g. Duchêne et al., 2008), it is both destructive of the entire sample and requires extreme and time-consuming precision in the sectioning methodology in order to acquire exactly locatable 2D slices. For these reasons, here we only discuss the latter technique: X-ray computed tomography.

X-ray computed tomography enables acquisition of high-resolution volumetric information of the internal structure of opaque materials in a non-destructive manner. Over the last decade or more, working with 3D data has become commonplace in Earth Sciences and is an essential tool in many branches of natural sciences (Cnudde and Boone, 2013): e.g. 3D morphological characterisation of the anatomy of micro-fossils (Friis et al., 2015; Lindgren et al., 2018; Voeten et al., 2018) or multi-scale 3D knowledge of the pore pathways in a porous media (Munawar et al., 2018). In volcanology, volumetric analysis of rock samples provides insights into magma evolution, be it crystallisation and degassing processes (Moretti et al., 2019), bubble growth in magma (Baker et al., 2012), and magma rheology (Pistone et al., 2015). While 3D analysis and data manipulation are well established for static data (i.e. rock or analogue samples), the acquisition procedure can also capture in situ dynamic processes, taking it to 4D (e.g. Colombier et al., 2020; Arzili et al., 2019; Polacci et al., 2018; Tripoli et al., 2019; Le Gall et al., 2021; Wadsworth et al., 2017; Dobson et al., 2020).

Among all the geoscientific problems for which 3D data is most important, fluid flow in porous media is perhaps the most crucial. Flow of fluids in a natural or synthetic material is ultimately controlled by the permeability, a parameter intrinsic to the material that defines the ability of a porous media to transmit fluids (e.g. Keller et al., 2011; Jackson et al., 2018). While easy

enough to measure, the quantification of the permeability via a predictive model is not trivial. The difficulty is in expressing the complexity and anisotropy of the porous system while at the same time proposing a widely applicable model. To achieve this, multi-scale 3D knowledge of the pore pathways in a porous media is crucial to obtain a true spatial comprehension of the pathways that flow can take (e.g. Munawar et al., 2018). The spatial data for pore space can then be accurately distilled to into well-chosen parameters that express the complexity of the media. Key parameters include the crystal/particle shape and size and the volume fractions of solids and void.

Herein, we use numerical 3D domains of particles packed in volumes to represent crystals packed in melts. 3D analysis of the pore network is key to understanding fluid flow and the permeability of natural materials. We use volumetric analysis tools to measure the key scalar and directional, vector quantities that constrain the fluid flow in porous media.

In this chapter, we outline the definition of the key parameters and notions that are used throughout this work. Conventional measuring methodologies are explained as well as details of the analytical procedures.

2.2 Fundamental quantities to constrain fluid flow in natural media

2.2.1. Scalar quantities

Scalar quantities necessary to constrain flow include:

1. Volumetric properties: The volume fraction ϕ of phases, including the crystals in a mush and its counterpart, the melt fraction ϕ_m. In this work, we consider crystal mush as a two-phase system of crystals and melt, such that $\phi_m = 1 - \phi$.
2. Areal properties: The surface area of a phase interface and specific surface area. The latter is defined as the sum of the surface area of all of one phase (e.g. the crystals in mush) divided by the total volume of the domain.
3. Length properties: The size and shape of a phase such as the crystals in mush.

2.2.1.1. Measuring the volume fractions of phases

The relative fractions of a volume that are taken up with each phase present is among the simplest and most important parameters to measure. We define the volume fraction ϕ as the

fraction taken up by the solid phase (in this case the crystals or the crystal analogues). The residual is often termed the porosity but, here, we consider a two-phase system composed of a solid and a fluid phase. Hence, we termed it the melt fraction ϕ_m.

We measure these parameters in a binary file, where the voxels that make up the 3D data are either assigned to the solid or fluid phase. The ratios are computed using an image processing software (either Python or Avizo©) that compares the numbers of voxels assigned to each phase.

2.2.1.2. Measuring the surface area of phases

The surface area of an object can be measured or calculated. The surface area of known geometries such as cylinders, cubes, spheres, etc can be calculated using formulas but these shapes are uncommon in natural materials. In laboratory settings, the parameter can be measured using gas adsorption theory where the number of gas molecules adsorbed by the object is a function of gas pressure, ambient temperature, the molecule species and the size of the reactive surface. When controlling the pressure, temperature and type of gas, the surface area can be measured.

As we are not working with physical samples, rather with numerical 3D renders of magma mush, we compute the surface area of the solid phase, or more specifically, the surface area of the interface between the two phases. We apply a marching cubes algorithm (Lorensen & Cline, 1987) that determines the internal surfaces between particles and the inter-particle pore spaces, but ignores the outer edges of the domain, and outputs the surface area as a count of edge voxels. That count can be converted to a surface area proper knowing the resolution of the 3D data (i.e. the size of one voxel edge).

The surface area of a phase is converted to a specific surface area s by dividing the measured surface area by the total sample volume.

2.2.1.3. Measuring the size of phases

The size of the crystals in the mush are an essential scalar parameter to know to predict the flow of the melt around the crystals (Martys et al. 1994; Wadsworth et al. 2016; Vasseur et al. 2021). In this work we will look at the effect of particle size and shape on the flow, hence, the size descriptor would ideally also express the shape of the objects. There exist several ways to express the size of a 3D object, here we present three most popular ways and discuss their

accuracy and how representative each result is: (1) equivalent spheres, (2) the Feret diameters and (3) the three orthogonal axes of the cuboid encompassing the shape.

In (1), the size of a 3D object can be measured by computing the sphere of equal volume or of equal surface area (Fig. 2.1a). This method accurately expresses the size of the 3D object as a radius, but, however, all notion of the shape of the object (here the crystals) is lost. Few natural materials are made up of perfect spheres, although it is a common approximation when looking at the permeability of natural media (e.g. Bachmann & Bergantz, 2004).

Another option is to use the (2) Feret diameter, which is an average of maximum and minimum lengths in a given orientation, much like measuring the maximum and minimum length of the shadow of the object (Figure 2.1b). To capture a complex 3D shape, this average would itself be averaged over many reorientations (i.e. over many iterations of orientation of the object in 3D space). With reference to previous work (Buckland et al. 2021), we assert that the Feret method provides an incomplete measure of 3D shape for our purposes.

Lastly, the size of any 3D object can be defined by (3) the orthogonal axes that describe the minimum length-scale, the intermediate and the longest length-scale in the object (Fig. 2.1c). Effectively, any geometry is approximated to a cuboid, the size and shape of which is expresses by the three characteristic axes. We define them as such: the small axis a, intermediate axis b and long axis c.

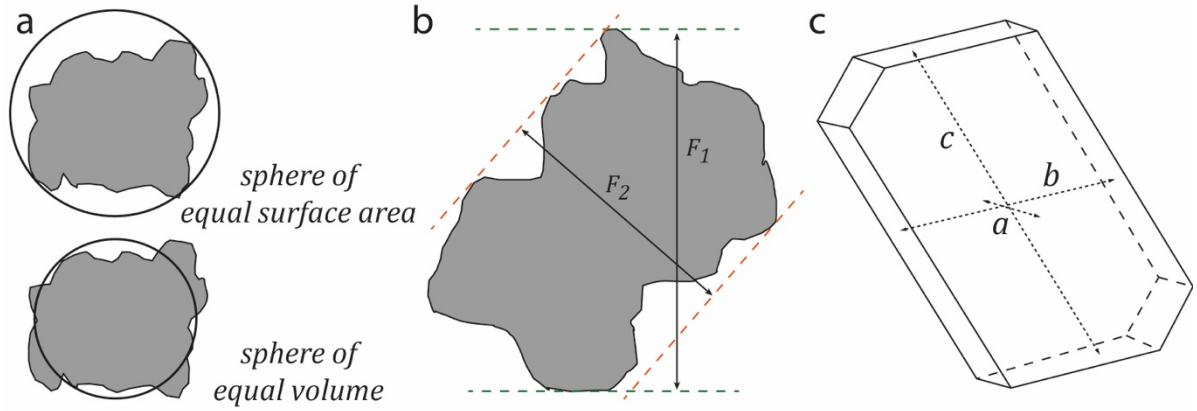

Figure 2.1: Overview of options for measuring the size of a 3D phase object. a) One option is to use the sphere of either equal surface area or of equivalent volume as the 3D object; the results of either are significantly different from one another (inspired from https://basicmedicalkey.com/particle-size-analysis/). b) Another method is using the Feret diameters, the longest and shortest lines that the "shadow" of the shape draws are averaged, much like the maximum and minimum value we could measure with a calliper (inspired from https://www.sympatec.com/en/particle-measurement/glossary/particle-shape/). c) Here, we use a true 3D

shape, using the three orthogonal axes a, b and c. This method is the most accurate at representing cuboidal shapes (figure inspired from Duchêne et al., 2008)

2.2.2 Vector quantities for porous media

To constrain fluid flow in natural materials, we also need to know certain quantities that are directional, quantified in vector space. The principal directional parameter here is the permeability, the measure of the efficiency with which a static medium can transmit fluids. However, another key parameter is the connectivity of the melt fraction (also referred to as pore space in a two-phase system), expressed here as the ratio of the connected melt fraction against the total melt volume.

Others have used other metrics to express the complexity and anisotropy of the pores of natural media (equivalent to the melt fraction we use here), such as the geometry of the pore space, inter-pore aperture size, anisotropy and tortuosity of the pore network (e.g Blower, 2001; Le Pennec et al., 2001; Bernard et al., 2007; Yokoyama and Takeuchi, 2009; Wright et al., 2009, Degruyter et al., 2010, Wright and Cashman, 2014). These quantities, however, require intimate knowledge of the pore network and are hard to generalise without losing precision and the intricacies of the natural material. Instead, we chose to use the pore space connectivity as simply a function of the bulk porosity and does not require quantification of pore anisotropy (Colombier et al., 2017; 2020).

2.2.2.1. Connectivity of pore spaces

The connectivity of the melt fraction (or pore space) exerts a first order control on the permeability of a medium (e.g. Rust & Cashman, 2011), making this an essential variable to quantify to model fluid flow in said medium. Particularly, it is the evolution of the connectivity as the melt fraction deceases that we are interested in and more specifically, quantification of the isolated melt pockets at low melt fractions. This last variable is key to understanding the percolation of fluids and will be explored in this work.

Previously, the evolution of the connectivity of pores or melt fraction was expressed as the connected fraction of the pores against the bulk porosity (Klug et al., 2002; Formenti and Druitt, 2003; Bouvet de Maisonneuve et al., 2009; Shea et al., 2012), making the evolution hard to follow. More recently, the connectivity C has been defined as the ratio of the connected pores ϕ_c and the bulk porosity ϕ_{tot}, such that $C = \phi_c/\phi_{tot}$. When $C = 1$, all pores are connected and as ϕ_{tot} decreases, C will drop to zero, indicating that the that the residual

porosity exists as isolated pores. The ratio C is then plotted against the bulk porosity ϕ_{tot} (Shimano and Nakada, 2006; Nakamura et al., 2008, Okumura et al., 2013, Farquharson et al., 2015, Colombier et al., 2017).

Pore network connectivity of physical samples can be measured in the laboratory with the use of a pycnometer, where pore clusters connected to the exterior of the sample are quantified as the connected porosity. Another measure of the connectivity can be performed by saturating the porous sample with water and then measuring the weight difference (Katyo, 1987; Nakaruma et al., 2008). X-ray tomography can also be used for this analysis (Okumura et al., 2008, Song et al., 2001), however, the quality of the imagery would need to be excellent to be able to discern the presence of bubble walls.

Our data in this study is numerical, hence none of the above methods can be applied. We apply a labelling algorithm that detects the connectivity of the pore space (Vasseur & Wadsworth, 2017; inspired from Fiorio & Gustedt, 1996; Wu et al., 2005; Newmann & Ziff, 2001). The algorithm labels clusters of voxels that are interconnected, the connectivity of which is evaluated according to chosen input arguments of voxel neighbourhood (face-face, edge-edge or corner-corner). The labelled clusters are then individually assessed to check for a connection between opposite boundaries of the domain. Clusters that pass this test are recorded and the sum of the connected porosity in one direction (i.e. one set of opposite edges of the domain) is averaged over the total size of the domain and output as the directional connectivity of the pore network.

2.2.2.2. Permeability: theory overview

The permeability is an intrinsic parameter, independent of any external forces, specific to each material and is an easy enough property to measure on physical samples in the laboratory. The governing equation for fluid flow through porous media is expressed by Darcy's law, which states that the velocity of the fluid flowing though the material υ is a function of the permeability k, the pressure gradient ∇P and the viscosity of the fluid μ (Darcy, 1856).

$$\upsilon = \frac{k}{\mu} \nabla P \qquad \text{Eq. 1}$$

The rock sample, usually a core, is subjected to a known pressure gradient and a flow of fluid of known viscosity. The velocity of the fluid is measured, and the permeability is calculated using Darcy's law (Eq. 1).

In theory, the permeability is calculated in the same way as in the lab, using Darcy's equation, however, the velocity field that describes the flow of the fluid through the porous material is very complex to express mathematically. There are several approaches to the mathematical dilemma depending on the scale of the system considered and this dictates whether fluid flow is considered as a continuum, a probability function or as a discrete finite element model. The latter is usually reserved for the atomic/molecule scale where each the flow is described by the behaviour of each individual molecule of the fluid. We will not be going into any more detail about this approach as it is not one we consider here for the permeability of magmas. We will, however, go into more detail on the two other ways of considering the flow and specifications of how these were applied can be found in the next section (section 2.4)

For the large-scale approach, fluid flow is considered a continuum, where variables such as pressure, viscosity, density, fluid velocity, etc vary smoothly over time and space. Flow is described by the Navier Stokes equations, a combination of the laws for conservation of mass and momentum. The complex equations are composed of a viscous and an inertial term, and on account of both these terms, the equations have never been fully integrated, hence, there exists no general solution. Simplified versions of the equations are routinely used to solve physical problems such as flow of fluid through a known geometry (e.g. a pipe), modelling weather patterns or ocean currents to name some applications.

The other approach we will discuss here is applied to the intermediate scale, where the fluid is not considered as a varying entity but in terms of the kinetics of the fluid. The flow is described as the probability of finding a fluid particle at a given time and place. The probability function is governed by the Boltzmann equation but exists in a very complex six-dimensional space, which renders the equation very complex for application.

Due to the complexity of the Boltzmann equation, a minimal form of the kinetic equation was suggested where the fluid is defined as particles set in a fictitious lattice that confines the motion and inter-particle interactions in time and space (Succi & Benzi, 1991; Chen & Doolen, 1998). The effective decrease in degrees of freedom for motion and time reduces the complexity of the Boltzmann equation and thereby increases the applications of, now called, Lattice-Boltzmann approach. Necessary conditions in term of the range of motion for the particles still needs to be met to fulfil the basic conservation laws of mass, momentum and energy (He & Luo, 1997; Chen & Doolen, 1998).

2.2.2.3. Quantification of the velocity field of fluid flow using numerical methods and subsequent permeability calculation

In this study, we used several numerical methods to measure the scalar and directional quantities essential to know to model the flow of melt around cumulate crystals in a magma mush. Two different methods are used in particular to "measure" the permeability of numerical samples: we use Avizo©, a 3D analysis software by Thermofisher, which has an integrated permeability module and LBFlow, a Lattice-Boltzmann flow simulator adapted to Python (Llewellin 2010a, b).

In Avizo©, the permeability is obtained by solving the Navier-Stokes for velocity and implementing the resulting into Darcy's law to obtain the permeability. The N-S equations are simplified to the Stokes equations by considering the following statements: (1) the fluid at a constant density, meaning the fluid is incompressible; (2) the fluid has a Newtonian behaviour and the dynamic viscosity is constant; (3) the flow exists at steady state, where the velocity of the fluid does not vary over time; and (4) the flow is laminar, i.e. Re<<1 (Reynolds, 1883). The resulting Stokes equations are solved in their volume averaged form and periodic boundary conditions are imposed. The resulting velocity vector is average in all three directions, and Darcy's law is applied to obtain a directional value for permeability.

In contrast, the LBFlow package relies on the Lattice-Boltzmann equation to model the flow of a fluid (Llewellin 2010a, b). The permeability simulation has been validated or applied using sphere packs in cubic lattice arrangements (Llewellin 2010b; Wadsworth et al. 2017), random overlapping sphere packs (Vasseur & Wadsworth 2017; Vasseur et al. 2020), hard sphere packs (Vasseur et al. 2021; 2022), hexagonal arrays (Vasseur & Wadsworth, 2019), fibrous porous media (Nabovati et al., 2009), sintering systems (Wadsworth et al. 2017; 2021), and basalt pore spaces (Macente et al. 2022). The input data needs to be binary and the phase of interest (the porosity, or here the melt fraction) is discretized into a cubic lattice of fluid nodes in both time space, with a resolution of Δt and Δx respectively. We impose a uniform pressure gradient on the fluid entering to the numerical domain, consequently mobilising the fluid particles. They are propagated along the lattice (according to the selected degrees of freedom) and also undergo collisions, thereby increasing the complexity of the flow. The simulation is run until the flow reaches steady state (i.e. the fluid velocity is constant over time). The fluid velocity u is then averaged for the volume, such that $\langle u \rangle = \phi_m u$, where ϕ_m is space where the fluid can flow (here the melt fraction).

The initial conditions of the simulation are all chosen to ensure that the model remains in the creeping domain, characterised by a low Reynolds number ($10^{-12} \leq \mathrm{Re} \leq 10^{-5}$) as well as adapted fluid velocity (i.e. a low Mach number, $10^{-16} \leq \mathrm{Ma} \leq 10^{-9}$). It is important to keep the simulation conditions in the creeping regime, so that the inertial effects can be neglected. As with Avizo©, the resulting averaged velocity is then input into Darcy's law to obtain the permeability in x, y and z.

The choice of using either method was motivated by a combination of factors, principally time and computing power availability. The permeability simulations in Avizo© require a large processing power and only one simulation can be run simultaneously. The processing power was not available in Durham (mainly due to covid) and the license is shared with other users and departments, such that running lengthy simulations back-to-back was not a sustainable option. Our partners at LMU were able to run the simulations using LBFlow and these were run on the LRZ (Leibniz Supercomputing Centre) Compute Cloud of the Bavarian Academy of Sciences and Humanities (Garching bei München, Germany). There is no scientific reason to choose LBFlow over Avizo©, as shown by the comparison we carried out using a simple geometry of a sphere in a box (Fig. 2.2). It is also worth noting that both methods assume the same simplifications regarding fluid compressibility, Newtonian behaviour and that the flow regime is laminar. These are necessary to compute the permeability and we cannot account for uncertainties created by these assumptions.

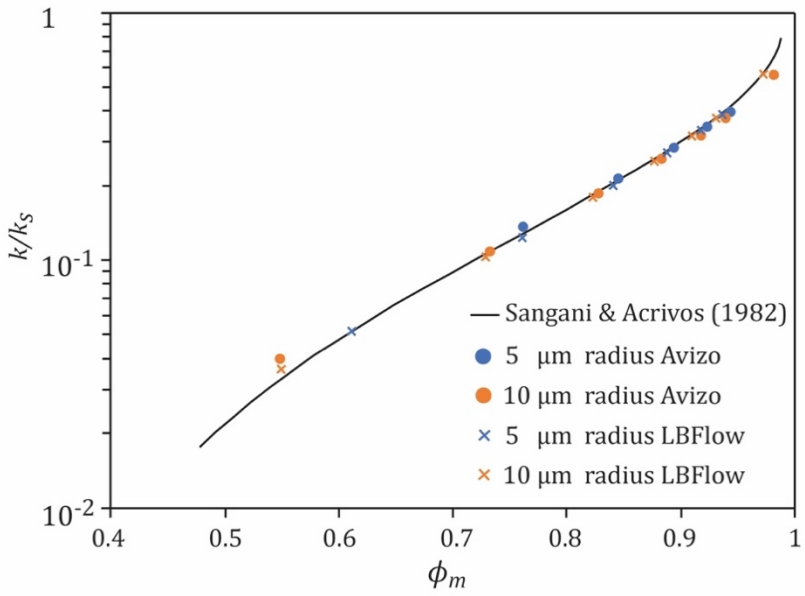

Figure 2.2: The permeability of the simple "sphere in a box" geometry measured with Avizo© and LBFlow. The data is represented here for a sphere of 5 and 10 microns and plotted as the normalised permeability against

the porosity (or melt fraction). The trendline corresponds to the permeability prediction in dilute conditions (i.e. low porosity) from Sangani &Acrivos (1982).

2.3 Specific methodologies deployed in this thesis

The permeability was measured on 3D numerical data produced in two ways: numerically generated packs of cuboids (courtesy of Liu et al., 2017) and analogue data obtained by scanning physical particles in a test tube.

In this section, we are going to introduce the data we use and then explore the practical aspects of extraction the scalar and directional quantities discussed above from 3D data sets.

2.3.1. Materials and data

2.3.1.1. Domains of randomly oriented cuboids at maximum packing

The first type of data we use are numerical periodic domains generated by Liu et al. (2017) of packed and randomly arranged solid cuboids. Cuboids are characterised by their axis lengths a, b, and c and aspect ratios $r_1 = a/b$ and $r_2 = b/c$. The cuboids have a square cross-section so that $b = c$ (hence, $r_2 = 1$) and the domains are produced at their random maximum packing, given by volume fraction ϕ. Here, for completeness, we detail the methods by which these domains were created.

In the 2017 paper, Lui et al. devise a novel inverse packing approach to generate dense, non-overlapping particle packings with a known degree of randomness. The new method is applied to generate a series of maximally dense random packings of hard (i.e. non-overlapping) square-edged cuboids with a range of aspect ratios to investigate the effect of shape on the degree of order/disorder.

The cuboid packs are generated step by step, where the initial cuboid is placed at the centre of the domain and its three principal orthogonal axes are set to coincide with the orientation of the domain. Next, cuboids with random orientation and fixed centre coordinates are added incrementally to surround the central initial cuboid. At each step, each placement of a neighbouring cuboid, the degree randomness is maximised to create a maximally dense random packing. The maximisation is performed using Lui et al. (2017) novel inverse packing method, which dictates the orientation and the centre coordinates of each new cuboid. New cuboids are added N times, i.e. the domains are composed of N cuboids. Lui et al. (2017) produced a series

of dense packings that span aspect ratios $r_1 = 0.2\ to\ r_1 = 6$, where the small aspect ratios ($r_1 < 1$) correspond to prolate shape and larger aspect ratios ($r_1 > 1$) to oblate particles (Fig. 2.3).

The authors have generously shared the numerical domains with us, enabling us to use them to verify our proposed permeability model. In this work, we use the cuboid packs as crystal mush analogues, where the cuboids represent the ridged framework of cumulate crystals and the inter-cuboid space is seen as the melt fraction, the space where the melt can flow around the crystals. This is a very simplified system, which is ideal for an initial observation of the effect of shape and size of the crystals on the permeability and melt flow.

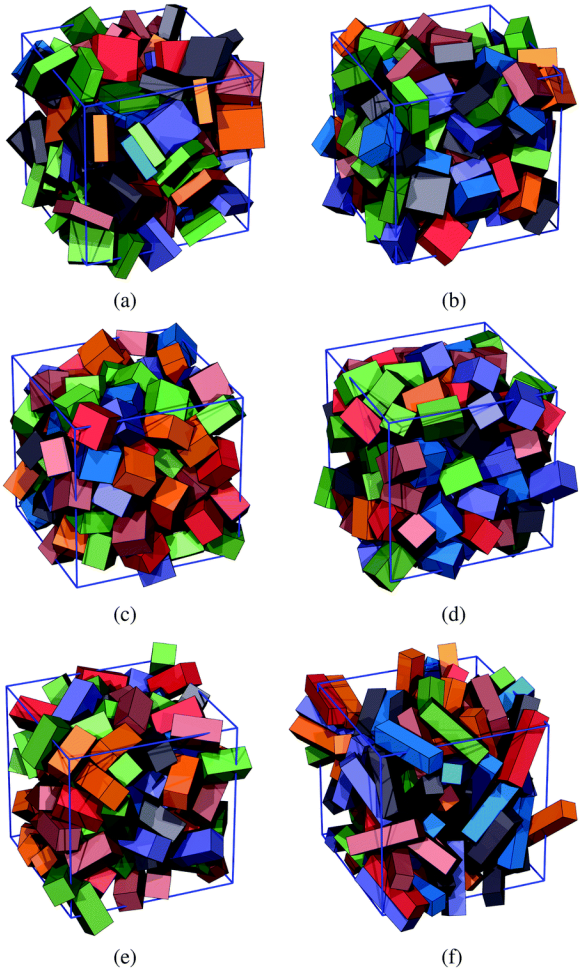

Figure 2.3 : Figure courtesy of Lui et al. (2017) showing 3D renders of the maximally dense random packings at different aspect ratios. a) $r_1 = 0.3$; *b*) $r_1 = 0.5$; c) $r_1 = 0.7$; d) $r_1 = 1.5$; e) $r_1 = 2$; f) $r_1 = 4$

2.3.1.2. Analogues for magma mush using confectionary

The second type of data are tomography scans of analogue mushes, randomly oriented and loosely packed confectionary: fudge chunks and sugar crystals. The output is a 3D grid of voxels, where each voxel is assigned a grayscale value that reflects the density of the materials

scanned. However, since samples are confectionary chunks in a gas phase (laboratory air), the density contrast is high and does not affect the quality of the data at the resolution we are working at (c.f. chapter 4).

For the scan, the particles are loaded randomly into a cylindrical sample volume for which we ensure at least 10 of the particles can fit across the cylinder diameter. The cylinders are shaken slightly to settle the particles into what we presume is relatively close to a random close pack, and then loaded into a Nikon XTH LC 225kV 225W Ultrafocus laboratory X-ray tomography scanner at the University of Strathclyde. Scans were performed at 90 kV (either 91 μA and 2s exposure, or 209 μA and 1 second exposure depending on scan) and were reconstructed using the built-in algorithms to give a 2000 voxel image with 16 μm voxel resolution. Subsequent visualisation and quantification of the ct scans are performed using Avizo©, the details of which are covered in the following section.

Each type of cake topping type is composed of similar shapes, nevertheless, the particles are subject to natural asperities and irregularities. This provides us with an opportunity to verify our proposed percolation model on data that is more imperfect than the cuboid packs, closer to natural crystals.

2.3.2. Extracting quantities from 3D data in practice

In this section, we detail the practical extraction of scalar and directional quantities necessary to model fluid flow and construct a permeability model. We built from the theory explained above and provide specific simulation/analytical conditions for anyone who would want to reproduce the data acquisition.

The first step that is applicable to all data sets is the binarization of the numerical domains, assigning voxels to the solid (crystal) phase and to the melt phase. This step is performed in Avizo© with the *auto-threshold* module, an integrated function that assigns the voxels to phases based on an automatic greyscale threshold determination. This step results in a segmented image where the two phases are selectable and separable. From here on, when referring to the raw data, we are referring to the binary data.

2.3.2.1. Extracting scalar quantities

2.3.2.1.1. Volume fraction of phases

The solid volume fraction ϕ and the melt fraction ϕ_m of the cuboid packs are already provided by Lui et al. (2017). Nevertheless, this data as well as the volume fractions of the analogue mush ct scans are computed with Python's scikit-image toolbox where the sum of voxels that make up each phase (crystal or melt) are compared.

2.3.2.1.2. Surface area of phases

To compute the specific surface area of the crystal phase, we use a marching cubes algorithm (Lorensen & Cline, 1987) from Python's scikit-image toolbox following the efficient algorithm implementation proposed by Lewiner et al. (2003). The algorithm is applied to the segmented crystal-melt binary data. This method determines the surface area of the crystal phase, and then, the specific surface area s is obtained by dividing the result by the total volume of the numerical domain.

2.3.2.1.3. Size of crystals

For the cuboid pack, is not necessary to extract the crystal axes lengths as we already have the two aspect ratios and one side length a. From there, we can calculate the axes lengths b and c.

For the cake topping data, we do not have the aspect ratios nor the size of the crystals. Hence, these need to be extracted from the 3D (as well as from the 2D data) and we perform this analysis in Avizo©. The following steps are consecutive, such that the result from the first step is used directly as the input for step 2, and so on for the following steps. The methodology to extract the crystal axes is organised in three broad steps: (1) the separation of the segmented crystal phase into individual crystals, (2) removing the particles truncated by the boundaries of the sample, (3) analyse the geometry of the remaining crystals. A visual overview of the results of the main steps is shown in Fig. 2.4.

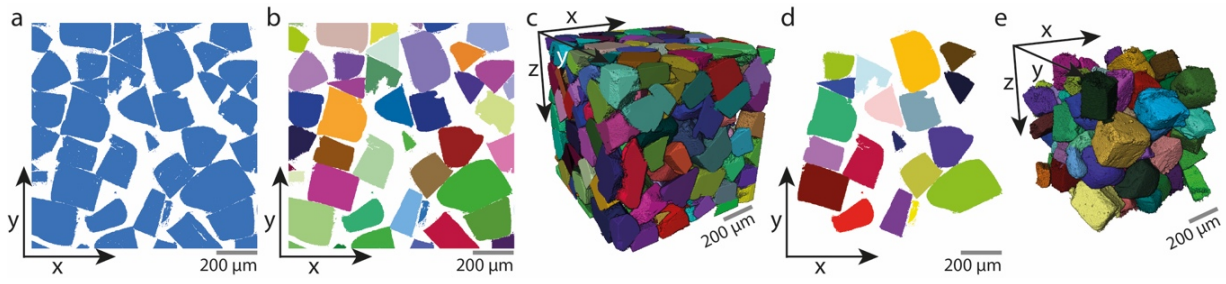

Figure 2.4: Rendering the outputs of five of the analysis steps used here, all illustrated using the fudge chunks. (a) The result of applying an *automatic threshold*, which allows binarization and segmentation of the volume into the two phases: crystals (blue) and melt fraction (white). (b-c) The result of the *fills holes* and conservative *separation* algorithms shown in (b) 2D and (c) 3D. These separated crystals are then labelled (and here coloured) individually

as discrete phases that can be measured independently. (d-e) The result of the *border kil*l algorithm shown in (d) 2D and (e) 3D, which removes the outermost objects.

For step (1), we start off by using the *fill holes* module to fill in any existing pore spaces internal to the particles (scanning artifacts); and then apply a conservative *separation algorithm* to separate the individual crystals and assign a label to each (Fig. 2.4b and 2.4c). For step (2), we use the *border kill* module to remove crystals that intersect the domain boundary (Fig. 2.4d and 4e). This step involves manual checking of each individual object in the volume in order to carefully determine that all objects have been separated effectively. The manual checking process helps us confirm that objects that share flat edge contacts are rare. For step (3), we use the *label analysis* module, which outputs chosen measurements of the separated crystals. In this case, we choose to obtain three orthogonal characteristic axes that represent the volume for each crystal, a, b, and c. This last step can either be performed in 3D, or in 2D, where each slice in a given direction (here z) is analysed individually.

2.3.2.2 Extracting directional quantities

2.3.2.2.1. Connectivity of the pore network

The connectivity of the cuboid domains is assessed using a labelling algorithm, applied to the data in Python. The data is input in the form of the binary file, where the melt fraction is segmented from the crystal phase. Due to the size of the numerical domains, the algorithm is run on smaller sub-volumes, which is moved across the entire domain to make sure that all the domain is assessed and that the results are representative.

2.3.2.2.2. Permeability

For the permeability measurements, we use LBFlow for both the cuboid and the cake topping data. The input files for LBFlow are the segmented files from Avizo©, where the crystals and the melt fraction exist as two different phases. The numerical procedure allows the user to define a driving pressure gradient ∇p, a fluid viscosity μ, and a fluid density ρ. We use $\nabla p = 0.01$ Pa. m^{-1}, and fluid properties of $\mu = 1.8205$ Pa. s and $\rho = 1.2047$ kg. m^{-3} corresponding to the National Institute of Standards and Technology (NIST) values for air at Normal Temperature and Pressure (NTP) conditions (20 °C and 1 atm respectively), and therefore similar to an air permeability test in the laboratory. The simulation converges when the average fluid speed does not change by more than 10^{-5} over 50 time-steps twice consecutively. We

then compute the filtration velocity, which can then be input to Darcy's law to get a permeability value.

We simulate the permeable flow in each of the principal directions of our domains to ensure isotropy and average the result. While we produce and analyse large domains of up to 10^9 voxels, for the permeability simulations we require a smaller domain. Therefore, we use $L = 250$ pixels as a maximum size sub-volume inside the larger ($L = 1000$ pixels) domain. We move the spatial position of this sub-volume around inside the larger volume to ensure that each fluid flow simulation on each sub-volume is representative of the larger system.

2.3.2.3. Additional processing steps

Additionally, we simulate crystal growth in the cuboid packs to verify the percolation law proposed in this work. To achieve this, we use the cuboid packs as the initial starting point for crystal "growth" and the crystal phase is incrementally grown over 20 steps. Each growth step is then run through LBFlow to obtain the permeability and is analysed for the specific surface area s, the melt fraction ϕ_m and the connectivity C in Python.

The "growth" process is performed in Avizo© on the segmented cuboid packs. The melt phase is incrementally eroded (using the *erosion* module) by 1 voxel at each step, effectively dilating the crystal phase and simulating crystal "growth". Note here that the crystals are not grown individually (i.e. we do not apply the method to the separated crystals), but on the segmented crystal phase as one. Furthermore, the erosion step is calibrated to erode 1 voxel with a neighbourhood of 26, meaning that any voxel touching either a face (6), an edge (12) or a corner of the initial voxel is eroded (8). Consequently, the result is termed overgrown crystals as opposed to intergrown (also called overlapping crystals).

Considering the number of iterations of the growth step, the method is batch processed. We install the *batch processing* plug-in module in Avizo©, save the workflow as a recipe and apply this to the initial cuboid packs. Each time step is saved out in Avizo© and then converted into a file format for LBFlow, now ready for the permeability simulation. The format change is performed in the Python console in Avizo©, for which Dr. L. Courtois (3Dmagnination) kindly provided us with a short script that transforms the Avizo© files into tiff stacks.

2.3.2.4. Summary of workflow in Avizo© for future users

Table 2.1 shows details of the modules used in the 3D data analysis in Avizo© and their applicability to numerically generated binary media and ct scans of natural rock samples. Also included are the estimated time for each step and whether there is a possibility of automation or if manual input and checking of the result are necessary. The input for this method requires a 3D raster of voxel informed for the greyscale value, typically the result of either multi-phase numerically generated media or an x-ray scan of natural media.

In the context of permeability predictions, the target is the acquisition of the specific surface area, which can be obtained from the segmented result using a label analysis module (see break Table 2.1). If users want to obtain crystal shape, the separation step is then performed on the segmented phase. Simple enough for numerically generated media, this step can become very complex for natural media as soon as the crystals are substantially inter or overgrown, or even exhibit a preferential orientation. The separation algorithm module in Avizo© is not designed for this type of media and will likely break up the crystals in unnatural ways. We would recommend either applying this to low crystallinity data or samples where there is minimal contact between the crystals. It is important to note that the separation step is not strictly necessary for permeability predictions but could be used to benchmark permeability results obtained with the specific surface area measurement.

Table 2.1: Details of modules used in the Avizo© workflow, the applicability to numerically generated media and ct scans of natural rock samples. Also included is the possibility of automating each step and a time estimate for each processing step.

Analysis step	Avizo© module	Numerical data			Natural rock data		
		applicability	Auto/ manual check	Time est.	applicability	Auto/ manual check	Time est.
Sharpening grain boundaries, smoothing grainy textures	Filtering	N/A	N/A	N/A	Often necessary step to smooth out eventual noisy ct signal	Manual check of result needed	Min. to hours (depending on size of data)
Segmenting a mineral phase/porosity based on greyscale	Threshold/ segmentation workroom	Use automatic thresholding, select black or white (ones and zeros) phase in settings	auto	2 mins.	Use segmentation workroom to manually select target phase and continually check 2D and 3D results	manual	Mins to hours
Breaking up segmented phase into	separation	Automatic process, select	Manual input for size	2-10 mins	Can be very tricky step for natural media if	Manual input for size	Mins. To hours

individual objects		appropriate crystal size	+ manual check of result		grains are inter/overgrown or follow preferential orientation	+ manual check of result	
Removing objects truncated by the sample boundary	Borderkill	Automatic module	auto	1 min	Automatic module	auto	1 min
Shape analysis	Label analysis	Select properties to analyse	auto	2 mins	Select properties to analyse	auto	2 mins
3D rendering of results	Volume rendering	Automatic module	auto	30 secs.	Automatic module	auto	30 secs.

References

Arzilli, F., La Spina, G., Burton, M.R., Polacci, M., Le Gall, N., Hartley, M.E., Di Genova, D., Cai, B., Vo, N.T., Bamber, E.C. and Nonni, S., 2019. Magma fragmentation in highly explosive basaltic eruptions induced by rapid crystallization. *Nature Geoscience*, *12*(12), pp.1023-1028.

Bachmann, O. and Bergantz, G.W., 2004. On the origin of crystal-poor rhyolites: extracted from batholithic crystal mushes. *Journal of Petrology*, *45*(8), pp.1565-1582.

Baker, D.R., Brun, F., O'shaughnessy, C., Mancini, L., Fife, J.L. and Rivers, M., 2012. A four-dimensional X-ray tomographic microscopy study of bubble growth in basaltic foam. *Nature Communications*, *3*(1), pp.1-8.

Bernard, M.L., Zamora, M., Géraud, Y. and Boudon, G., 2007. Transport properties of pyroclastic rocks from Montagne Pelée volcano (Martinique, Lesser Antilles). *Journal of Geophysical Research: Solid Earth*, *112*(B5).

Blower, J., 2001. Factors controlling permeability–porosity relationships in magma. *Bulletin of Volcanology*, *63*(7), pp.497-504.

Bouvet de Maisonneuve, C., Bachmann, O. and Burgisser, A., 2009. Characterization of juvenile pyroclasts from the Kos Plateau Tuff (Aegean Arc): insights into the eruptive dynamics of a large rhyolitic eruption. *Bulletin of volcanology*, *71*(6), pp.643-658.

Carlson, W.D. and Denison, C., 1992. Mechanisms of porphyroblast crystallization: results from high-resolution computed X-ray tomography. *Science*, *257*(5074), pp.1236-1239.

Chen, S. and Doolen, G.D., 1998. Lattice Boltzmann method for fluid flows. *Annual review of fluid mechanics*, *30*(1), pp.329-364.

Cnudde, V. and Boone, M.N., 2013. High-resolution X-ray computed tomography in geosciences: A review of the current technology and applications. *Earth-Science Reviews*, *123*, pp.1-17.

Colombier, M., Wadsworth, F.B., Gurioli, L., Scheu, B., Kueppers, U., Di Muro, A. and Dingwell, D.B., 2017. The evolution of pore connectivity in volcanic rocks. *Earth and planetary science letters*, *462*, pp.99-109.

Colombier, M., Wadsworth, F.B., Scheu, B., Vasseur, J., Dobson, K.J., Cáceres, F., Allabar, A., Marone, F., Schlepütz, C.M. and Dingwell, D.B., 2020. In situ observation of the percolation threshold in multiphase magma analogues. *Bulletin of volcanology*, *82*(4), pp.1-15.

Darcy, H., 1856. The public fountains of the city of Dijon. *Victor Dalmont, Paris, France*.

Degruyter, W., Bachmann, O. and Burgisser, A., 2010. Controls on magma permeability in the volcanic conduit during the climactic phase of the Kos Plateau Tuff eruption (Aegean Arc). *Bulletin of Volcanology*, *72*(1), pp.63-74.

Dobson, K.J., Allabar, A., Bretagne, E., Coumans, J., Cassidy, M., Cimarelli, C., Coats, R., Connolley, T., Courtois, L., Dingwell, D.B. and Di Genova, D., 2020. Quantifying microstructural evolution in moving magma. *Frontiers in Earth Science*, *8*, p.287.

Duchêne, S., Pupier, E., De Veslud, C.L.C. and Toplis, M.J., 2008. A 3D reconstruction of plagioclase crystals in a synthetic basalt. *American Mineralogist*, *93*(5-6), pp.893-901.

Farquharson, J., Heap, M.J., Varley, N.R., Baud, P. and Reuschlé, T., 2015. Permeability and porosity relationships of edifice-forming andesites: a combined field and laboratory study. *Journal of Volcanology and Geothermal Research*, *297*, pp.52-68.

Fiorio, C. and Gustedt, J., 1996. Two linear time union-find strategies for image processing. *Theoretical Computer Science*, *154*(2), pp.165-181.

Formenti, Y. and Druitt, T.H., 2003. Vesicle connectivity in pyroclasts and implications for the fluidisation of fountain-collapse pyroclastic flows, Montserrat (West Indies). *Earth and Planetary Science Letters*, *214*(3-4), pp.561-574.

Friis, E.M., Grimm, G.W., Miguel Mendes, M. and Pedersen, K.R., 2015. Canrightiopsis, a new Early Cretaceous fossil with Clavatipollenites-type pollen bridge the gap between extinct Canrightia and extant Chloranthaceae. *Grana*, *54*(3), pp.184-212.

He, X. and Luo, L.S., 1997. Lattice Boltzmann model for the incompressible Navier–Stokes equation. *Journal of statistical Physics*, *88*(3), pp.927-944.

Higgins, M.D., 2000. Measurement of crystal size distributions. *American Mineralogist*, *85*(9), pp.1105-1116.

Holness, M.B., 1997. Surface chemical controls on pore-fluid connectivity in texturally equilibrated materials. *Fluid flow and transport in rocks*, pp.149-169.

Jackson, M.D., Blundy, J. and Sparks, R.S.J., 2018. Chemical differentiation, cold storage and remobilization of magma in the Earth's crust. *Nature*, *564*(7736), pp.405-409.

Katyo, Y., 1987. Woody pumice generated with submarine eruption. *Chishitsugaku Zasshi*, *93*(1), pp.11-20.

Keller, L.M., Holzer, L., Wepf, R., Gasser, P., Münch, B. and Marschall, P., 2011. On the application of focused ion beam nanotomography in characterizing the 3D pore space geometry of Opalinus clay. *Physics and Chemistry of the Earth, Parts A/B/C*, *36*(17-18), pp.1539-1544.

Klug, C., Cashman, K.V. and Bacon, C., 2002. Structure and physical characteristics of pumice from the climactic eruption of Mount Mazama (Crater Lake), Oregon. *Bulletin of Volcanology*, *64*(7), pp.486-501.

Le Gall, N., Arzilli, F., La Spina, G., Polacci, M., Cai, B., Hartley, M.E., Vo, N.T., Atwood, R.C., Di Genova, D., Nonni, S. and Llewellin, E.W., 2021. In situ quantification of crystallisation kinetics of plagioclase and clinopyroxene in basaltic magma: Implications for lava flow. *Earth and Planetary Science Letters*, *568*, p.117016.

Le Pennec, J.L., Hermitte, D., Dana, I., Pezard, P., Coulon, C., Cochemé, J.J., Mulyadi, E., Ollagnier, F. and Revest, C., 2001. Electrical conductivity and pore-space topology of Merapi Lavas: Implications for the degassing of porphyritic andesite magmas. *Geophysical research letters*, *28*(22), pp.4283-4286.

Lewiner, T., Lopes, H., Vieira, A.W. and Tavares, G., 2003. Efficient implementation of marching cubes' cases with topological guarantees. *Journal of graphics tools*, *8*(2), pp.1-15.

Lindgren, J., Sjövall, P., Thiel, V., Zheng, W., Ito, S., Wakamatsu, K., Hauff, R., Kear, B.P., Engdahl, A., Alwmark, C. and Eriksson, M.E., 2018. Soft-tissue evidence for homeothermy and crypsis in a Jurassic ichthyosaur. *Nature*, *564*(7736), pp.359-365.

Liu, T., Lin, B. and Yang, W., 2017. Impact of matrix–fracture interactions on coal permeability: model development and analysis. *Fuel*, *207*, pp.522-532.

Llewellin, E.W., 2010. LBflow: An extensible lattice Boltzmann framework for the simulation of geophysical flows. Part I: theory and implementation. *Computers & Geosciences*, *36*(2), pp.115-122.

Llewellin, E.W., 2010. LBflow: An extensible lattice Boltzmann framework for the simulation of geophysical flows. Part II: usage and validation. *Computers & geosciences*, *36*(2), pp.123-132.

Lorensen, W.E. and Cline, H.E., 1987. Marching cubes: A high resolution 3D surface construction algorithm. *ACM siggraph computer graphics*, *21*(4), pp.163-169.

Macente, A., Dobson, K.J., MacDonald, J., Wadsworth, F.B. and Vasseur, J., 2022. The Evolution of Paleo-Porosity in Basalts: Reversing Pore-Filling Mechanisms Using X-Ray Computed Tomography. *Transport in Porous Media*, pp.1-21.

Mangler, M.F., Humphreys, M.C., Wadsworth, F.B., Iveson, A.A. and Higgins, M.D., 2022. Variation of plagioclase shape with size in intermediate magmas: a window into incipient plagioclase crystallisation. *Contributions to Mineralogy and Petrology*, *177*(6), p.64.

Martys, N.S., Torquato, S. and Bentz, D.P., 1994. Universal scaling of fluid permeability for sphere packings. *Physical Review E*, *50*(1), p.403.

Munawar, M.J., Lin, C., Cnudde, V., Bultreys, T., Dong, C., Zhang, X., De Boever, W., Zahid, M.A. and Wu, Y., 2018. Petrographic characterization to build an accurate rock model using micro-CT: Case study on low-permeable to tight turbidite sandstone from Eocene Shahejie Formation. *Micron*, *109*, pp.22-33.

Nabovati, A., Llewellin, E.W. and Sousa, A.C., 2009. A general model for the permeability of fibrous porous media based on fluid flow simulations using the lattice Boltzmann method. *Composites Part A: Applied Science and Manufacturing*, *40*(6-7), pp.860-869.

Nakamura, M., Otaki, K. and Takeuchi, S., 2008. Permeability and pore-connectivity variation of pumices from a single pyroclastic flow eruption: Implications for partial fragmentation. *Journal of Volcanology and Geothermal Research*, *176*(2), pp.302-314.

Nakamura, M., Otaki, K. and Takeuchi, S., 2008. Permeability and pore-connectivity variation of pumices from a single pyroclastic flow eruption: Implications for partial fragmentation. *Journal of Volcanology and Geothermal Research*, *176*(2), pp.302-314.

Newman, M.E. and Ziff, R.M., 2001. Fast Monte Carlo algorithm for site or bond percolation. *Physical Review E*, *64*(1), p.016706.

Okumura, S., Nakamura, M., Tsuchiyama, A., Nakano, T. and Uesugi, K., 2008. Evolution of bubble microstructure in sheared rhyolite: Formation of a channel-like bubble network. *Journal of Geophysical Research: Solid Earth*, *113*(B7).

Okumura, S., Nakamura, M., Uesugi, K., Nakano, T. and Fujioka, T., 2013. Coupled effect of magma degassing and rheology on silicic volcanism. *Earth and Planetary Science Letters*, *362*, pp.163-170.

Pistone, M., Arzilli, F., Dobson, K.J., Cordonnier, B., Reusser, E., Ulmer, P., Marone, F., Whittington, A.G., Mancini, L., Fife, J.L. and Blundy, J.D., 2015. Gas-driven filter pressing in magmas: Insights into in-situ melt segregation from crystal mushes. *Geology*, *43*(8), pp.699-702.

Polacci, M., Arzilli, F., La Spina, G., Le Gall, N., Cai, B., Hartley, M.E., Di Genova, D., Vo, N.T., Nonni, S., Atwood, R.C. and Llewellin, E.W., 2018. Crystallisation in basaltic magmas revealed via in situ 4D synchrotron X-ray microtomography. *Scientific reports*, *8*(1), pp.1-13.

Reynolds, O., 1883. An experimental investigation of the circumstances which determine whether the motion of water shall be direct or sinuous, and of the law of resistance in parallel channels. *Proceedings of the royal society of London*, *35*(224-226), pp.84-99.

Rust, A.C. and Cashman, K.V., 2011. Permeability controls on expansion and size distributions of pyroclasts. *Journal of Geophysical Research: Solid Earth*, *116*(B11).

S Succi, R Benzi, 1991. Simulation Of Nonlinear Systems In Physics, *World Scientific*

Shea, T., Gurioli, L. and Houghton, B.F., 2012. Transitions between fall phases and pyroclastic density currents during the AD 79 eruption at Vesuvius: building a transient conduit model from the textural and volatile record. *Bulletin of volcanology*, *74*(10), pp.2363-2381.

Shimano, T. and Nakada, S., 2006. Vesiculation path of ascending magma in the 1983 and the 2000 eruptions of Miyakejima volcano, Japan. *Bulletin of volcanology*, *68*(6), pp.549-566.

Song, S.R., Jones, K.W., Lindquist, B.W., Dowd, B.A. and Sahagian, D.L., 2001. Synchrotron X-ray computed microtomography: studies on vesiculated basaltic rocks. *Bulletin of Volcanology*, *63*(4), pp.252-263.

Tripoli, B., Manga, M., Mayeux, J. and Barnard, H., 2019. The effects of deformation on the early crystallization kinetics of basaltic magmas. *Frontiers in Earth Science*, *7*, p.250.

Vasseur & Wadsworth, 2017

Vasseur, J. and Wadsworth, F.B., 2019. The permeability of columnar jointed lava. *Journal of Geophysical Research: Solid Earth*, *124*(11), pp.11305-11315.

Vasseur, J., Wadsworth, F.B., Bretagne, E. and Dingwell, D.B., 2022. Universal scaling for the permeability of random packs of overlapping and nonoverlapping particles. *Physical Review E*, *105*(4), p.L043301.

Vasseur, J., Wadsworth, F.B., Coumans, J.P. and Dingwell, D.B., 2021. Permeability of packs of polydisperse hard spheres. *Physical Review E*, *103*(6), p.062613.

Voeten, D.F., Cubo, J., De Margerie, E., Röper, M., Beyrand, V., Bureš, S., Tafforeau, P. and Sanchez, S., 2018. Wing bone geometry reveals active flight in Archaeopteryx. *Nature communications*, *9*(1), pp.1-9.

Wadsworth, F.B., Vasseur, J., Llewellin, E.W. and Dingwell, D.B., 2017. Sintering of polydisperse viscous droplets. *Physical Review E*, *95*(3), p.033114.

Wadsworth, F.B., Vasseur, J., Scheu, B., Kendrick, J.E., Lavallée, Y. and Dingwell, D.B., 2016. Universal scaling of fluid permeability during volcanic welding and sediment diagenesis. *Geology*, *44*(3), pp.219-222.

Wadsworth, F.B., Witcher, T., Vasseur, J., Dingwell, D.B. and Scheu, B., 2017. When does magma break?. In *Volcanic unrest* (pp. 171-184). Springer, Cham.

Wright, H.M. and Cashman, K.V., 2014. Compaction and gas loss in welded pyroclastic deposits as revealed by porosity, permeability, and electrical conductivity measurements of the Shevlin Park Tuff. *Bulletin*, *126*(1-2), pp.234-247.

Wright, H.M., Cashman, K.V., Gottesfeld, E.H. and Roberts, J.J., 2009. Pore structure of volcanic clasts: measurements of permeability and electrical conductivity. *Earth and Planetary Science Letters*, *280*(1-4), pp.93-104.

Wu, B.F. and Wang, K.C., 2005. Robust endpoint detection algorithm based on the adaptive band-partitioning spectral entropy in adverse environments. *IEEE Transactions on Speech and Audio Processing*, *13*(5), pp.762-775.

Yokoyama, T. and Takeuchi, S., 2009. Porosimetry of vesicular volcanic products by a water-expulsion method and the relationship of pore characteristics to permeability. *Journal of Geophysical Research: Solid Earth*, *114*(B2).

Chapter 3 : The permeability of loose magma mush

Chapter preamble

This chapter is under consideration for publication in *Geology* with the following citation:
Bretagne, E., Wadsworth, F.B., Vasseur, J., Humphreys, M.C.S, Dingwell, D.B., Dobson, K.J, Mangler, M, Rooyakkers, S.M, The permeability of loose magma mush, *In review.*

The author contribution by the PhD candidate amounts to 60% of the content, and the manuscript draft presented here was authored solely by the PhD candidate.

Models for the evolution of magma mush zones are of fundamental importance for understanding magma storage, differentiation in the crust, and melt extraction processes that prime eruptions. These models are underpinned by calculations of the permeability of the evolving crystal frameworks in the mush, which controls the rate of melt movement relative to crystals. Existing approaches for estimating the crystal framework permeability do not account for crystal shape. Here, we represent magma mush crystal frameworks as packs of hard cuboids with a range of aspect ratios, all at their maximum random packing. We use numerical fluid flow simulation tools to determine the melt fraction, specific surface area, and permeability of our 3D digital samples. We find that crystal shape exerts a first-order control on both the melt fraction at maximum packing, and on the permeability. We use these new data to generalize a Kozeny-Carman model in order to propose a simple constitutive law for the scaling between permeability and melt fraction that accounts for crystal shape in upscaled mush dynamics simulations. Our results show that magma mush permeability calculated using a model that accounts for crystal shape is significantly different compared with models that make a spherical crystal approximation, with key implications for crustal melt segregation flux and reactive flow.

Keywords: Darcy; volcanic eruption; rhyolite; magma reservoir; silicic magma

3.1 Introduction

Substantial volumes of melt are stored in magma mush regions throughout the crust (Hildreth, 1981; Sparks & Cashman, 2017). Models for the evolution of these magma mush zones are of fundamental importance for magma storage timescales, differentiation in the crust, and melt extraction processes that prime eruptions (Bachmann & Bergantz, 2004; Jackson et al. 2018). The initial assembly of crustal magma bodies requires emplacement of, and percolative reactive flow through, crystal mushes (Jackson et al. 2018). The eruption of crystal-poor magmas requires that melts be separated from these mushes (Bachmann & Bergantz, 2004). While the details of these dynamics, the controlling processes, and the overall rates, are all poorly constrained and widely discussed (Petford 2020; Holness 2018), in most models, it is the permeability of the interlocking crystal framework that is a first-order rate-limiter. Leading quantitative models for melt percolation dynamics on crystal scales use variations on a Kozeny-Carman permeability law for which the crystals are assumed to have a single radius (Petford, 1995; Bachmann & Bergantz, 2004; Jackson et al. 2018). Therefore, these constitutive models for mush permeability cannot account for crystal shape or the difference in percolative hydraulic properties between one mush and another if the phenocrysts are of similar size.

Petrological and geochronological evidence suggests that melt percolation and extraction prior to the eruption of crystal-poor rhyolites occurs in transient and episodic events rather than continuously over the thermal lifespan of the mush (e.g. Allan et al., 2013). In most known cases, the extraction timescales derived from petrological methods are rapid compared with simple gravitational compaction processes, leading to models that involve additional heat by mafic recharge magmas (e.g. Huang et al. 2015), and/or applied directional stresses and strain (Clemens & Petford, 1999; Bachmann & Bergantz 2008; Holness 2018) resulting in anisotropic dilation of the mush (Liu & Lee, 2021). Differentiating between one mechanism and another, or developing predictive frameworks for melt segregation timescales, all depend on rigorous constitutive models for the permeability of real mushes (e.g. Bachmann & Bergantz, 2004), which remains poorly investigated. A key challenge is that the 3D shape of crystals is likely to affect both the melt fraction at maximum crystal packing in the mush and the permeability at that melt fraction, such that models should seek to constrain both effects simultaneously.

3.2 Methods: percolation of melts through magma mush

Melt extraction rates are given by the volumetric melt flux through a mush, Q, which in turn is governed by Darcy's law $\nabla P = -\mu_f Q/(kA)$ where ∇P is the driving melt pressure gradient in the direction of the flux, μ_f is the melt shear viscosity, k is the permeability of the mush, and A is the area normal to the extraction direction. Throughout we make an isotropic assumption, such that mush permeability can be treated as a pseudo-scalar and equal in all directions, in line with previous work (e.g. Bachmann & Bergantz, 2004). Previous models have used simple scaling laws for k that assume all crystals are spherical and can be defined by their radius (e.g. Bachmann & Bergantz, 2004; Huber et al. 2010; Hartung et al. 2019; Floess et al. 2019; Pistone et al. 2020). The most widely used model for k is the Kozeny-Carman equation, where k as a function of the solid volume fraction ϕ, the specific surface area of the network s, and a dimensionless constant C (c.f. Röding et al. 2020; Vasseur et al. 2021)

$$k = \frac{(1-\phi)^3}{Cs^2}. \qquad \text{Eq. 1}$$

Using the specific surface area for volumes packed with monodisperse spheres of radius R gives $s = 3(\phi)/R$, which results in $k = (1-\phi)^3 R^2/[9C(\phi)^2]$ (e.g. Hersum et al., 2015; Lui and Lee, 2021). $C = 5$ has been found to be a typical value for most granular systems (Vasseur et al. 2021; Röding et al. 2020; Torquato, 2013). However, the problem remains that the solid crystals in silicic mushes are often dominated by non-spherical crystals, and indeed may involve highly anisometric crystals such as high aspect ratio plagioclase (see Fig. 3.1A) or amphibole. Here, our central aim is to find a form of Eq. 1 that accounts for 3D crystal shape, and that can be used widely in mush evolution models.

We use numerical periodic domains generated by Liu et al. (2017) of packed and randomly arranged solid cuboids to approximate magma mush, which is a geometry that is closer to natural crystal shapes than spheres (c.f. Fig. 3.1A). Our cuboids have axis lengths a, b, and c and length aspect ratios $r_1 = c/a$ and $r_2 = b/a$. The cuboids have a square cross-section such that $a = b$ (hence, $r_2 = 1$) and the domains are produced at their random maximum packing, given by volume fraction $\phi = \phi'$ (Figure 3.1B). Liu et al. (2017) used order parameters to ensure that the packs are isotropic and disordered (i.e. no fabrics or cuboid preferred arrangements are found). We use a marching cubes algorithm to determine the specific surface area of each cuboid pack (Lorensen & Cline 1987), and we use LBflow – a numerical lattice-Boltzmann fluid flow simulation tool (Llewellin, 2010a, 2010b) – to characterise steady-state

fluid flow through the inter-cuboid space and output the permeability of each cuboid domain (details of the numerical analysis are provided in the Appendix 1).

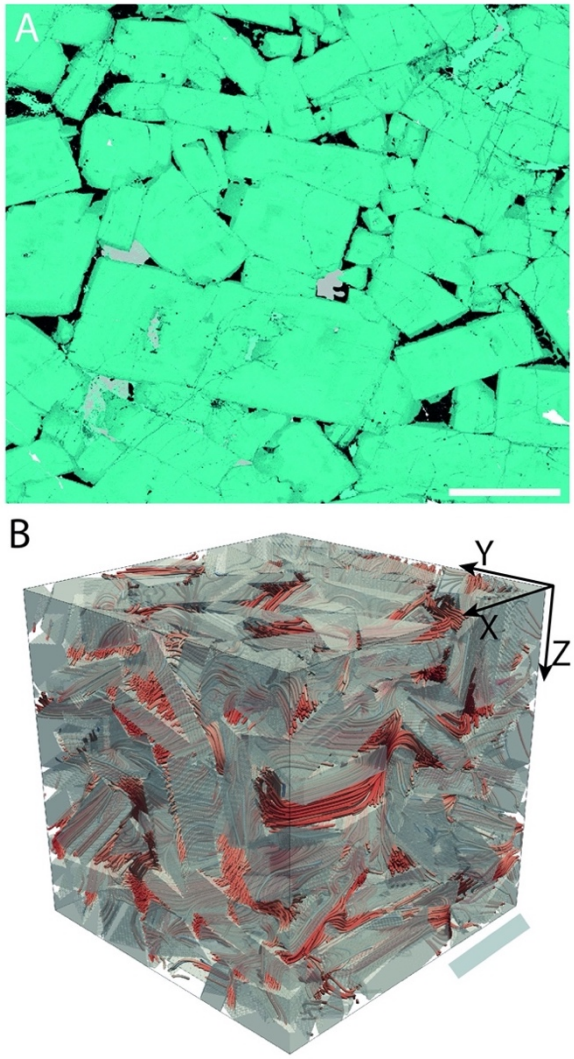

Figure 3.1. Mush textural characteristics compared with our simulated mush. (A) Ca-concentration map from a leucocratic portion of the Layered Series of the Skaergaard intrusion (East Greenland), demonstrating the anisometric and broadly cuboidal nature of plagioclase crystals (in teal) with interstitial quartz (black) and clinopyroxene in grey (reproduced with permission from Holness et al., 2019, scalebar is 1mm). (B) 3D visualization of a numerical cuboid pack ($r_1 = 0.2$) with the flow pattern at steady state represented in the melt phase (scalebar is 100 μm).

3.3 Results and analysis

The results of our permeability determinations show that the permeability is a function of the melt fraction $1 - \phi$ and the specific surface area as predicted by Eq. 1, which is a function of the crystal aspect ratio r_1. All raw results are provided in the Appendix 1. In order to analyse these results in a unified manner across a range of crystal sizes, we introduce the dimensionless

permeability $\bar{k} = k/k_s = ks^2/(2\phi)$, where k_s is a generalized Stokes permeability (Vasseur & Wadsworth, 2017; Vasseur et al. 2020) and the specific surface area is measured directly for our packs. Our data for the normalized permeability $\bar{k}$ collapse to a single trend as a function of melt fraction, regardless of r_1 and crystal size (Fig. 3.2A), indicating that our non-dimensional approach captures these effects. In this normalized space, Eq. 1 becomes universal for any crystal shape and is $\bar{k} = (1-\phi)^3/(2C\phi)$; we find good agreement between the model and the cuboid dataset with the classic $C = 5$ (Torquato, 2013). To calibrate this further, we compare our results with published permeability data for packs of hard spheres normalized in the same way (Fig 3.2A). The excellent agreement we see between the numerical data and the model is used to validate Eq. 2 as a permeability model applicable to any particle/crystal shape as s is known. We note that in the dilute limit as $\phi \to 0$, the sphere data deviate from Eq. 1, which is explored and modeled by Vasseur et al. (2021) using a dilute expansion of k_s (see Appendix 1).

The analysis for $\bar{k}$ relies on our determination of the specific surface area for each sample, which in turn depends on the aspect ratio r_1 and the melt fraction. In order to render this of wide utility in systems for which s is not known *a priori*, we test our model using the theoretical specific surface area of a pack cuboids with interstitial melt fraction (Eq.2; see Appendix 1 for derivation).

$$s = \frac{2\phi}{a}\left(1 + \frac{1}{r_1} + \frac{1}{r_2}\right) \qquad \text{Eq. 2}$$

which reduces to $s = 2\phi(2 + 1/r_1)/a$ when $r_2 = 1$ (square-ended cuboids used here). As with k, we can compare our results for s with the prediction of Eq. 2 across all cuboid packs used here, by making Eq. 2 scale-independent via the normalisation $\bar{s} = sa/\phi$, which reduces Eq. 2 to $\bar{s} = 4 + 2/r_1$.

We find that our data for s, converted to $\bar{s}$, collapse to a single trend, which matches the prediction of this $\bar{s}$ model (Fig. 3.2B). This shows that the normalized specific surface area $\bar{s}$ decreases as the cuboids move from oblate (platy-habit such that $r_1 \ll 1$) to prolate (needle-habit such that $r_1 \gg 1$), meaning that rod-like crystals have a lower specific surface area at their maximum packing. Hence, with reference to Eq. 1, the permeability of maximally packed mush consisting of prolate crystals will be higher than that of a mush made from oblate crystals. The result presented in Fig. 3.2B (i.e. the success of Eq. 2 in describing the specific surface area of the cuboid packs used here) suggests that the incidence of planar cuboid-cuboid contact surfaces is rare, and therefore justifies our use of Eq. 1 and the generalization of permeability

by $k \propto 1/s^2$. We propose that Eq. 2 used with Eq. 1, validated herein, represents a universal model for the permeability of packs of cuboids as a proxy for the permeability of magma mush, and given in expanded dimensional form by

$$k = \frac{(1-\phi)^3 a^2}{4C\phi^2}\left(1+\frac{1}{r_1}+\frac{1}{r_2}\right)^{-2}. \qquad \text{Eq. 3}$$

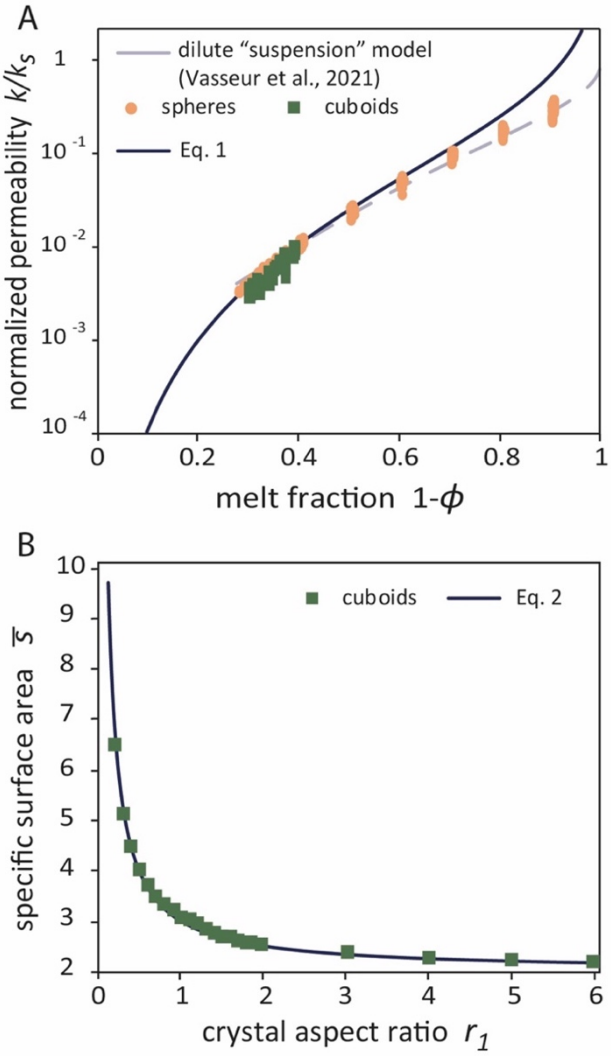

Figure 3.2. The permeability and specific surface area of the cuboid packs analyzed, compared with our proposed theoretical models. (A) the normalised permeability k/k_s as a function of melt volume fraction $1-\phi$. The squares are the results from cuboid packs from Lui et al. (2017); the circles are for hard spheres (Vasseur et al. 2021) for validation and comparison. The solid curve represents our model $\bar{k} = k/k_s = (1-\phi)^3/(2C\phi)$ using $C = 5$. The dashed curve represents a dilute expansion for the 'suspension' regime at high melt fraction (Vasseur et al. 2021) which is shown for completeness, but which is not relevant to melt extraction in mushes. (B) The scaling for s as a function of r_1 for cuboids cast as the normalized $\bar{s}$. Taken together, these results represent a validation of our model.

3.4 Loose mush vs maximally packed mush

Using Eq. 3, we can calculate the permeability of percolating mush using measured or estimated crystal aspect ratios and sizes for a given melt fraction thereby accounting for crystal shape. Crystal shape not only changes the permeability at a given melt fraction, but also strongly affects the maximum packing fraction itself. Mush maximum packing fraction ϕ' is a function of r_1 (Fig. 3.3), and for $r_1 = 1$ (cubes), there is a local minimum in ϕ', and local maxima at $r_1 \approx 0.7$ and $r_1 \approx 1.5$. Our results are consistent with the general form for previous results for loose random packs of non-spherical particles (e.g. Donev et al. 2004; Wouterse et al. 2007; Rudge et al. 2008; Delaney et al. 2010; Meng et al. 2016; Liu et al. 2017). As crystals become highly oblate ($r_1 \ll 0.7$) or highly prolate ($r_1 \gg 1.5$), ϕ' drops, and is symmetric in $\log(r_1)$ around $r_1 = 1$. The function $\phi' = \phi'_0(Ax + 1)\exp(-Bx)$ matches our data, where $\phi'_0 = 0.641$ is the numerically determined value of ϕ' at $r_1 = 1$, $x = |\log_{10}(r_1)|$, and $A = 1.26$ and $B = 1.04$ are best-fit constants.

At high melt fraction, crystals do not interact or communicate force (i.e. a 'suspension'). Conversely, at the random maximum packing of crystals, a mush can support load and transmit force through the crystal framework but cannot densify further by compaction or other processes without deformation or re-organisation of the crystal framework. The transition from 'suspension' to a random maximally packed mush can be termed the 'loose mush' region, and we posit that the percolative extraction of melt begins when crystal fractions increase to a critical value $\phi = \phi_\tau$. We interpret ϕ_τ to be the lowest crystal volume fraction at which crystal-crystal force interactions can occur. Mueller et al., (2010) show that $\phi_\tau \approx 0.8\phi'$ for all r_1. Using this and our model for how the maximum packing varies with crystal shape, we can quantitatively define the 'loose mush' region. Furthermore, using our general model (Eq. 3), we can predict the permeability at ϕ_τ and ϕ' for all r_1. We note here that ϕ_τ is an approximate and indicative value, and that granular dynamics simulations demonstrate that a single melt fraction may be insufficient to demark the boundary between 'suspension' and 'loose mush' regimes (Deng et al. 2021). Regardless, whatever definition of a lower-bound on ϕ one places to demark 'loose mush', our model can predict k for that ϕ.

In Fig. 3.3 we show the results of our model (Eq. 3) in two modes of application. First, we show the general results of our permeability model for any melt fraction and a range of crystal shapes (Fig. 3.3; $a = 1$ mm). Second, we show the results of the model specifically for the upper and lower bounds on the 'loose mush' region, defined as when the crystal volume fraction is between the onset of crystal-crystal interactions, and the random maximum packing

$\phi_\tau < \phi < \phi'$. This second mode of application of Eq. 3 allows us to deconvolve the two principal effects predicted here: (1) the effect of r_1 on ϕ' or ϕ_τ, and (2) the resultant effect of r_1 on the permeability. Fig. 3.3 shows that crystal shape can play a substantial role in controlling the absolute value of the permeability in these 'loose' simulated crystal mushes. A limitation of this model is that anisotropy is not considered, and that in nature, evolution of mush from ϕ_τ to ϕ' may well involve crystal rearrangements and fabric development (see Liu & Lee, 2021).

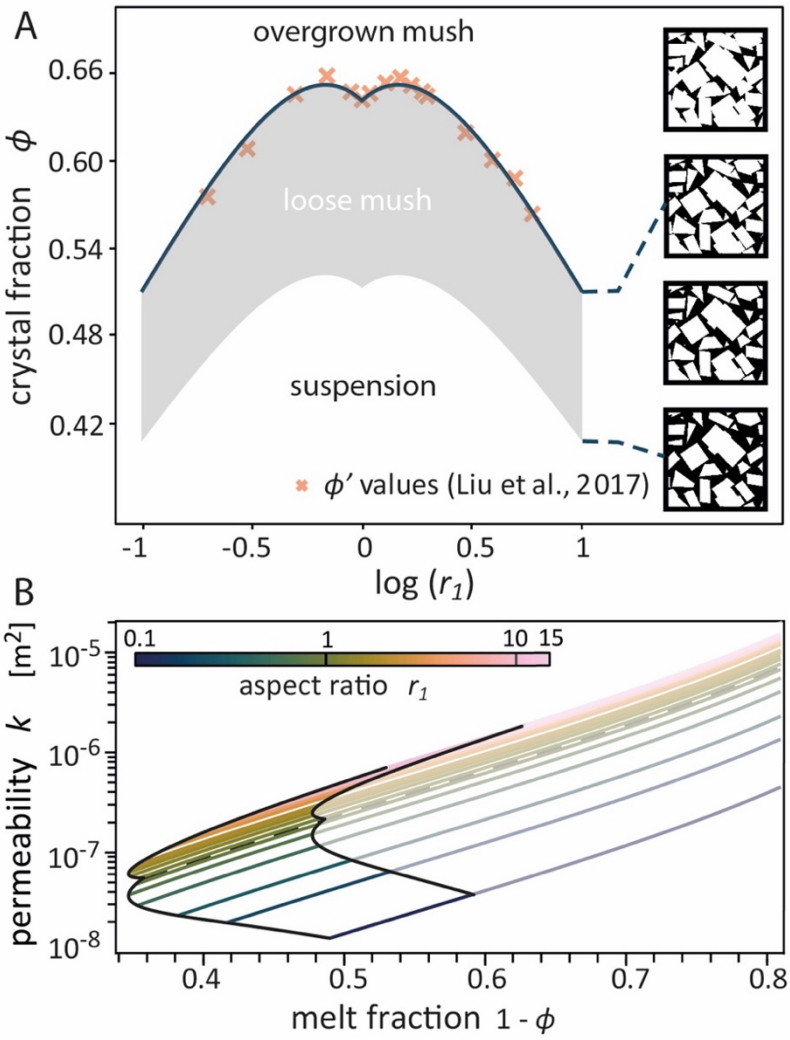

Figure 3.3. The permeability model for cuboid packs plotted for loose mush and for a range of aspect ratios ($0.1 < r_1 < 15$). (A) The maximum packing crystal volume fraction ϕ' as a function of r_1 (data from Liu et al., 2017) compared with our empirical model for ϕ' (see text). The grey shaded area terminates against the upper bound of ϕ' and a lower bound at $\phi_\tau = 0.8\phi'$ (Mueller et al. 2010) and represents the loose mush field. (B) The model (Eq. 3) solved using input crystal square edge length $a = 1$ cm. The black curves represent the solution for each aspect ratio at the specific maximum packing value (see A). The cartoons on panel A are a visual representation of the mush at different crystal fractions, showing the indicative texture of intergrown and loose mush, as well as a suspension at low crystal fraction.

3.5 Implications: rates of percolation through magma mush

In this study, we have used packs of square-ended cuboids, however, via Eq. 3 our model is applicable to crystals of arbitrary 3D shape. In order to apply our model to mush with real crystals, we use published data for plagioclase phenocryst shapes (Duchene et al., 2008), wherein a, b, and c are measured directly ($a{:}b{:}c = 1{:}\,6.5{:}\,9.6$; Duchêne et al. 2008). In all cases, we normalize all measured crystal shapes so that they are relative to a, which we take to be the shortest of the axes. We note that this approach does not alter r_1 and r_2. Then we assign $a = 1$ cm, in order to compute the permeabilities of mushes that comprise those shapes. Using this workflow, we find that for a given melt fraction, the permeabilities of the plagioclase mush fall within an order of magnitude of each other. Importantly, at a melt fraction of 0.5, these datasets occur at predicted permeabilities up to a maximum of 1.5 orders of magnitude greater than the prediction of the Jackson et al. (2018) scaling (Fig. 3.4). Since such models predict the flux of melt to the shallow crust, we posit that our model has implications for overall melt accumulation timescales. Our model (Eq. 3) can be used to predict the melt extraction rates, fluxes, and characteristic timescales, and, importantly, our results suggest that crystal shape plays a first-order role in melt extraction because the timescales λ are proportional to permeability $\lambda \propto k^{-1} \propto s^2$. Mush permeability exerts a first order control over the rates of this process, and hence crystal shape effects need to be accounted for using our model.

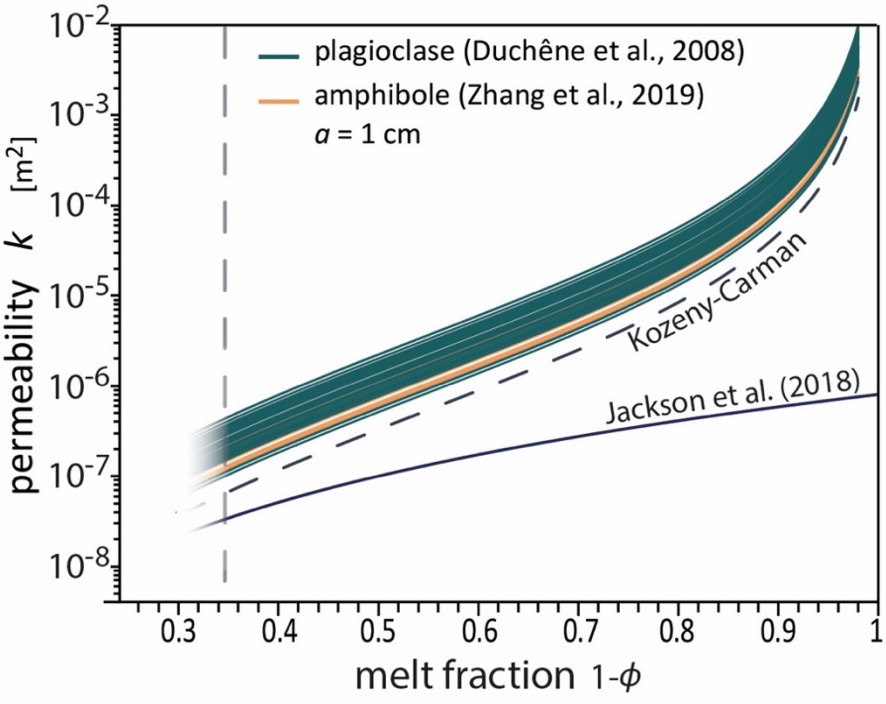

Figure 3.4. The model (Eq. 3) solved using input 3D crystal shapes for amphibole (Zhang et al., 2019) and plagioclase (Duchene et al., 2008) phenocrysts (shortest crystal axis length is set to $a = 1$ cm). Our model is compared with the scaling from Jackson et al. (2018) $k = a^2\beta\phi^n$ where $\beta = 1/125$ and $\alpha = 3$ are the parameters proposed (Jackson et al. 2018). We also give a classical Kozeny-Carman model of the form $k = (1-\phi)^3 a^2/[150(\phi)^2]$ (e.g. Torquato 2013). Both of these comparisons substantially underpredict plagioclase and amphibole mush permeabilities given here. The vertical line at $\phi = 0.35$ is for comparison across models and corresponds to a hypothetical natural mush maximum packing fraction.

Acknowledgments

Funding was provided via a Durham University 'Durham Doctoral Studentship' (provided to Bretagne) and via both the Natural Environment Research Council (grants NE/T000430/1 and NE/M018687/2) and the European Research Council (834225 EAVESDROP). We acknowledge the authors of Liu et al. (2017) for providing their 3D digital domains. Comments from Chris Huber, Marian Holness, and an anonymous reviewer improved the manuscript substantially.

References

Allan, A.S.R., Morgan, D.J., Wilson, C.J.N. and Millet, M.A., 2013. From mush to eruption in centuries: assembly of the super-sized Oruanui magma body. *Contributions to Mineralogy and Petrology*, *166*(1), pp.143-164.

Bachmann, O. and Bergantz, G.W., 2008. Rhyolites and their source mushes across tectonic settings. *Journal of Petrology*, *49*(12), pp.2277-2285.

Bachmann, O. and Bergantz, G.W., 2004. On the origin of crystal-poor rhyolites: extracted from batholithic crystal mushes. *Journal of Petrology*, *45*(8), pp.1565-1582.

Clemens, J.D. and Petford, N., 1999. Granitic melt viscosity and silicic magma dynamics in contrasting tectonic settings. *Journal of the Geological Society*, *156*(6), pp.1057-1060.

Delaney, G., Cleary, P., Sinnott, M. and Morrison, R., 2010. Modelling non-spherical particle breakage in DEM simulations.

Deng, N., Wautier, A., Thiery, Y., Yin, Z.Y., Hicher, P.Y. and Nicot, F., 2021. On the attraction power of critical state in granular materials. *Journal of the Mechanics and Physics of Solids*, *149*, p.104300.

Donev, A., Cisse, I., Sachs, D., Variano, E.A., Stillinger, F.H., Connelly, R., Torquato, S. and Chaikin, P.M., 2004. Improving the density of jammed disordered packings using ellipsoids. *Science*, *303*(5660), pp.990-993.

Duchêne, S., Pupier, E., De Veslud, C.L.C. and Toplis, M.J., 2008. A 3D reconstruction of plagioclase crystals in a synthetic basalt. *American Mineralogist*, *93*(5-6), pp.893-901.

Floess, D., Caricchi, L., Simpson, G. and Wallis, S.R., 2019. Melt segregation and the architecture of magmatic reservoirs: insights from the Muroto sill (Japan). *Contributions to Mineralogy and Petrology*, *174*(4), pp.1-15.

Hartung, E., Weber, G. and Caricchi, L., 2019. The role of H2O on the extraction of melt from crystallising magmas. *Earth and Planetary Science Letters*, *508*, pp.85-96.

Hersum, T., Hilpert, M. and Marsh, B., 2005. Permeability and melt flow in simulated and natural partially molten basaltic magmas. *Earth and Planetary Science Letters*, *237*(3-4), pp.798-814.

Hildreth, W., 1981. Gradients in silicic magma chambers: implications for lithospheric magmatism. *Journal of Geophysical Research: Solid Earth*, *86*(B11), pp.10153-10192.

Holness, M.B., 2018. Melt segregation from silicic crystal mushes: a critical appraisal of possible mechanisms and their microstructural record. *Contributions to Mineralogy and Petrology*, *173*(6), pp.1-17.

Huang, H.H., Lin, F.C., Schmandt, B., Farrell, J., Smith, R.B. and Tsai, V.C., 2015. The Yellowstone magmatic system from the mantle plume to the upper crust. *Science*, *348*(6236), pp.773-776.

Huber, C., Bachmann, O. and Manga, M., 2010. Two competing effects of volatiles on heat transfer in crystal-rich magmas: thermal insulation vs defrosting. *Journal of Petrology*, *51*(4), pp.847-867.

Jackson, M.D., Blundy, J. and Sparks, R.S.J., 2018. Chemical differentiation, cold storage and remobilization of magma in the Earth's crust. *Nature*, *564*(7736), pp.405-409.

Liu, B. and Lee, C.T., 2021. Fast melt expulsion from crystal-rich mushes via induced anisotropic permeability. *Earth and Planetar*

Liu, T., Lin, B. and Yang, W., 2017. Impact of matrix–fracture interactions on coal permeability: model development and analysis. *Fuel*, *207*, pp.522-532.

Llewellin, E.W., 2010. LBflow: An extensible lattice Boltzmann framework for the simulation of geophysical flows. Part I: theory and implementation. *Computers & Geosciences*, *36*(2), pp.115-122.

Llewellin, E.W., 2010. LBflow: An extensible lattice Boltzmann framework for the simulation of geophysical flows. Part II: usage and validation. *Computers & geosciences*, *36*(2), pp.123-132.

Lorensen, W.E. and Cline, H.E., 1987. Marching cubes: A high resolution 3D surface construction algorithm. *ACM siggraph computer graphics*, *21*(4), pp.163-169.

Meng, L., Jiao, Y. and Li, S., 2016. Maximally dense random packings of spherocylinders. *Powder Technology*, *292*, pp.176-185.

Mueller, S., Llewellin, E.W. and Mader, H.M., 2010. The rheology of suspensions of solid particles. *Proceedings of the Royal Society A: Mathematical, Physical and Engineering Sciences*, *466*(2116), pp.1201-1228.

Petford, N., Koenders, M.A. and Clemens, J.D., 2020. Igneous differentiation by deformation. *Contributions to Mineralogy and Petrology*, *175*(5), pp.1-21.

Petford, N., 1995. Segregation of tonalitic-trondhjemitic melts in the continental crust: The mantle connection. *Journal of Geophysical Research: Solid Earth*, *100*(B8), pp.15735-15743.

Pistone, M., Baumgartner, L.P., Bégué, F., Jarvis, P.A., Bloch, E., Robyr, M., Müntener, O., Sisson, T.W. and Blundy, J.D., 2020. Felsic melt and gas mobilization during magma solidification: An experimental study at 1.1 kbar. *Frontiers in Earth Science*, *8*, p.175.

Röding, M., Ma, Z. and Torquato, S., 2020. Predicting permeability via statistical learning on higher-order microstructural information. *Scientific reports*, *10*(1), pp.1-17.

Rudge, J.F., Holness, M.B. and Smith, G.C., 2008. Quantitative textural analysis of packings of elongate crystals. *Contributions to Mineralogy and Petrology*, *156*(4), pp.413-429.

Sparks, R.S.J. and Cashman, K.V., 2017. Dynamic magma systems: Implications for forecasting volcanic activity. *Elements*, *13*(1), pp.35-40.

Torquato, S., 2013. *Random heterogeneous materials*. Springer

Vasseur, J. and Wadsworth, F.B., 2017. Sphere models for pore geometry and fluid permeability in heterogeneous magmas. *Bulletin of Volcanology*, *79*(11), pp.1-15.

Vasseur, J., Wadsworth, F.B. and Dingwell, D.B., 2020. Permeability of polydisperse magma foam. *Geology*, *48*(6), pp.536-540.

Vasseur, J., Wadsworth, F.B., Coumans, J.P. and Dingwell, D.B., 2021. Permeability of packs of polydisperse hard spheres. *Physical Review E*, *103*(6), p.062613.

Wouterse, A., Williams, S.R. and Philipse, A.P., 2007. Effect of particle shape on the density and microstructure of random packings. *Journal of Physics: Condensed Matter*, *19*(40), p.406215.

Zhang, B., Hu, X., Asimow, P.D., Zhang, X., Xu, J., Fan, D. and Zhou, W., 2019. Crystal size distribution of amphibole grown from hydrous basaltic melt at 0.6–2.6 GPa and 860–970 C. *American Mineralogist: Journal of Earth and Planetary Materials*, *104*(4), pp.525-535.

Chapter 4 : A universal scaling for the permeability of magma mush

A scaling for the permeability of loose magma mush validated using X-ray computed tomography of packed confectionary in 3D and estimation methods from 2D crystal shapes

Chapter preamble

This chapter is ready for imminent submission in *Contributions to Mineralogy and Petrology* with the following citation:

Bretagne, E., Wadsworth, F.B., Vasseur, J., Dobson, K. J, A scaling for the permeability of loose magma mush validated using X-ray computed tomography of packed confectionary in 3D and estimation methods from 2D crystal shapes, *in prep.*

The author contribution by the PhD candidate amounts to 60% of the content, and the manuscript draft presented here was authored solely by the PhD candidate.

Melt percolation through partially molten 'mushy' regions of the crust underpins models for magma migration, accumulation, and processes that prime systems for eruption. Knowledge of the hydraulic properties of magma mush, especially permeability, is required for accurate predictions of melt migration rates and accumulation timescales. Here, we present and characterize X-ray computed tomography 3D datasets of magma mush analogues made from packed confectionary particles arranged randomly in a volume. We extract the porosity, specific surface area, particle geometry, and particle size distribution and use a lattice-Boltzmann fluid flow simulation tool to determine the permeability of the melt phase network between the packed particles. Using these datasets, we test a model for permeability of granular materials, finding excellent agreement with our datasets to within ~0.1 log units, when the specific surface area is taken as a measured value. To extend this to more typical cases where the specific surface area is an unknown variable, we additionally use the shape and size of the objects determined in both 3D and 2D to estimate the specific surface area assuming a cuboid approximation. These approximate solutions give good results to within ~0.5 log units of the measured permeability and offer a method by which permeability could be estimated from a thin section of a cumulate or pluton sample. Our approach is more accurate than existing models for permeability of magma mush which take a spherical approximation,

and therefore we propose that these could be implemented in dynamic magma mush models for melt movement in the crust.

Keywords: percolation; igneous petrology; melt extraction; trans-crustal; magma chamber

4.1 Introduction

The dynamics of magma movement through the Earth's crust remain poorly understood. The leading models contend that magmas accumulate in the crust through repeated intrusive emplacement as mush – a framework of packed and variably intergrown or overgrown crystals with an interstitial melt phase. Upon emplacement, melts can migrate relative to and through the magma mush (Bachmann & Bergantz 2004; Annen, 2009; Cashman et al. 2017; Jackson et al. 2018; Sparks et al. 2019). Therefore, for large portions of the system, the advection of melt from one place to another is hosted in a porous medium, the solid static framework of which is a complex 3D manifold of crystal phases. This means the key parameter that can limit the rates and fluxes of melt through the system is the permeability of the mush. While all crust-scale models require permeability to compute fluxes (Bachmann & Bergantz, 2004; Jackson et al. 2018), there has been relatively little work to constrain the permeability beyond first-order scaling approaches.

While the exact physical processes are debated (c.f. Holness 2018; Liu & Lee 2021), the extraction of melts from mushes primes some magmatic systems to erupt voluminous crystal-poor silicic magmas in very large eruptions (Bachmann & Bergantz 2004; Hildreth & Wilson, 2007; Wilson et al. 2021). Therefore, while understanding mush permeability is important for predicting melt migration in general, it may also hold the key to understanding the timescales of melt extraction prior to Earth's largest eruptions.

Typically, the permeability k of mushy magma is predicted using a general scaling such as $k = a^2\beta\phi_m^3$ (Jackson et al. 2018), where, a is the crystal 'size', ϕ_m is the melt fraction interstitial to the crystals, and β is a constant. This approach encompasses the widely used Kozeny-Carman formulation $k = \phi_m^3 a^2/(150(1-\phi_m)^2)$, for which $\beta = 1/(150(1-\phi_m)^2)$ (e.g. Bachmann & Bergantz 2004). In these models, complex crystal habits and multi-component mushes are reduced to a single size parameter a, despite evidence that that the shape of the objects defining the solid framework in a porous medium has a first-order effect on the possible packing geometries (e.g. Liu et al. 2017) and the resulting permeability at those packings (c.f. chapter 3). Here, we move beyond idealized shapes and test more sophisticated permeability

models against packs of realistic particles explicitly. Our aim is to constrain the efficacy of magma mush permeability models.

4.2 Developing a model hypothesis

The simplest and most widely used model for the permeability k of packed particles is the Kozeny-Carman model (Ergun, 1952). While this model is given in a variety of forms, sometimes including additional parameters such as a pore network tortuosity, and the specific lengths of pores or particles, the more general form is

$$k = \frac{\phi_m^3}{Cs^2} \qquad \text{Eq. 1}$$

where ϕ_m is the volume fraction of the non-particle phase, C is a constant, and s is the specific surface area of the pore space (Torquato, 2013; Röding et al. 2020; Vasseur & Wadsworth, 2017; Wadsworth et al. 2017; Vasseur et al. 2021; 2022). In the case of magma mush, we can think of ϕ_m as being the melt volume fraction, and then $\phi = 1 - \phi_m$ representing the crystal volume fraction (assuming a two-phase system). In general, across a very wide range of porous media, $C \approx 5$ appears to result in a good match between Eq. 1 and empirical data when the medium is statistically representative and isotropic (Torquato, 2013; Vasseur et al. 2021). While C appears independent of the medium, and ϕ can be readily determined using image analysis tools or laboratory methods, it only remains to constrain s. If we take $s = 3(1 - \phi_m)/R$ as the specific surface area of monodispersed spheres of radius R in a volume (sphere volume fraction $1 - \phi_m$) Eq. 1 becomes the more familiar $k = \phi_m^3 R^2/(9C(1 - \phi_m)^2)$. For magma mush, a model of this form is used commonly (e.g. Bachmann & Bergantz, 2004[1]).

For cuboids with three independent axis lengths a, b, and c, the s is given explicitly by (adapted from c.f. chapter 3)

$$s = 2(1 - \phi_m)\left(\frac{1}{a} + \frac{1}{b} + \frac{1}{c}\right) \qquad \text{Eq. 2}$$

[1] We note that in their original paper, Bachmann & Bergantz give $(1 - \phi_m^2)$ in place of $(1 - \phi_m)^2$, which we assume is a typographic error.

and so for packs of cuboids, the Kozeny-Carman law given in Eq. 1 becomes

$$k = \frac{\phi_m^3}{4C(1-\phi_m)^2}\left(\frac{1}{a}+\frac{1}{b}+\frac{1}{c}\right)^{-2} \quad \text{Eq. 3}$$

This implies that if the cuboid lengths a, b, and c and the melt fraction ϕ_m can be determined, so too can the permeability. In chapter 3, we validated the efficacy of Eq. 3. for 3D simulated volumes of packed cuboids for which $b = c$ (i.e. square-ended cuboids), However, some key aspects of this hypothesis still require testing, specifically does Eq. 3 remain valid for: (1) cuboids for which $b \neq c$; (2) particles that are not cuboids; and (3) given the sensitivity of k to s (via s^2 in Eq. 1), is Eq. 3 valid for rough particles. Here, we provide the results of these tests.

Eq. 3 is a dimensional form, which means that it is scale-dependent and k depends on not only the relative ratios of a, b, and c, but also on the magnitude of a, b, and c. In order to compare simulation results or empirical data across scales, while still testing Eq. 3, we can introduce a scaling parameter, which is a reference permeability. We choose $k_s = 2(1-\phi_m)/s^2$ (c.f. chapter 3), which is a so-called 'Stokes permeability' (Martys et al. 1994; Wadsworth et al. 2016; Vasseur et al. 2021). For some idealized systems of solid spheres in a volume, the Stokes permeability is the limiting value of k as $\phi_m \to 1$ and is related to Stokes law for the drag around a sphere. If we divide Eq. 1 by this value, we retrieve a dimensionless permeability $\bar{k}$ that should be universal and scale independent and applicable across a wide range of mush types in nature and the laboratory (Vasseur et al. 2021; 2022)

$$\bar{k} = \frac{k}{k_s} = \frac{{\phi_m}^3}{2C(1-\phi_m)}. \quad \text{Eq. 4}$$

4.3 Materials and methods

4.3.1. Methods to test the permeability model

In the crust, mush is often not crystals packed in melts to their random close packing limit; instead, it is an interlocking framework of moderately or thoroughly intergrown crystals (e.g. Sparks et al. 2019). But there are also clear examples of what we termed 'loose mush' in chapter

3, where the degree of inter-growth is minimal and the mush is closer to a pack of near-separate crystals in a melt volume (Holness et al. 2019). It is these loose mush materials that we emulate here. To create real loose mush analogues in the laboratory with a range of particle geometries, we represent the crystals by confectionary: either near cubic or cuboidal shape, smooth faced fudge chunks, or non-cuboid rough sugar crystals (Fig. 4.1).

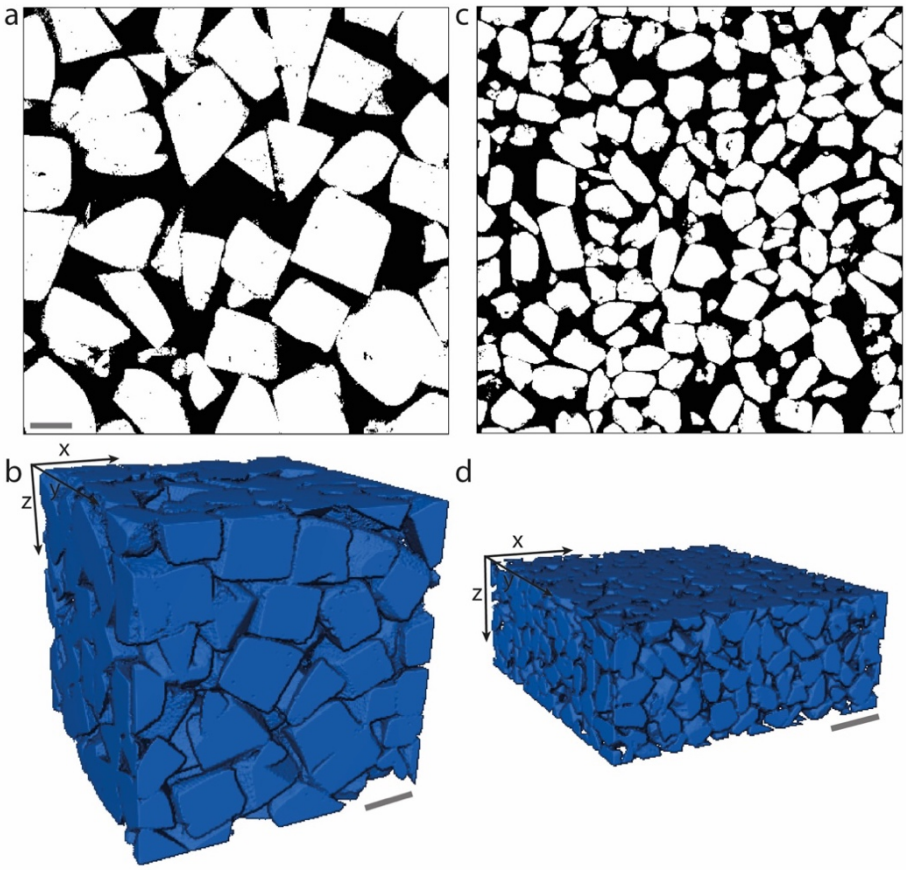

Figure 4.2: Renderings of (a-b) the packed fudge chunks, and (c-d) the packed sugar crystals in (a,c) 2D slice representation and (b,d) in 3D. In 2D representations, the scale bar represents 100 μm and in 3D, the scale bar is 200 μm. No border kill is applied on these outputs because these are the full domains $f = 1$ required for LBflow

We load particles randomly into a 20 mm diameter cylindrical centrifuge tube, ensuring at least 10 particles can fit across the cylinder diameter. The cylinders are shaken slightly to settle the particles into a relatively close to a random close pack, and then imaged using a Nikon XTH LC 225kV 225W Ultrafocus laboratory X-ray tomography scanner at the University of Strathclyde. Scans were performed at 90 kV (either 91 μA and 2s exposure, or 209 μA and 1 second exposure depending on scan) and were reconstructed using the built-in algorithms to give a 2000 voxel image with 16 μm voxel resolution. Visualisation and quantification were performed using Avizo©, and the data segmented into binary images showing the pore and

solid networks. These binary images were loaded into the lattice-Boltzmann fluid flow simulation tool LBflow (Llewellin et al. 2010a; 2010b) which is designed for determining the permeability of complex porous media. LBflow has been validated or applied using sphere packs in cubic lattice arrangements (Llewellin 2010b; Wadsworth et al. 2017), random overlapping sphere packs (Vasseur & Wadsworth 2017; Vasseur et al. 2020), hard sphere packs (Vasseur et al. 2021; 2022), hexagonal arrays (Vasseur & Wadsworth 2019), fibrous porous media (Nabovati et al. 2009), sintering systems (Wadsworth et al. 2017; 2021), and basalt pore spaces (Macente et al. 2022). The specific surface area s of the particle packs we use a marching cubes algorithm (Lorensen & Cline, 1987) from Python's scikit-image toolbox (following Lewiner et al. 2003). This workflow yields k, s, and ϕ_m, allowing explicit validation of Eq. 4.

As we also aim to test Eq. 2 so show how Eqs. 3 & 4 can be used without explicitly measuring s, (not always possible in many situations of interest), we performed a separation using the *separation* algorithm in Avizo© to enable measurement of the 3D shape parameters of every complete particle within the image volume and measured the principal component (orthogonal axis) lengths and 3D shape parameters. The values of a, b, and c can be used without *a priori* knowledge of s.

4.3.2. Methods to additionally test the effect of surface roughness

Although the scans we collected are sufficient to accurately resolve particle edges and surfaces, we can also numerically roughen the images by a factor f, applying a rescale algorithm to the datasets without an anti-aliasing filter, which effectively combines locally adjacent voxels (using scikit-image toolbox, from $f = 1$ to $f = 0.10$) (Fig. 4.2). The value $f = 1$ represents no down sampling applied. With each roughened dataset, we apply LBflow to determine the permeability k and the marching cubes algorithm to determine s. Our data show the efficacy of our scaling crystals with non-smooth edges, but we acknowledge that this cannot readily be used without prior knowledge of s because the particles at low-f are clearly non-cuboidal. While Eq. 2 is not strictly valid when the particles are non-cuboidal, the relationship $k \propto s^{-2}$ given by Eq. 1 can still be tested.

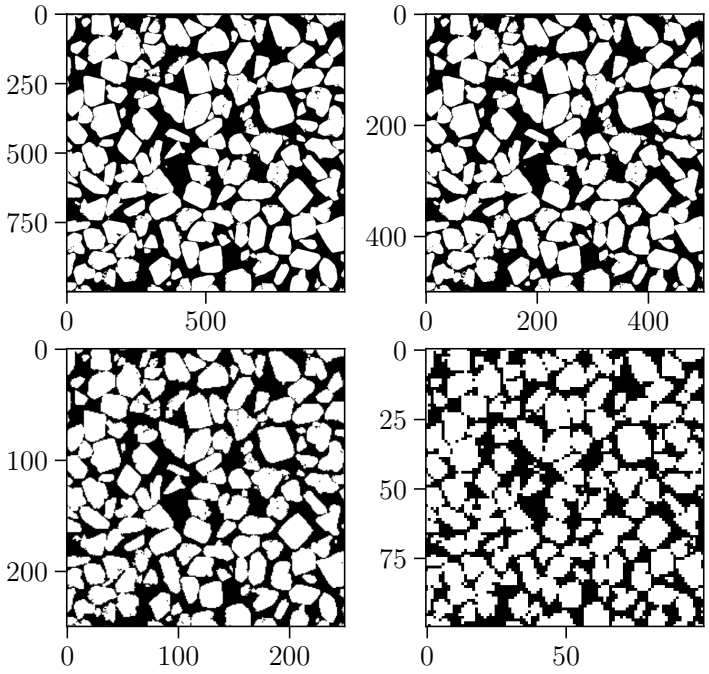

Figure 4.2. An example output from the roughening algorithm for (a) $f = 1$ (i.e. the domain as measured), (b) $f = 0.50$, (c) $f = 0.25$, and (d) $f = 0.10$ applied to the sugar crystals dataset. The values on the x- and y-axes are the voxel counts.

4.4 Results and analysis

The geometry of the first dataset is cubic or cuboidal with relatively smooth-edges compared with the sugar particles which are anisometric and rough-edged (Fig. 4.1); and represent a variable and harsh test of the simple models presented in Section 2. We test both the universal dimensionless model (Eq. 4) and the dimensional model with different methods of predicting s. In all cases, raw data for k, s, and ϕ are given in Table 4.1. k is determined in all three principal directions, however we discuss the results of the average of those values and use the standard deviation on that average to compute uncertainties via a standard error (for example, in Fig. 4.3).

4.4.1. Results using the measured specific surface area

The output values of k can be used with the of k can be used with the measured s and ϕ_m to define $\bar{k} = ks^2/(2(1-\phi_m))$, which represents the dependent variable on the left-hand-side of Eq. 4. Regardless of whether the data have been roughened ($f < 1$; see Section 3b) or not ($f = 1$), the data collapse to a cluster relatively close to the model with $C = 5$ (Röding et al. 2020; Fig. 4.3a) demonstrating that the roughening does not affect the universality of Eq. 4 when s is known. If we let C be an adjustable parameter, we can use a least-squares regression

technique to minimize for the value of C. Given the relatively small differences in ϕ_m across all data, this is done by minimizing for the logarithm of the $\bar{k}$ data. We perform this minimization using all data (including the numerical cuboid data from chapter 3) or with each dataset individually (Table 4.2, Fig. 4.3b) and show the result with the best-fit C for the combination of the fudge and sugar crystals (i.e. $C = 4.01 \pm 0.24$). Regardless of the value of C, the slope in Fig. 4.4 matches well the Eq. 4 prediction.

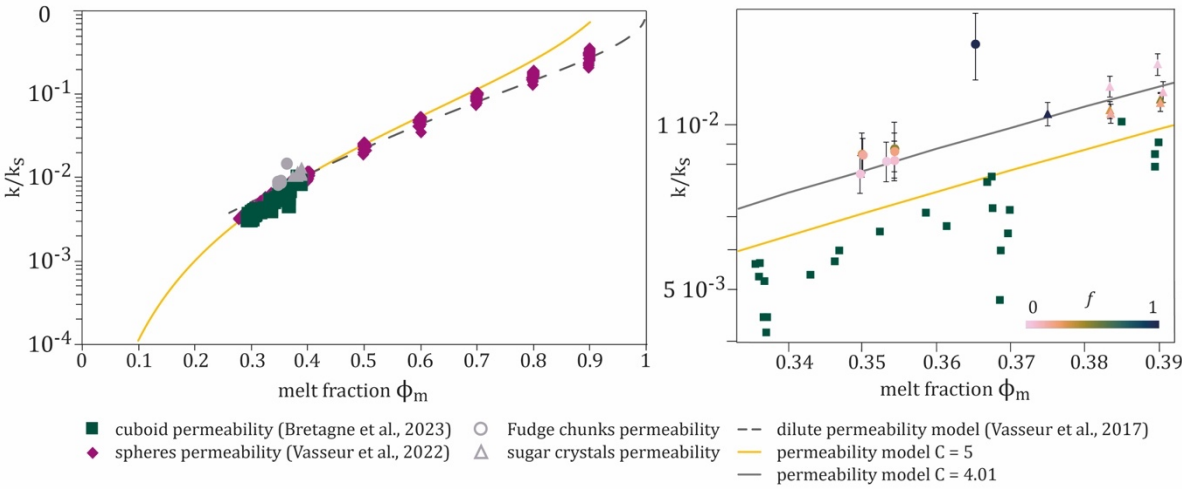

Figure 4.3: The normalized permeability $\bar{k}$ as a function of the inter-particle phase volume fraction ϕ_m with measured s. (a) The data from this study with roughened particles $f < 1$ values and non-roughened particles at $f = 1$. (b) A zoom-in on the data from (a) and including the best-fit Eq. 4. Also shown are the data from chapter 3 for cuboid simulations, and the model (Eq. 4) with $C = 5$. For comparison we show hard sphere simulations from Vasseur et al. (2021; 2022) and a hard-sphere model (Sangani & Acrivos 1982), which approaches the prediction of Eq. 4 at moderate ϕ_m.

For comparison, Fig. 4.3 also shows the data for hard sphere simulations (Vasseur et al. 2021; 2022) and an associated model specifically for the permeability between hard spheres in cubic lattices (Sangani & Acrivos, 1982; Llewellin, 2010b; Vasseur & Wadsworth 2017). This is shown here for completeness, and to demonstrate that solutions for spherical particles can, if scaled correctly, provide similar universal results as those for anisometric particles such as cuboids, fudge, and sugar.

4.4.2. Using the cuboid approximation to find the specific surface area

The measured *a, b, c* axes for each particle are used to define the specific surface area of each via Eq. 2, and because there is a distribution of axis lengths in each sample, we then take an average of each of these which we term $\langle a \rangle$, $\langle b \rangle$, and $\langle c \rangle$, respectively. The standard deviation σ on each of those averages is set as the error on the axis length distributions (σ_a, σ_b, and σ_c). For the fudge chunks, $N = 79$ and for the sugar crystals, $N = 361$. These are used to determine

s and an uncertainty on s (using Eq. 2), assuming that this represents an approximate s from the average crystal shape in the pack. The output of these steps is a value for k_s derived from the crystal shape determinations, and which can be used to compute $\bar{k}$ for each sample. We test this with the un-roughened data at $f = 1$ because the approach here relies on the data being close to cuboidal and smooth.

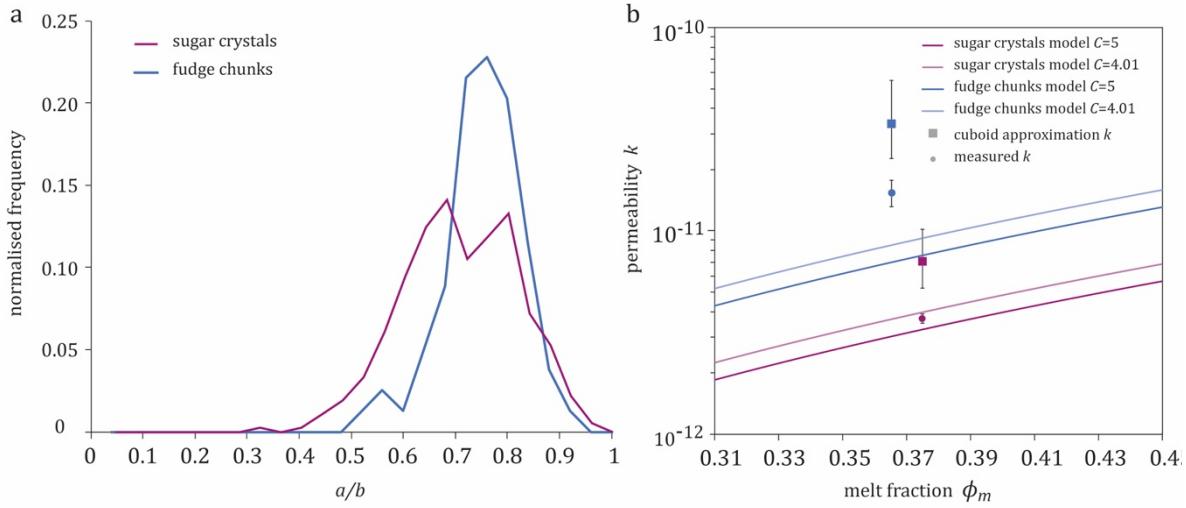

Figure 4.4. (a) The distribution of crystal lengths in the fudge chunks sample, and the sugar crystal sample. (b) The permeability of the fudge chunks and the sugar crystals using two methods: (1) using the measured s (as given in Fig. 3); and (2) using s predicted by the cuboid approximation using the mean values given in (a) and the associated errors.

In Fig. 4.4, we show the result of the steps outlined above for the pack of fudge chunks and the pack of sugar crystals. In Fig. 4.4a, we show the normalized count distribution of the crystal size for each sample. And in Fig. 4.4b we show the result of the computation of k. We do this in dimensional space (i.e. k and not $\bar{k}$; using Eq. 3 and not Eq. 4). The difference between the data computed using the cuboid approximation, and the same data for which s is measured directly is a difference of less than 0.5 log units of k in the case of both the sugar and fudge chunks. We conclude therefore that any prediction made using the model presented here (Eq. 3) with a cuboid approximation for the specific surface area, can be accurate to within 0.5 log units when $C = 4.01$.

4.5 Discussion

Here we explore and extend our results in a few key ways. First, we provide the limits of applicability of our models. Second, we propose a method to find the permeability from a 2D

thin section of a cumulate rock. And third, we explore the implications of our findings for real mush systems.

4.5.1. The limits of applicability at high and low melt volume fraction ϕ_m

Like all scaling approaches, the model tested here has limits beyond which it should not be applied. The limits as $\phi_m \rightarrow 1$ are best understood by comparing the prediction of Eq. 4 with those given by the dilute expansions of k_s (i.e. the 'Stokes permeability'). These two competing predictions converge at the range of ϕ_m that packed particles used here occupy (see Fig. 4.4). However, as particle packing densities ϕ drop (i.e. as ϕ_m increases) the dilute expansion model fits better. The point at which our universal model and the dilute model diverge substantially ($\phi_m \geq 0.6$) provides a good upper limit of applicability of Eq. 4, and is consistent with arguments given in Vasseur & Wadsworth 2017). Using Eq. 4 at $\phi_m \geq 0.6$ will overestimate the permeability of mush. The limits as $\phi_m \rightarrow 0$ below which Eq. 4 should not be used is formally given by the maximum random close packing of particles, which occurs at a particle volume fraction ϕ'. In chapter 3, we propose a functional form for this value as a function of the aspect ratio of square-ended cuboids. However, here, with triaxial cuboids, this function is not strictly valid and ϕ' is not well known. At $\phi > \phi'$ magma mush is no longer 'loose' and some intergrowth, overgrowth, or deformation of the crystals must have occurred (Holness 2018; c.f. chapter 3). The lowest ϕ_m determined in chapter 3 was approximately $\phi_m = 0.35$ and therefore we consider this value the lower limit of applicability of the model presented here (Eq. 4). Based on these arguments, the model applicability window is $0.35 \leq \phi_m \leq 0.60$. Below these limits, a percolation model is required (e.g. Martys et al. 1994; Wadsworth et al. 2016; Vasseur & Wadsworth 2017; Vasseur et al. 2021; 2022), and above these limits a dilute expansion model is required (Sangani & Acrivos, 1982; Vasseur et al. 2021; 2022).

4.5.2. Finding a permeability from a 2D thin section

Using standard petrological methods, it is rare to have the kind of 3D data presented here, especially for silicic magmas. The most widely used X-ray computed tomography (XCT) methods can be highly effective when there is an attenuation contrast between the 'mush' and 'melt' phases. In our analogue samples, the interstitial volume was air, and so the high attenuation contrast makes segmentation of phases easy, and ϕ_m allows easy separation of the individual particles. In natural cumulate samples – an erupted and quenched piece of magma mush – the interstitial melt can solidify or crystallise into the same phases as the mush (e.g.

Wager et al., 1960; Morse, 1998; Humphreys, 2009), or into phases with only a small attenuation contrast, making the segmentation and separation processes challenging. More advanced phase contrast XCT and diffraction contrast tomography that can support effective image analysis for samples with low contrast is now widely accessible.

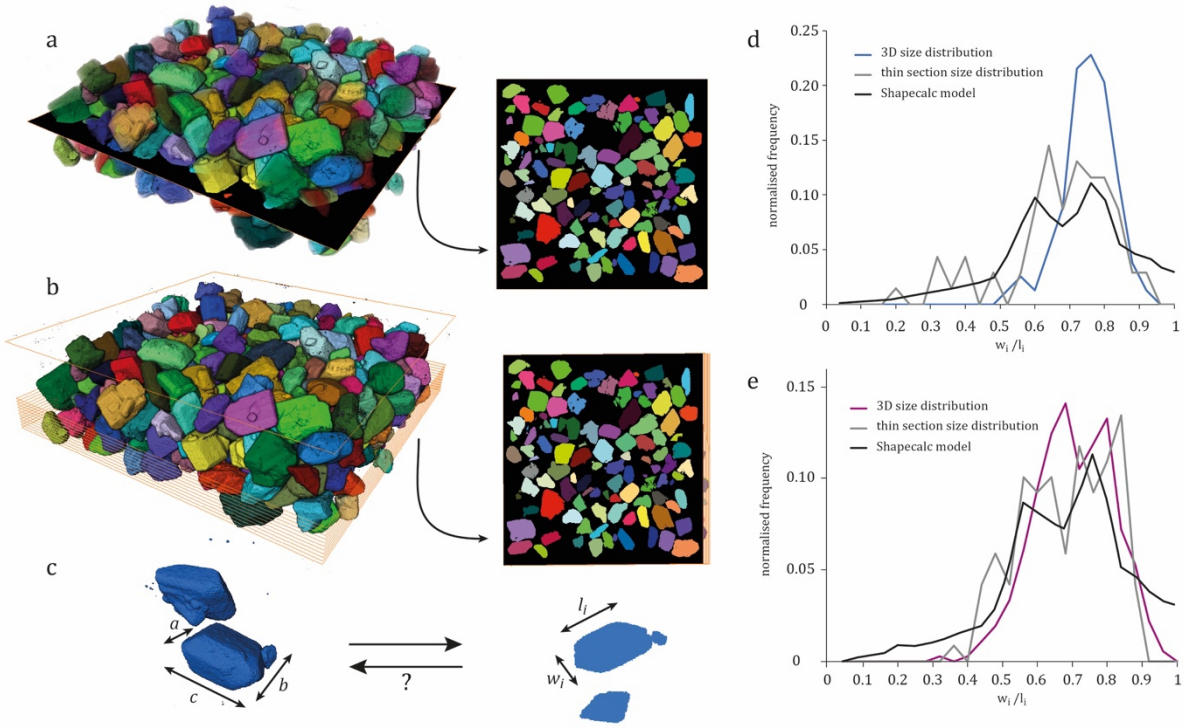

Figure 4.5. The process of taking a layer of 3D particles and generating a 2D slice and associated 2D w and l data. (a) An example of a 2D slice from the stack of slices. (b) A 3D render of fudge chunks with a sequence of 2D 'virtual sections' cut through it. (c) Defining the cuboid axis in 3D and in 2D. (d) and (e) show the associated distributions of the ratio w_i/l_i that are found from analysing the shapes in (a) and (b), respectively. Also shown in (d) and (e) are the best-fit ShapeCalc (Mangler et al. 2022) distributions of cuboid cuts, which relates to a best-fit single cuboid shape.

2D techniques such as thin section microscopy is far more common, and so we test a workflow for retrieving a representative 3D permeability value from 2D data. First, we define a 2D 'slice' through the 3D volumes to generate a virtual thin section. This method effectively cuts the crystals in a plane and, depending on the orientation of the crystals, will result in a distribution of intersection length-scales (Fig. 4.5). We then extract the maximum and minimum axis lengths of each particle that we can observe in the 2D plane, which we term w_i and l_i, respectively (Figs 4.5a & 4.5c). As these 2D slices are virtual, we can produce multiple thin sections in many orientations and locations within the larger sample, effectively generating many pseudo-thin section datasets (Fig. 4.5b). The distributions of the measured w_i/l_i ratios

(Figs 4.5d & 4.5e) cannot be used directly with Eq. 2, because their relationship to to a, b, and c (the three 'true' axes) of the 3D objects needs to be established.

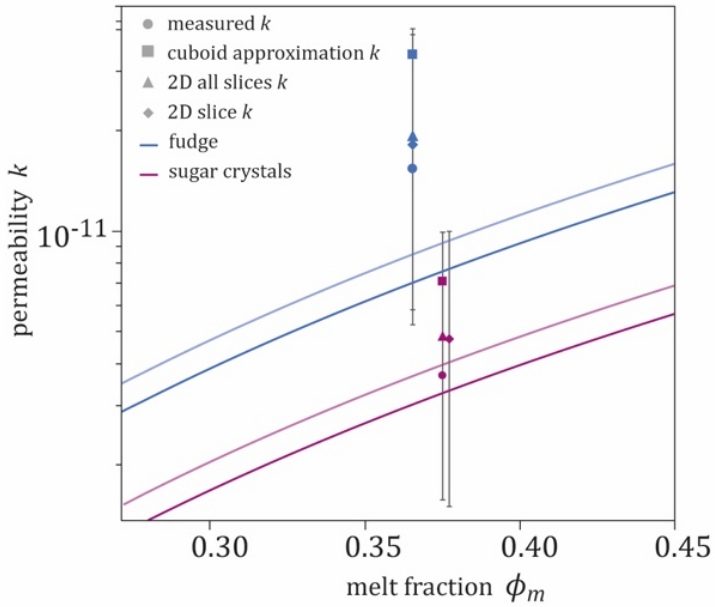

Figure 4.6. The results of the 2D-to-3D approach outlined here, compared with the direct result from LBflow shown in Fig. 4.4 and the model given by Eq. 3. The difference between the data from LBFlow and the projected 2D slice data (lozenges) is only of 0.07 orders of magnitude and 0.11 orders of magnitude for the fudge bits and the sugar crystals, respectively. The difference between the data from LBFlow and the projected 2D all slice data (triangles) is only of 0.10 orders of magnitude and 0.12 orders of magnitude for the fudge bits and the sugar crystals, respectively. The uncertainty on k in the 2D-to-3D method arises from propagating the uncertainty on a, b, and c from the standard deviation of w_i and l_i, which can be substantial.

To estimate the true axis lengths and allow direct application of our model, we use ShapeCalc (Mangler et al. 2022), which allows prediction of the 3D shape of the crystals from the distribution of w_i and l_i measured on a 2D dataset. This model yields normalised axis lengths s, the small axis, i, the intermediate axis, and l, the long axis. These represent the true axis lengths a, b, and c normalised to a, such that $s = a/a = 1$, $i = b/a$ and $l = c/a$. Higgins (1994) demonstrated that for a population of randomly oriented anisotropic 3D objects of same size and shape, the intersection long axis l_i is close to the true intermediate axis b and the intersection short axis w_i is close to the true short axis a. Therefore, $l_i \approx b$ or $w_i \approx a$. If we assume $a = w_i$, then we have $b = i\, w_i$ and $c = l\, w_i$.

Applying this workflow, we can then apply Eq. 2 and Eq. 4 to the 2D virtual section data. We find that this approach works very well (Fig. 4.6), and the propagated uncertainty on the output permeabilities is within error of both the model (Eq. 3) and the measured result from LBflow with the marching cubes algorithm to find s. This demonstrates that our model, coupled with

ShapeCalc, can be used to convert 2D thin section observations of packed crystal geometries, into a bulk material permeability for individual cumulate samples.

4.5.3. Anisotropic mush permeability and the fabric tensor

Eqs 1, 3, and 4 are all isotropic models that do not predict a full permeability tensor, nor a permeability that depends on shear strain in any manner. This is consistent with the widely used models that are embedded in magma mush melt migration solutions (Bachmann & Bergantz 2004; Jackson et al. 2018) and indeed in general formulations for melt migration in analogous partially molten systems (e.g. McKenzie 1984) or compaction of crystal-rich plugs even in flowing systems (e.g. Lecampion & Garagash 2014). However, the melt percolation and extraction timescales from mush predicted from these extraction models are often many orders of magnitude in timescale slower than recorded by chronometers that track extraction processes (e.g. Holness 2018). This has led to models that invoke shear strain and a resultant anisotropy development driving high permeability in one direction, perhaps at the expense of efficient permeable channels in the perpendicular direction (Liu & Lee, 2018), and large-scale simulations of mush dynamics that show kinematics involve the definition and evolution of a fabric tensor (Bergantz et al. 2017). This fabric tensor could be used to compute a local but volume-averaged permeability tensor description (Bergantz et al. 2017). In any anisotropic model, the scaling for permeability via a scalar specific surface area (e.g. Eq. 1) will not hold, or will require additional scaling via a fabric deformation correction.

While our model is not applicable to anisotropic systems, our approach grounds solutions in the specific microstructures of mushes, accounting for the complex crystal morphologies involved, and so provides a clear direction for developing the anisotropic models, from readily producible textures produced easily in a laboratory setting and amenable to X-ray computed tomography techniques.

Our model formulation is specific to what we term ‘loose mush’. That is, mush for which crystal-crystal intergrowth or overgrowth is minimal, and for which the mush is isotropic and simply analogous to crystals at their maximum random close packing fraction. Therefore, a tenable future step would be to extend these models to *overlapping* cuboid systems where ϕ_m can drop to values below the limits explored here (see Section 5a). Indeed, for overlapping objects in a volume, ϕ_m can drop to a critical value below which the system as a whole becomes impermeable – termed the percolation threshold ϕ_c (Vasseur and Wadsworth, 2017; Colombier et al. 2020; Wadsworth et al. 2021). This parameter has not been determined for systems of

magma mush, but constraint of this critical percolation property, as well as s down to low-ϕ_m would allow permeability models to be extended down from the 'loose mush' regime into the 'intergrown mush' regime.

4.6 Conclusions

Magma mush comprises anisometric crystals that are variably intergrown with one another or overgrown by additional phases. We have expanded the relatively simple biaxial cuboid model presented in chapter 3 to account for the triaxial nature of natural cuboidal crystals. We have validated that expanded form of the model using real X-ray computed tomography data for mush analogues, and identified the need for a minor adjustment of the constant C (albeit with reasonable efficacy for the forward model with $C = 5$). We have also shown that the model is accurate to within $0.2 - 0.5$ log units when the axes of particles approximated from 2D thin section derived measurements; opening up the possibility that mush permeability can be extracted as part of a general petrological workflow in any laboratory.

As in chapter 3, we emphasise that the permeability model presented here can be orders of magnitude different from existing approaches. While our model (Eq. 3) is similar in form (and based on the same starting point) as the Kozeny-Carman model given in Bachmann & Bergantz (2004), the shape-dependence of permeability that we apply renders the predictions of our model dramatically different from those of $k = {\phi_m}^3 a^2/(150(1-\phi_m)^2)$ with a fixed single crystal 'size' a. Therefore, we propose that not only does our model include the effect of crystal shape, which should be incorporated in mush permeability models, but it also gives higher permeability predictions than existing approaches. If embedded in any existing melt migration model, the higher permeabilities predicted here would result in greater fluxes and shorter overall transport timescales for a given set of conditions. Therefore, there are direct implications of our result for crustal melt movement models.

Acknowledgments

We thank Madeleine Humphreys, Martin Mangler, Alex Iveson, Amanda Lindoo, Charline Lormand, Katie Schofield, and Gemma Brown, for fascinating discussions about magma mush dynamics during 'mush meetings' at Durham University, led by Madeleine Humphreys. We thank Donald Dingwell for facilitating the contribution of J. Vasseur and for general discussion. We acknowledge funding from a Durham Doctoral Scholarship provided to E. Bretagne, and the Natural Environment Research Council Standard Grant "Magma mush eruptibility: The lifetime of mobile magma" NE/T000430/1. We acknowledge access to the OGIC XCT facility at Strathclyde which was supported by EP/T023198/1, and NE/T00908X/2.

References

Annen, C., 2009. From plutons to magma chambers: Thermal constraints on the accumulation of eruptible silicic magma in the upper crust. *Earth and Planetary Science Letters*, *284*(3-4), pp.409-416.

Bachmann, O. and Bergantz, G.W., 2004. On the origin of crystal-poor rhyolites: extracted from batholithic crystal mushes. *Journal of Petrology*, *45*(8), pp.1565-1582.

Bergantz, G.W., Schleicher, J.M. and Burgisser, A., 2017. On the kinematics and dynamics of crystal-rich systems. *Journal of Geophysical Research: Solid Earth*, *122*(8), pp.6131-6159.

Cashman, K.V., Sparks, R.S.J. and Blundy, J.D., 2017. Vertically extensive and unstable magmatic systems: a unified view of igneous processes. *Science*, *355*(6331), p. 3055.

Colombier, M., Wadsworth, F.B., Scheu, B., Vasseur, J., Dobson, K.J., Cáceres, F., Allabar, A., Marone, F., Schlepütz, C.M. and Dingwell, D.B., 2020. In situ observation of the percolation threshold in multiphase magma analogues. *Bulletin of volcanology*, *82*(4), pp.1-15.

Ergun, S., 1952. Determination of geometric surface area of crushed porous solids. *Analytical Chemistry*, *24*(2), pp.388-393.

Higgins, M.D., 1994. Numerical modeling of crystal shapes in thin sections: estimation of crystal habit and true size. *American Mineralogist*, *79*(1-2), pp.113-119.

Hildreth, W. and Wilson, C.J., 2007. Compositional zoning of the Bishop Tuff. *Journal of Petrology*, *48*(5), pp.951-999.

Holness, M.B., 2018. Melt segregation from silicic crystal mushes: a critical appraisal of possible mechanisms and their microstructural record. *Contributions to Mineralogy and Petrology*, *173*(6), pp.1-17.

Holness, M.B., Stock, M.J. and Geist, D., 2019. Magma chambers versus mush zones: constraining the architecture of sub-volcanic plumbing systems from microstructural analysis of crystalline enclaves. *Philosophical Transactions of the Royal Society A*, *377*(2139), p.20180006.

Humphreys, M.C., 2009. Chemical evolution of intercumulus liquid, as recorded in plagioclase overgrowth rims from the Skaergaard intrusion. *Journal of Petrology*, *50*(1), pp.127-145.

Jackson, M.D., Blundy, J. and Sparks, R.S.J., 2018. Chemical differentiation, cold storage and remobilization of magma in the Earth's crust. *Nature*, *564*(7736), pp.405-409.

Lewiner, T., Lopes, H., Vieira, A.W. and Tavares, G., 2003. Efficient implementation of marching cubes' cases with topological guarantees. *Journal of graphics tools*, *8*(2), pp.1-15.

Liu, B. and Lee, C.T., 2021. Fast melt expulsion from crystal-rich mushes via induced anisotropic permeability. *Earth and Planetary Science Letters*, *571*, p.117113.

Liu, B. and Lee, C.T., 2020. Large silicic eruptions, episodic recharge, and the transcrustal magmatic system. *Geochemistry, Geophysics, Geosystems*, *21*(9), p.e2020GC009220.

Liu, T., Lin, B. and Yang, W., 2017. Impact of matrix–fracture interactions on coal permeability: model development and analysis. *Fuel*, *207*, pp.522-532.

Llewellin, E.W., 2010. LBflow: An extensible lattice Boltzmann framework for the simulation of geophysical flows. Part I: theory and implementation. *Computers & Geosciences*, *36*(2), pp.115-122.

Llewellin, E.W., 2010. LBflow: An extensible lattice Boltzmann framework for the simulation of geophysical flows. Part II: usage and validation. *Computers & geosciences*, *36*(2), pp.123-132.

Lorensen, W.E. and Cline, H.E., 1987. Marching cubes: A high resolution 3D surface construction algorithm. *ACM siggraph computer graphics*, *21*(4), pp.163-169.

Mangler, M.F., Humphreys, M., Wadsworth, F.B., Iveson, A.A. and Higgins, M.D., 2022. Variation of plagioclase shape with size in intermediate magmas: a window into incipient plagioclase crystallisation. *Contributions to Mineralogy and Petrology*, *177*(6), pp.1-21.

Martys, N.S., Torquato, S. and Bentz, D.P., 1994. Universal scaling of fluid permeability for sphere packings. *Physical Review E*, *50*(1), p.403.

McKenzie, D., 1984. The generation and compaction of partially molten rock. *Journal of petrology*, *25*(3), pp.713-765.

Morse, S.A., 1998. Is the cumulate paradigm at risk?: an extended discussion of The cumulate paradigm reconsidered. *The Journal of geology*, *106*(3), pp.367-372.

Nabovati, A., Llewellin, E.W. and Sousa, A.C., 2009. A general model for the permeability of fibrous porous media based on fluid flow simulations using the lattice Boltzmann method. *Composites Part A: Applied Science and Manufacturing*, *40*(6-7), pp.860-869.

Röding, M., Ma, Z. and Torquato, S., 2020. Predicting permeability via statistical learning on higher-order microstructural information. *Scientific reports*, *10*(1), pp.1-17.

Sangani, A.S. and Acrivos, A., 1982. Slow flow through a periodic array of spheres. *International Journal of Multiphase Flow*, *8*(4), pp.343-360.

Sparks, R.S.J., Annen, C., Blundy, J.D., Cashman, K.V., Rust, A.C. and Jackson, M.D., 2019. Formation and dynamics of magma reservoirs. *Philosophical Transactions of the Royal society A*, *377*(2139), p.20180019.

Torquato, S., 2013. *Random heterogeneous materials*. Springer

Vasseur, J. and Wadsworth, F.B., 2017. Sphere models for pore geometry and fluid permeability in heterogeneous magmas. *Bulletin of Volcanology*, *79*(11), pp.1-15.

Vasseur, J. and Wadsworth, F.B., 2019. The permeability of columnar jointed lava. *Journal of Geophysical Research: Solid Earth*, *124*(11), pp.11305-11315.

Vasseur, J., Wadsworth, F.B. and Dingwell, D.B., 2020. Permeability of polydisperse magma foam. *Geology*, *48*(6), pp.536-540.

Vasseur, J., Wadsworth, F.B., Coumans, J.P. and Dingwell, D.B., 2021. Permeability of packs of polydisperse hard spheres. *Physical Review E*, *103*(6), p.062613.

Vasseur, J., Wadsworth, F.B., Bretagne, E. and Dingwell, D.B., 2022. Universal scaling for the permeability of random packs of overlapping and nonoverlapping particles. *Physical Review E*, *105*(4), p.L043301.

Wadsworth, F.B., Vasseur, J., Scheu, B., Kendrick, J.E., Lavallée, Y. and Dingwell, D.B., 2016. Universal scaling of fluid permeability during volcanic welding and sediment diagenesis. *Geology*, *44*(3), pp.219-222.

Wadsworth, F.B., Vasseur, J., Llewellin, E.W. and Dingwell, D.B., 2017. Sintering of polydisperse viscous droplets. *Physical Review E*, *95*(3), p.033114.

Wadsworth, F.B., Vasseur, J., Casas, A.S., Delmelle, P., Hess, K.U., Ayris, P.M. and Dingwell, D.B., 2021. A model for the kinetics of high-temperature reactions between polydisperse volcanic ash and SO2 gas. *American Mineralogist: Journal of Earth and Planetary Materials*, *106*(8), pp.1319-1332.

Wager, L.R., Brown, G.M. and Wadsworth, W.J., 1960. Types of igneous cumulates. *Journal of Petrology*, *1*(1), pp.73-85.

Wilson, C.J., Cooper, G.F., Chamberlain, K.J., Barker, S.J., Myers, M.L., Illsley-Kemp, F. and Farrell, J., 2021. No single model for supersized eruptions and their magma bodies. *Nature Reviews Earth & Environment*, *2*(9), pp.610-627

Table 4.1: raw data for permeability in the 3 directions, the specific surface area, shrinking factor and melt fraction

Name	Shrinking factor	Melt fraction	Specific surface area (m^{-1})	Perm X (m^2)	Perm Y (m2)	Perm Z (m2)
fudge bits	1.0000	0.3653	34390.27	1.18E-11	1.11E-11	1.54E-11
	0.5000	0.3543	55853.4600	3.0184E-12	3.9250E-12	3.6785E-12
	0.3333	0.3500	82000.7500	1.4193E-12	1.7350E-12	1.6758E-12
	0.2500	0.3543	99901.6500	9.3872E-13	1.0862E-12	1.1357E-12
	0.2000	0.3501	125451.0000	6.0228E-13	6.8012E-13	7.1371E-13
	0.1000	0.3543	212487.9000	1.9854E-13	2.1280E-13	2.4109E-13
	0.0667	0.3497	297233.2000	9.7299E-14	1.0181E-13	1.1673E-13
	0.0500	0.3533	370835.0000	6.5449E-14	6.8075E-14	7.9047E-14
sugar crystals	1.0000	0.375	59397.05	3.34E-12	3.38E-12	3.70E-12
	0.5000	0.3902	105453.3000	1.1671E-12	1.2327E-12	1.2243E-12
	0.3333	0.3834	154884.9000	5.0622E-13	5.3724E-13	5.4569E-13
	0.2500	0.3902	196884.2000	3.1874E-13	3.3788E-13	3.4613E-13
	0.2000	0.3835	242223.3000	2.0089E-13	2.1337E-13	2.1981E-13
	0.1000	0.3905	427365.3000	6.9858E-14	7.4480E-14	7.7062E-14
	0.0667	0.3834	588604.0000	3.8043E-14	3.9858E-14	4.2141E-14
	0.0500	0.3898	721765.1000	2.7677E-14	2.9428E-14	3.0704E-14

Table 4.2: The results of fitting for the coefficient C in Eq. 4.

Sample family	Best fit C	95% confidence interval	99% confidence interval
Cake topping data (n=16)	4.01	± 0.24	± 0.33
Fudge chunks only (n=8)	3.79	± 0.37	± 0.53
Sugar crystals only (n=8)	4.24	± 0.25	± 0.37
Square-ended cuboids (c.f. chapter 3; n=92)	5.83	± 0.10	± 0.14
All above data (n=108)	5.52	± 0.17	± 0.22

Chapter 5 : The permeability of an overgrown mush

Chapter preamble

This chapter is in preparation for submission in *Earth and Planetary Science Letters* with the following citation:

Bretagne, E., Wadsworth, F.B., Vasseur, J., Dobson, K. J, The permeability of a mush: quantifying the percolation of melt in an overgrown mush, *in prep*

The author contribution by the PhD candidate amounts to 60% of the content, and the manuscript draft presented here was authored solely by the PhD candidate.

Constraining the time evolution of melt flow around crystals in a magma mush is essential to better understanding crystal-melt segregation, reactive transport and differentiation at crustal scale. Most widely accepted trans-crustal mush zone evolution models are underpinned by the mobility of the interstitial melt, hence are controlled by the permeability of the mush, the ability of the static crystal framework to transmit a fluid phase. Previous models for mush permeability are only defined up to the maximum packing of cumulate crystals, but in this contribution we validate a percolation model for overgrown cumulate crystals and low melt fraction. The mush is represented here by a numerical pack of cuboids that is incrementally overgrown to simulate crystal overgrowth. We define a percolation threshold for overgrown magma mush from the permeability data which is very close to values found for overlapping sphere packs. We also define a new expression for calculating the specific surface area as a function of the melt fraction and crystal size and aspect ratio. The model is very close to expressions for overlapping sphere packs and the data for the overgrown cuboids collapse to a single value at low melt fractions, implying that the shape of the initial crystals becomes irrelevant at low melt fractions (close to the percolation threshold). Herein, we also show that accounting for the percolation threshold when looking at the permeability of porous media and mush, in particular, is very important. At low melt fractions, the difference between a model that does not account for the percolation threshold (e.g. Jackson et al., 2018) brings about errors that tend to infinity. This has major implications for melt percolation in a mush, impacting melt extraction calculations or even reactive flow pathways to mention just a few. We also discuss that correctly modelling the flow of melt

around cumulate crystals in the mush is essential for understanding the final textures that we see in the crystalline end result that we can observe in the field today.

5.1 Introduction

Transport of magmatic melts may be hosted in magma mush zones, which could extend over substantial vertical sections of the Earth's crust (Cashman et al., 2017). Percolation of melts through mush can be reactive, resulting in a distillation column effect at crustal scales, and dynamic magma evolution (Annen et al., 2006; Cashman et al., 2017; Jackson et al., 2018; Sparks et al., 2019). The progression of both melt movement, and of melt-crystal reactions are rate-limited by the percolation speed through the mush. In turn, the speed of melt percolation is controlled by the permeability of the solid framework of crystals between which melts migrate (c.f. chapter 3; Liu and Lee, 2021). Models for crystallization or compaction predict that the permeability of mush evolves with time as melt volume fraction evolves (Bachmann and Bergantz, 2004; Jackson et al., 2018), however the specifics of this relationship remain poorly constrained.

In addition to melt migration itself, magma mush permeability exerts control on the crystallization path a mush will take, and therefore the end-state mineral assemblage and texture (Humphreys, 2009). As mushes solidify – forming cumulate textures – temperature and interstitial melt composition changes and the nature of the interstitial crystallisation is sensitive to these changes. Adcumulate textures are formed when the crystallizing interstitial melt is hydraulically connected, such that it is constantly replenished and cannot evolve *in situ* (Morse, 1998). By contrast orthocumulate textures are formed when the crystallizing interstitial melt is poorly hydraulically connected, such that it is readily isolated, causing overgrowth rims on, for example, plagioclase, and the formation of evolved interstitial phases (e.g. Wager et al., 1960; Morse, 1998). This difference – adcumulate compared with orthocumulate – is therefore controlled by the evolution of the permeability, which dictates the degree of hydraulic connectivity of melt.

On the whole, magma mush permeability is approximated as an isotropic pseudo-scalar property (Bachmann and Bergantz, 2004; Jackson et al., 2018) and simple scaling laws are used. Exceptions include models that explicitly account for the development of fabric and anisotropy of permeability, however, these are typically specific to a given mush type (such as

olivine-dominated mush; Liu & Lee, 2021) and the relationship between anisotropy, strain, and crystal shape or properties are poorly known (discussed in Bergantz et al., 2017). Therefore, isotropic approximations are common, especially when embedded in 1D models of crustal-scale melt migration processes (Annen et al., 2006; Bachmann and Bergantz, 2004; Jackson et al., 2018). The scaling laws used are typically of the generalized Kozeny-Carman form

$$k = \beta a^2 \phi_m^{\alpha} \qquad \text{Eq. 1}$$

where k is the permeability, ϕ_m is the melt fraction, a is a mush crystal lengthscale, α is an exponent that is typically $\alpha = 3$ after Carman (1937), and β is then a parameter that varies from model to model. For example, Jackson et al., (2018) use $\beta = 1/125$, whereas Bachmann & Bergantz, (2004) use $\beta = [\gamma(1-\phi_m)^2]^{-1}$ with $50 \leq \gamma \leq 200$ (Rabinowicz et al., 2001)[2]. In its simplicity, Eq. 1 does not capture the effect of crystal morphology. Additionally, Eq. 1 predicts that there should be a finite permeability even down to vanishingly low melt fractions $\phi_m \to 0$ (but for $\phi_m = 0, k = 0$). This is counter to the concept of melt pocket isolation and a percolation threshold $\phi_m = \phi_c$ as crystals intergrow, overgrow, or compact. Note that in a 2-phase magma mush, $\phi_m = 1 - \phi$ where ϕ is the crystallinity.

Generalising the Kozeny-Carman law for a better shape descriptor (Torquato, 2013; Vasseur et al., 2022, 2021; Vasseur and Wadsworth, 2017), we introduced in chapter 3 a modification to the form of Eq. 1 that accounts for crystal shape by approximating crystals to cuboid solids with axis lengths a, b, and c and two aspect ratios $r_1 = c/a$ and $r_2 = b/a$

$$k = \frac{{\phi_m}^3}{Cs^2} = \frac{a^2\,\phi_m^3}{C\phi^2}\left(1 + \frac{1}{r_1} + \frac{1}{r_2}\right)^{-2} \qquad \text{Eq. 2}$$

where s is the specific surface area, and C is a constant validated to be $C \approx 5$ across a range of media (Röding et al., 2020). While Eq. 2 accounts for crystal morphology and therefore allows platey (oblate) and acicular/needle-like (prolate) crystals to be compared directly, the issue remains that this approach cannot account for isolation effects at low melt fraction as $\phi_m \to \phi_c$. For this reason, we propose in chapter 3 that Eq. 2 is only appropriate for 'loose mush' for which crystals are at or near to a random maximum packing density, but not denser. At higher

[2] In the original Bachmann & Bergantz (2004) $\beta = \left[\gamma\left(1 - {\phi_m}^2\right)\right]^{-1}$ which we assume is a typographic error and should be $\beta = [\gamma(1-\phi_m)^2]^{-1}$ reported here.

densities, or equivalently, lower melt fractions, a viable permeability law for magma mush remains to be tested.

Here, we aim to address some outstanding issues with models for mush permeability. Namely and foremost, we explore how the permeability evolves as melt fraction ϕ_m decreases to low values (i.e. the crystallinity ϕ rises beyond the maximum packing fraction, defined as $\phi = \phi'$) and aim to provide a direct constraint of the percolation threshold. To do this, we use image analysis methods to create 3D geometries where simulated crystals can be overgrown in increments, successively occluding the interstitial space. We use these new data to test models for the permeability that can be applied across a wide range of melt fraction, useful as a constitutive model in larger, crustal-scale models of mush dynamics (Jackson et al., 2018).

5.1.1. First order observations from cumulate textures

In some cases, primocrysts can be distinguished from post-emplacement phases that crystallize from an interstitial melt. This means that cumulate rocks can preserve primary evidence for crystal geometries of the mush. Here, we use micrographs of three examples from the Skaergaard system in Greenland, all published previously (Humphreys, 2009). We provide interpretive diagrams where we identify the phases that are interpreted to have been the crystal framework, and the phases that are interpreted to have been the melt phase at the time of crystallization of a loose mush (Figure). Our interpretive diagrams, associated with direct micrographs, give some information about the melt-crystal morphologies that might typify intermediate to low melt fraction examples. We can see that at low relative melt fractions, it appears that isolated pockets of melt occur between overgrown or interlocking crystals, (Figure a-5.1d). By contrast, at high relative melt fractions, the solid phase(s) touch at contact points, but are separated by regions of open melt channels, now replaced by oxides (Figure e & 5.1f). While isolated versus connected is impossible to determine reliably in 2D, this at least suggests that the hydraulic properties – such as permeability – affect the texture of the final mineral assemblage.

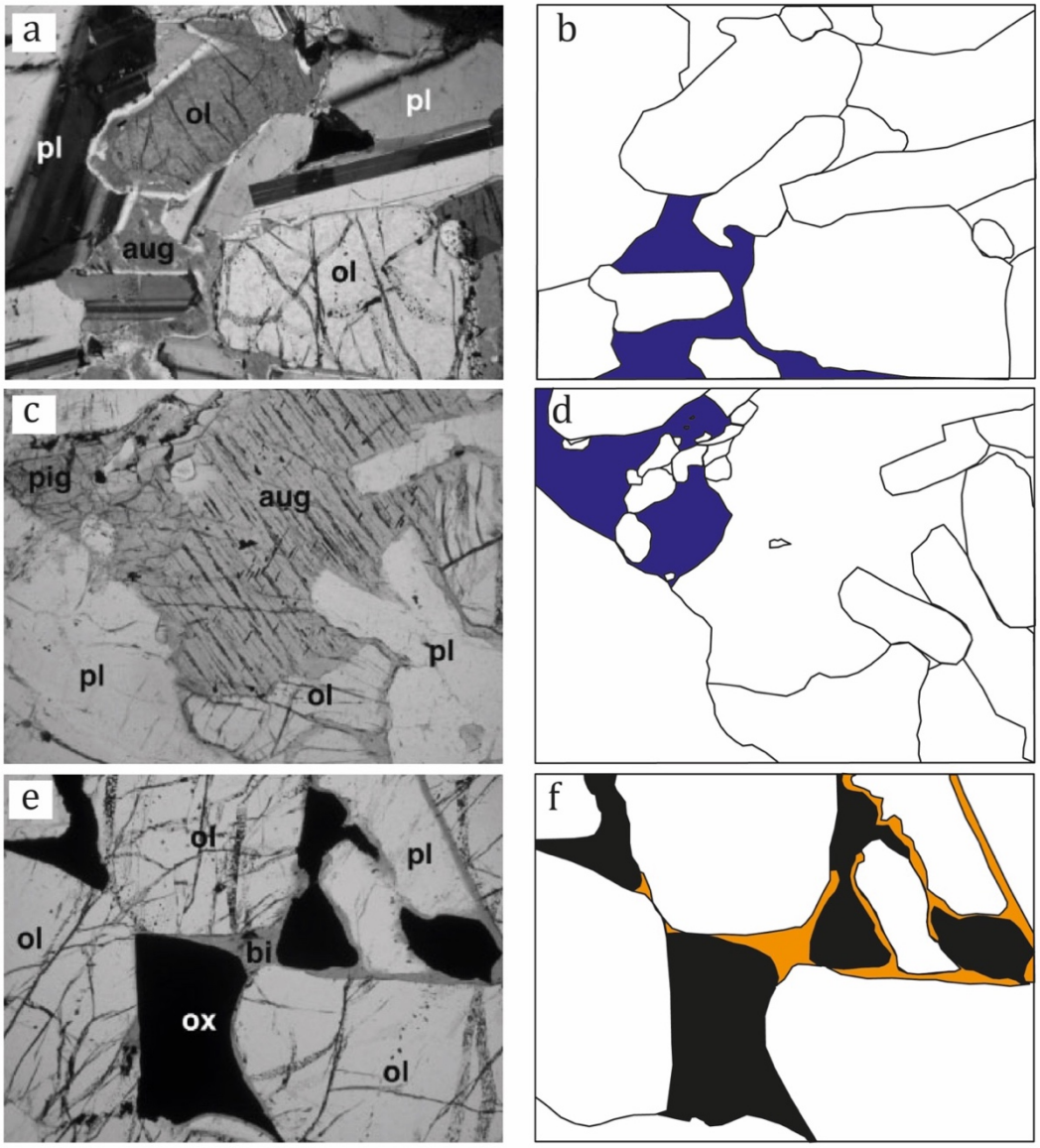

Figure 5.1: Textures of magma mush inferred from micrographs of cumulate rocks (these examples are from Skaergaard, Greenland). (a,c,e) Original micrographs reproduced with permission from Humphreys, (2009). (b,d,f) Interpretive phase portraits of the same images divided into a primocryst phase (colourless) and a melt phase , according to the petrological interpretations presented by Humphreys, (2009). (a) Cumulate plagioclase and olivine with the interstitial melt interpreted to be represented by augite (blue). (c) Cumulate augite, plagioclase, and olivine with a single pigeonite phase interpreted to represent the interstitial liquid (blue). (e) Cumulate olivine and plagioclase crystals with the interstitial melt interpreted to be represented by the oxides (black) and biotite (orange). In all images, the image horizontal length is 2-3 mm

5.1.2. Model hypothesis

The permeability model shown herein or in the general Kozeny-Carman form is only valid until maximum packing fraction of crystals $\phi = \phi'$, where all the solids in the system occupy the highest volume fraction possible by packing alone. The maximum packing fraction is a function of the aspect ratio of the solids involved (e.g. Lui et al., 2017; c.f. chapter 3). The crystallinity can rise above the maximum packing if the phases intergrow, overgrow, or if new phases nucleate in the interstitial spaces (all of these possibilities are seen in Figure). At crystallinities beyond maximum packing ϕ', we need to use percolation theory to model fluid flow and correctly predict the permeability (Martys et al., 1994; Wadsworth et al., 2016; Wadsworth et al., 2017; Wadsworth et al., 2021, Vasseur et al., 2022). A percolation model was proposed by Martys et al. (1994)

$$k = \frac{2\left(1 - \left(\phi_m - \phi_c\right)\right)}{s^2} \left(\phi_m - \phi_c\right)^y \qquad \text{Eq. 3}$$

where ϕ_c is the percolation threshold melt fraction at which melt is fully isolated, and y is an exponent. Eq. 3 predicts that at $\phi_m < \phi_c$ the system will have zero permeability, whereas at $\phi_m > \phi_c$ the permeability will be finite. As with Eq. 1, Eq. 3 suggests that the length-scale of importance here is the inverse of the specific surface area, s^{-1}, such that the permeability proportionality is $k \propto s^{-2}$. This approach has been validated for generalized digital media (Martys et al., 1994; Vasseur et al., 2022; Vasseur and Wadsworth, 2017), sandstones and volcanic deposits (Eichheimer et al., 2020; Ryan et al., 2020; Wadsworth et al., 2021, 2016), systems of bubbles growing in magma (Vasseur et al., 2020), and industrially relevant sintering systems (Wadsworth et al., 2017); but not yet for magma mush.

The so-called 'percolation exponent' y has been theoretically constrained to be $y = 4.4$ for systems of overlapping spheres (Feng et al., 1987), and similar values $4 \leq y \leq 4.4$ have been found empirically using large datasets (Martys et al., 1994; Vasseur et al., 2022; Wadsworth et al., 2016, 2021). Here, we propose to set $y = 4.4$ and not vary this further. Similarly, the percolation threshold ϕ_c has been constrained for a range of overlapping media, most pertinent here is for 'square prisms' or, equivalently, overlapping cuboids (Ballow et al. 2022). In Table 5.1, we summarize existing constraints of the percolation threshold ϕ_c, which will be compared with the value we find here. We will also compare our percolation threshold ϕ_c with values

obtained for overlapping sphere packs (Kertesz, 1981; Rintoul, 2000; Vasseur et Wadsworth, 2017).

Now that we are interested in the domain beyond the maximum packing fraction $\phi > \phi'$, the specific surface area equation (expressed in Eq. 2) is no longer valid as the cuboids are no longer defined by their contact point but become progressively overgrown and/or intergrown. The specific area can no longer simply be a function of crystal size a and aspect ratios $r_1$and r_2. In this contribution, we aim to present a new expression for the specific surface area for overgrown cuboids, derived from the permeability data.

The percolation model is typically normalised by the reference permeability k_r (Wadsworth et al. 2017; Vasseur & Wadsworth, 2017; Vasseur et al. 2022)

$$k_r = \frac{2\left(1-\left(\phi_m-\phi_c\right)\right)}{s^2}. \quad \text{Eq. 4}$$

The normalised percolation model then becomes $\bar{k} = k/k_r = (\phi_m - \phi_c)^y$.

Table 5.1: Percolation thresholds for the melt between overlapping 3D objects

System	ϕ_c	Reference
Overlapping square-ended cuboids*		
$r_1 = 20$	0.0534 ± 0.0004	Ballow et al. (2022)
$r_1 = 15$	0.0535 ± 0.0004	Ballow et al. (2022)
$r_1 = 10$	0.0524 ± 0.0005	Ballow et al. (2022)
$r_1 = 8$	0.0523 ± 0.0006	Ballow et al. (2022)
$r_1 = 7$	0.0519 ± 0.0003	Ballow et al. (2022)
$r_1 = 6$	0.0519 ± 0.0005	Ballow et al. (2022)
$r_1 = 5$	0.0515 ± 0.0007	Ballow et al. (2022)
$r_1 = 4$	0.0505 ± 0.0007	Ballow et al. (2022)
$r_1 = 3$	0.0485 ± 0.0011	Ballow et al. (2022)
$r_1 = 2.5$	0.0483 ± 0.0008	Ballow et al. (2022)
$r_1 = 2$	0.0465 ± 0.0007	Ballow et al. (2022)
$r_1 = 1.5$	0.0461 ± 0.0014	Ballow et al. (2022)
$r_1 = 1$	0.0449 ± 0.0005	Ballow et al. (2022)
Overlapping spheres		
	0.034 ± 0.007	Kertesz (1981)
	0.032 ± 0.004	Elam et al. (1984)

*r_1 is the aspect ratio of a square ended cuboid (i.e. $r_2 = 1$ is a cube).

5.2 Methods and materials

To test the predictions of the percolation model for cuboids, we simulate crystal overgrowth. The initial geometries are numerical periodic domains of packed and randomly oriented solid cuboids generated by Liu et al. (2017), analysed in chapter 3. The initial cuboids have a square cross-section, such that $a = b$, and the domains are produced at their random maximum packing (i.e. $\phi = \phi'$). The domains are characterised by the aspect ratio of the cuboids, r_1 (where $r_2 = 1$).

We numerically erode the pore spaces by a set increment using Avizo©. To achieve this, 1 solid phase voxel is added adjacent to existing solid phases subject to 3 conditions: (1) a voxel is added orthogonally to the pore voxels adjacent to each existing solid voxel face that borders a pore voxel; (2) a voxel is added to each edge; (3) a voxel is added to each corner. This is the same method that was applied by Macente et al. (2022) to simulate the precipitation of layers on pore walls. We repeat this incrementally in 1-voxel steps up to 20 times (for more details on the methodology in Avizo©, see Chapter 2). This workflow is then applied to initial cuboid packs with different aspect ratios.

In Figure 5.4, we show selected steps of the pore erosion process and highlight the evolution of the melt fraction connectivity. Our 3D datasets allow us to extract the melt fraction that is fully connected in a given direction, which we term the percolating melt fraction ϕ_p, as opposed to the total melt fraction ϕ_m. The ratio of these two ϕ_p/ϕ_m is a 'connectivity' (c.f. Colombier et al., 2017). In detail, we extract ϕ_p in all three principal directions x, y, and z and then average them. In Figure 5.4a, the melt phase is completely connected ($\phi_p/\phi_m = 1$), expressed by the purple colour of the melt phase. As the space for the melt shrinks (Figure 5.4b-5.2d), the melt fraction becomes less and less connected until in the result of the 20th growth iteration, the melt only exists as isolated pockets in the mush (Figure 5.4d).

It is important here to note that the overgrowth on the crystals is performed on the crystal phase as a whole instead of each individual crystal. In practice, this means that the crystal-melt interface is grown outwards towards the melt phase by one voxel in every direction, on all 6 sides of the voxel as well as on the ridges. This is why we call grown domains overgrown as opposed to intergrown, and we think is more representative of how magma mush evolves beyond an initial packed state (cf. Figure e & Figure f).

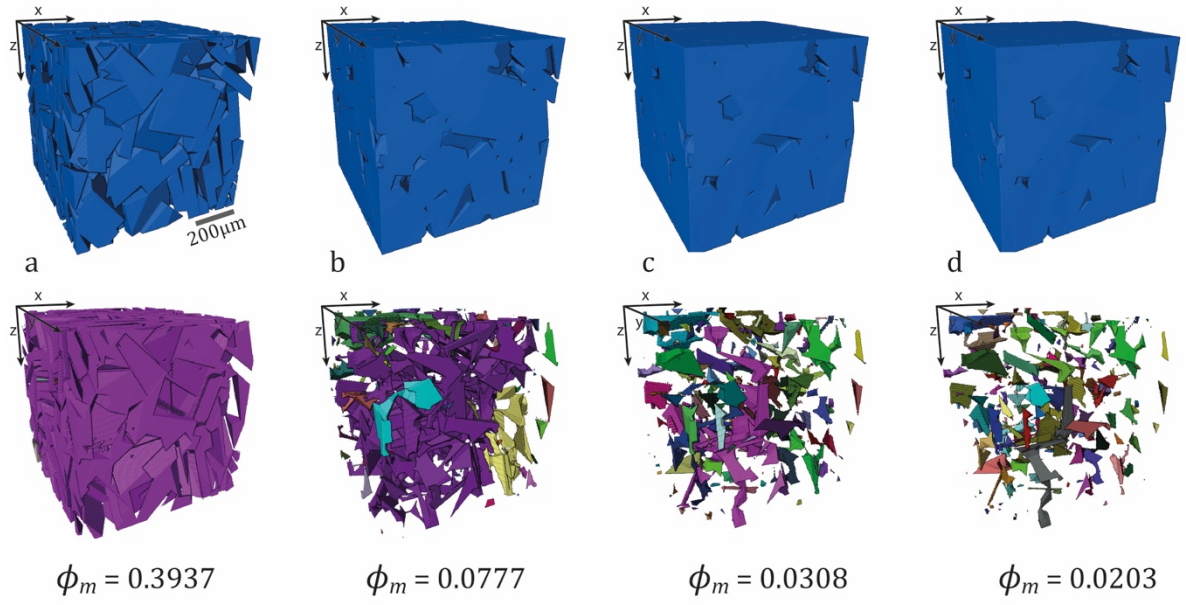

Figure 5.4: Coupled volumetric representation of the crystal fraction (top) and the melt fraction (bottom) at select growth steps for the domain $r_1 = 0.2$. The melt fraction ϕ_m indicated for each step. The connectivity of the melt fraction is qualitatively expressed through the colour of the melt phase: the connected parts are in purple, and as the crystals are grown, the pore throats are pinched off and the remaining melt trapped in the isolated pockets is expressed in a different colour (c.f. (b) to (d)).

We obtain the specific surface area of each incremental growth step of each cuboid pack using a marching cubes algorithm that computes the volume ratio of the crystal and the melt phases (Lorensen & Cline 1987). We use an implementation of this algorithm developed in Wadsworth et al. (2017) and Vasseur & Wadsworth (2017). We then use LBflow – a numerical lattice-Boltzmann fluid flow simulation tool (Llewellin, 2010a, 2010b) – to characterise steady-state fluid flow through the inter-cuboid space in all three directions x, y and z (details of the numerical analysis are provided in Chapter 2). The velocity field is averaged in each direction and the averaged velocity value is used in Darcy's law to output the permeability of each domain. The difference between the directional permeability values is evaluated and if small, we declare the permeability isotropic.

5.3 Results

In this contribution, we aim to give a permeability model such as Eq. 2 where the specific area is included in the model. This is achieved in several steps of data analysis: (1) we constrain the percolation threshold ϕ_c using the permeability data measured from the simulations; (2) we

then test the validity of the percolation model (Eq. 3) for overgrown cuboids and propose a universal model for permeability across all melt fraction $\phi_c \lesssim \phi_m \lesssim 1$; and lastly (3) we propose a new model for the specific surface area of overgrown cuboids, for cases where the user does not have a measured value.

5.3.1. Permeability of magma mush at low melt fraction

The first step in the analysis of our results is to test Eq. 3 as a function of the melt fraction, $k(\phi_m)$. Our datasets for each domain include data for the melt fraction ϕ_m, the permeability of the domain k, and the specific surface area s. In order to apply Eq. 3 directly, we must also find the percolation threshold ϕ_c. There exist two levels of analysis here: firstly, we can assume that the percolation threshold ϕ_c is a single value for all domains, regardless of the aspect ratio of the initial pack of cuboids: secondly, we can check the validity of the first statement by comparing values of the percolation threshold ϕ_c for each aspect ratio. We achieve this by using a least squares regression between the measured permeability data and the predicted permeability values using Eq. 3 to minimize for a best-fit ϕ_c for all domains. Assuming a percolation threshold for all aspect ratios, we find that $\phi_c = 0.0187 \pm 0.001$. Importantly, we do not find a significantly difference for percolation threshold data per aspect ratio: for overgrown cube packs (i.e. $r_1 = 1$), we find $\phi_c = 0.0225 \pm 0.005$ and for overgrown prolate or oblate packs, we find that $\phi_c = 0.229 \pm 0.003$ and 0.0224 ± 0.004, respectively. This demonstrates that the initial pack type has no influence on the percolation threshold ϕ_c during an overgrowth process and suggests that there may be a universal value regardless of mush type (c.f. Table 5.2).

Assuming the percolation threshold $\phi_c = 0.0187 \pm 0.001$ for all aspect ratios, we check the fit of the percolation with the permeability data of the overgrown cuboid packs in the dimensionless space (Fig. 5.3, using Eq. 4). Visual inspection of the fit between the model and the data confirms that (1) the percolation model is a good description of the permeability data, and (2) the value of the percolation threshold ϕ_c may indeed be universal to these data regardless of mush type.

Table 5.2: results of least squares regression for individual aspect ratios and all the data together.

r_1	ϕ_c	95% confidence interval	99% confidence interval

0.2 (n=8)	0.0224	± 0.0040	± 0.0057
0.7 (n=7)	0.0144	± 0.0016	± 0.0024
1 (n=6)	0.0225	± 0.0047	± 0.0072
1.5 (n=7)	0.0196	± 0.0024	± 0.0035
3 (n=10)	0.0174	± 0.0008	± 0.0012
4 (n=8)	0.0204	± 0.0027	± 0.0039
6 (n=8)	0.0229	± 0.0031	± 0.0044
all data (n=54)	0.0187	± 0.0010	± 0.0013

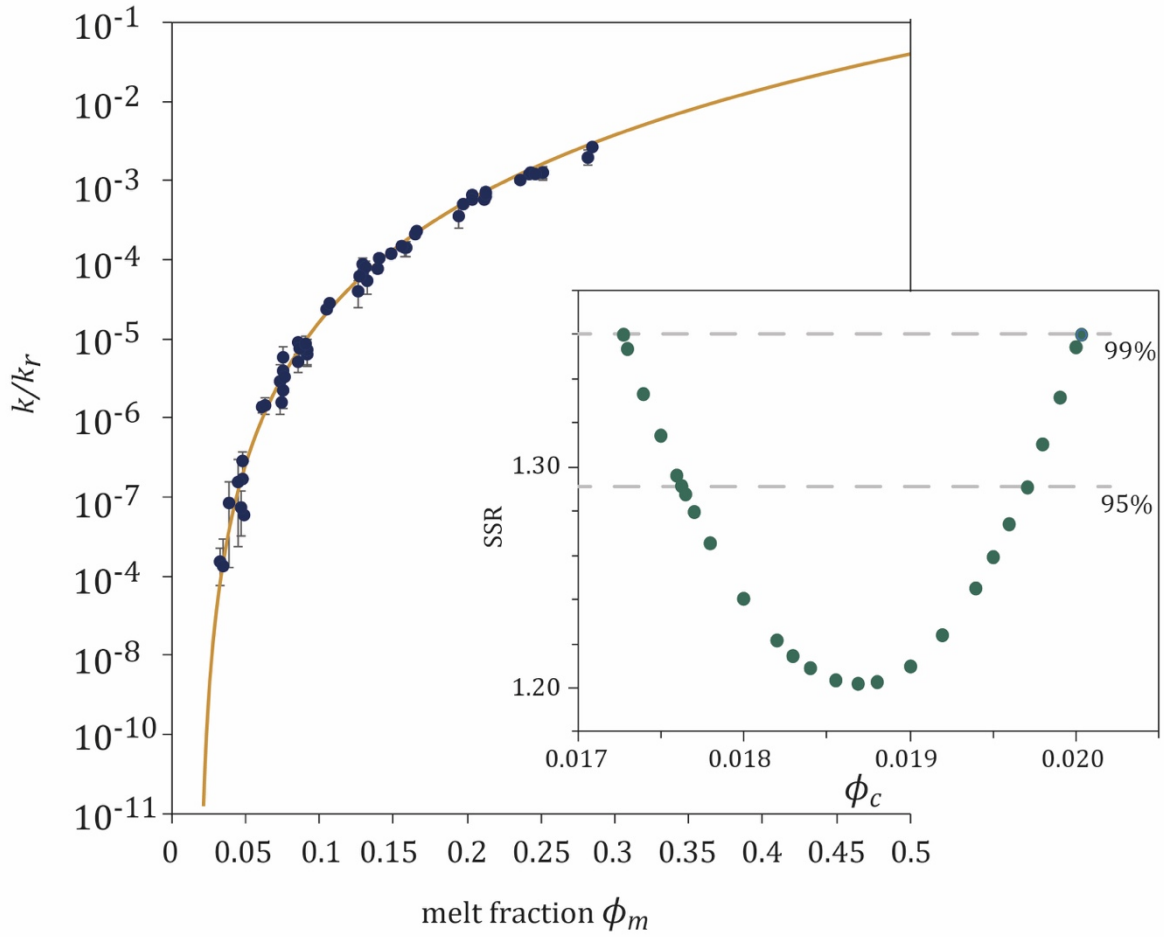

Figure 5.3. Normalised permeability data plotted against the melt fraction (blue round symbols), the percolation model (yellow line, Eq. 3) is added for visual inspection of the fit of the percolation threshold ($\phi_c = 0.0187$). The data and the model are normalised using k_r (Eq. 4). The inset represents the confidence intervals of the least squares regression used to obtain the best fit percolation threshold value for all aspect ratios (last line of Table 5.2). The sum of squared residuals (SSR) is on the x-axis and the percolation threshold data is on the y-axis. The 99 and 95 % confidence intervals are shown, giving the error on the fitted percolation threshold value (local minima).

5.3.2. Direct determination of the percolation threshold

By looking at the evolution of the connectivity ϕ_p/ϕ_m as a function of the melt fraction ϕ_m, we can track what proportion of the melt phase is connected during the simulated overgrowth process. We find that at the initial maximum packing value ϕ', the connectivity $\phi_p/\phi_m = 1$, which means that all the melt phase is connected (Fig. 5.4). Conversely, as the melt fraction nears zero $\phi_m \to 0$,the connectivity ϕ_p/ϕ_m drops to zero. There is an apparent transition window in which the connectivity is other than null or 1, $0 < \phi_p/\phi_m < 1$, which qualitatively occurs around $0.02 \lesssim \phi_c \lesssim 0.05$ (Fig. 5.4).

In a simple system or in an infinitely large system, the connectivity transition from $0 < \phi_p/\phi_m < 1$ would be a step function and the percolation threshold ϕ_c would appear as a single value at which ϕ_p/ϕ_m drops to zero. However, the overgrown cuboid domains have a finite size and the transition in connectivity is smoothed out over the melt fraction ϕ_m. In Fig. 5.4, we also plot the best-fit percolation threshold value $\phi_c = 0.0187$. as well as the value for intergrown cuboids obtained from the literature (Ballow et al., 2022). Qualitatively, the best-fit percolation threshold ϕ_c occurs at the lowest end of the window $0 < \phi_p/\phi_m < 1$, such that it demarks well the melt fraction ϕ_m for which all pores become isolated. Based on this observation, we consider this an independent confirmation that our best-fit value is robust using the connectivity.

In comparison to our best-fit percolation threshold value that is insensitive to aspect ratio, Ballow et al. (2022) provide values for square-edged cuboids that are sensitive to aspect ratio r_1 (Table) and show an increasing trend for increasing aspect ratio r_1. The trend plateaus around $r_1 \approx 5$ and remains similar up to very high aspect ratios. The percolation threshold ϕ_c for smallest aspect ratio studied in Ballow et al. (2022) (($r_1 = 1$; cubes) is $\phi_c = 0.0449 \pm 0.0005$, which is 0.0262 larger than the best-fit value found herein. And for higher r_1, this difference grows. This difference between the percolation threshold values can be explained by the fact that Ballow et al (2022) use inter-penetrable cuboids whereas we overgrow the cuboids as one packed phase. In principle, this would represent the difference between a percolation threshold for a purely intergrown mush (i.e. using the method of Ballow et al. 2022) and that of an overgrown mush (using our method).

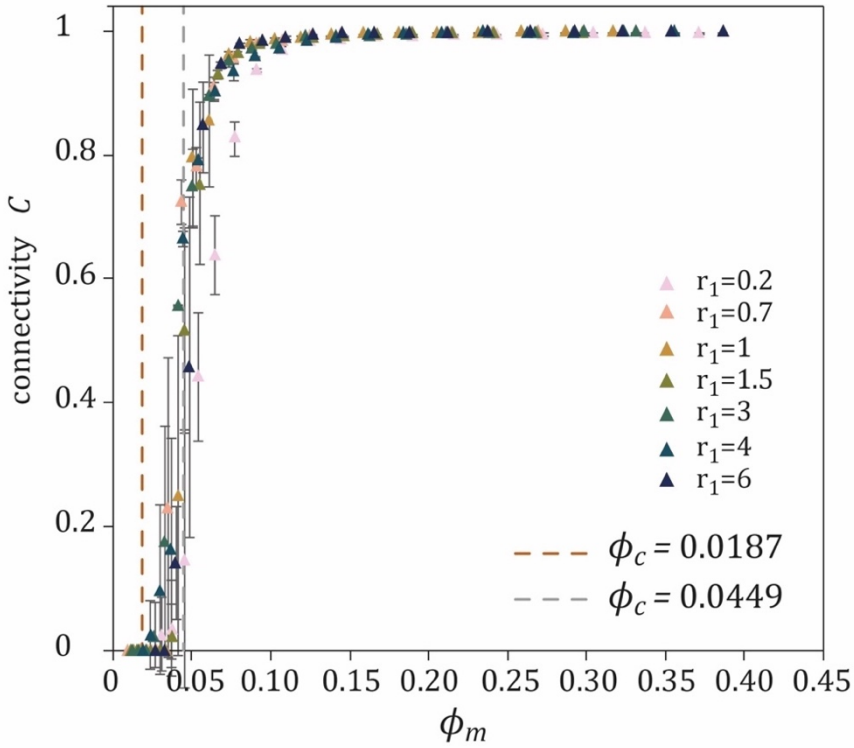

Figure 5.4. Melt phase connectivity as a function of melt fraction ϕ_m for all domains analysed. We additionally show the percolation threshold determined herein by the best fit analysis ($\phi_c = 0.0187$) and the range of percolation thresholds determined for overlapping or inter-penetrable cuboids by intergrowth ($\phi_c = 0.0449$, Ballow et al. 2022; Table 5.1).

5.3.3. Universality in models for the permeability of packed particles

In order to build a universal dimensionless picture of mush permeability, we can generalize the result shown in Fig. 5.3 beyond just the overgrown cuboid data. To do this, we first make the transformation of the x-axis data from melt fraction ϕ_m to the so-called 'reduced' melt fraction $\phi_m - \phi_c$ (after Martys et al. 1994; Wadsworth et al. 2016; Vasseur & Wadsworth 2017). Because our universal dimensionless model is $\bar{k} = (\phi_m - \phi_c)^y$, this transformation to $\phi_m - \phi_c$ as the independent variable makes the model of the form $\bar{k} = x^y$ where x is the x-axis variable. This means that in a log-log plot (Fig. 5.5b), Eq. 3 is a straight curve of slope y. This transformation is robust because we have independently verified the percolation threshold ϕ_c using the connected porosity data (Fig. 5.4). When performed to both the percolation data and to the model, the transformed data are in very good agreement across all melt fraction ϕ_m (Fig. 5.5).

In Fig. 5.5, we add the permeability data for the non-overgrown cuboids from chapter 3, which are effectively the starting point for this study – i.e. they represent maximally packed cuboid domains with no overgrowth. Additionally, we add data for non-penetrating packed spheres

that span porosities from their maximum packing up to the dilute limit (n.b. here porosity is equivalent to melt fraction ϕ_m; Vasseur et al. 2021; 2022). It is important to note that these sphere data at the dilute limit are not applicable to nature because the spheres are held artificially static, effectively in suspension in a fluid medium but without any of the dynamics that suspensions imply. Nevertheless, they represent a dilute extension of the packed porous media studied here. For both the packed-to-dilute spheres and the packed cuboids, we assume a percolation threshold $\phi_c = 0$ in the normalization via Eq. 4 and similarly the x-axis ordinate remains the melt fraction ϕ_m (i.e. without the correction on ϕ_c). This is justified because there is no geometrical reason that packed solids have a percolation threshold at any melt fraction ϕ_m (after Vasseur et al. 2021). In this case of a null percolation threshold $\phi_c = 0$, the reference permeability becomes $k_r = 2(1-\phi_m)/s^2$ for those data, which is termed a 'dilute Stokes permeability' (Torquato 2013).

As with the data novel to this contribution (i.e. overgrown cuboids), we find that across all sphere sizes, cuboid sizes, cuboid aspect ratios, and melt fractions ϕ_m, the data collapse to a universal trend (Fig. 5.5a). This universal data collapse follows the percolation model (i.e. the dimensionless form of Eq. 3) up to $\phi_m \lesssim 0.3$, and deviate at values above this limit. The deviation is from the percolation model onto a previously explored 'granular' model for dilute systems of particles that is based on an exact solution for $\phi_m \to 1$ (from Sangani & Acrivos, 1982). Interestingly, a model of the form given by Eq. 1 (with $\beta = C^{-1}\phi^{-2}$ c.f. chapter 3) has validity at this intermediate melt fraction around maximum packing values of ϕ_m~0.3. Therefore, this dimensionless approach yields these equation predictions and associated validity:

$$k = k_r \left(\sum_{i=0}^{30} c_i \left(\frac{\phi}{1-\phi'} \right)^{\frac{i}{3}} \right)^{-1} \qquad \phi_m \gtrsim 0.4 \qquad \text{Eq. 5a}$$

$$k = \frac{{\phi_m}^3}{Cs^2} \qquad 0.2 \lesssim \phi_m \lesssim 0.4 \qquad \text{Eq. 5b}$$

$$k = k_r(\phi_m - \phi_c)^y \qquad \phi_m \lesssim 0.2 \qquad \text{Eq. 5c}$$

where in Eq. 5a, the percolation threshold is null $\phi_c = 0$ in the reference permeability k_r and ϕ' is the maximum crystal volume fraction at the random close packing (as discussed in chapter 3). Eq. 5a was first proposed for cubic arrays of spheres by Sangani & Acrivos (1982) and was subsequently shown to be a reasonable predictor of the permeability between random arrays of spheres in the dilute limit (Wadsworth et al. 2017; Vasseur & Wadsworth 2017; Vasseur et al. 2021). Eq. 5b is explored in detail in Chapters 3 & 4 of this work.

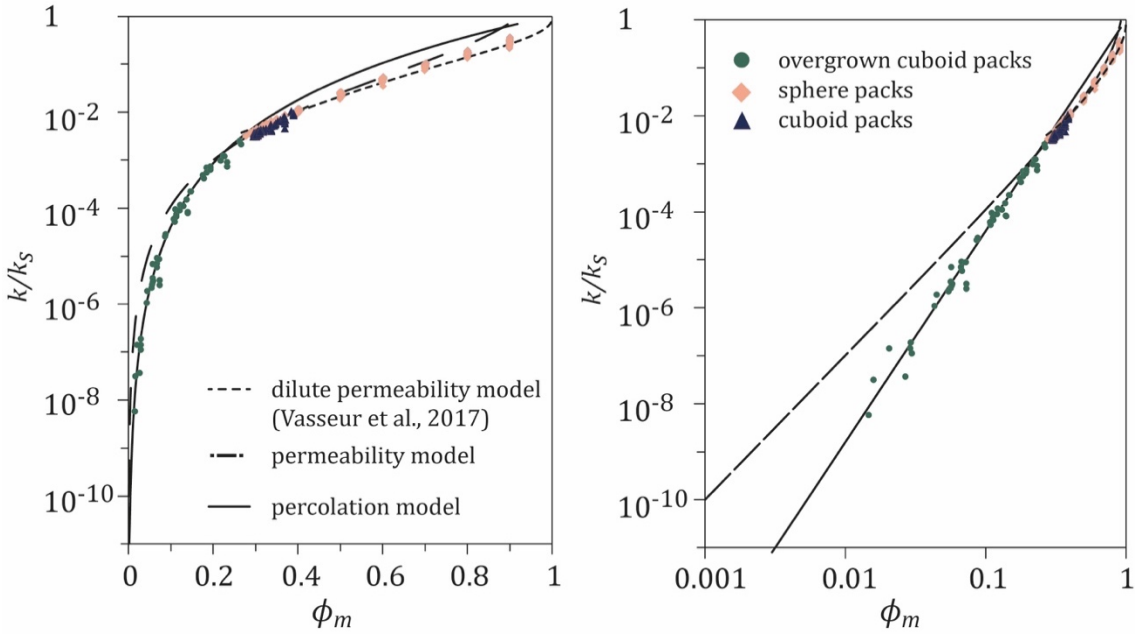

Figure 5.5: Application of the three different scaling laws over the entire range of melt fraction (Eq. 5). These scaling laws include the law applied for low melt fraction (Eq. 3 and Eq.5c) as well as the law for dilute arrays of particles (Eq. 5a) and for intermediate maximally packed systems of particles (Eq. 5b). (a) The full scaling solutions proposed herein, shown here in dimensionless space, and with the overgrown cuboids, the cuboids and dilute sphere packs data. The different data sets span the aspect ratio range as well as the melt fraction range; b) The same set of scaling laws as in part a), both axes are set to logarithmic scale to highlight the correlation between the data and the models.

5.3.4. Specific surface area model for overgrown cuboids

It is clear from Eq. 5 and its universal application in Fig. 5.5, that in all regimes (i.e. dilute, intermediate, and densely overgrown), it is the specific surface area that controls fluid flow in isotropic media. The success of the result illustrated in Fig. 5.5 requires *a priori* knowledge of the specific surface area s, which herein is a parameter we measure directly. However, in general, the specific surface area s may not be known for a given magma mush. And so, it is important to explore models for this value as a function of crystal shape and melt fraction ϕ_m

The specific surface area s is ideally measured or if that is not possible, it can be constrained but some knowledge of the shape and size of the solids is necessary in this case. Natural shapes can be approximated to spheres (e.g. Bachmann and Bergantz, 2004, 2008; Jackson et al., 2018) but herein we propose that natural crystal shapes are better represented by cuboids (c.f. chapter 3). The specific surface area for cuboids at a given melt fraction ϕ_m is given by (c.f. chapter 3)

$$s = \frac{2(1-\phi_m)}{a}\left(1+\frac{1}{r_1}+\frac{1}{r_2}\right) \qquad \text{Eq. 6}$$

where the specific surface area s is defined by crystal size a, and aspect ratios r_1 and r_2. Cuboid shapes are characterised by their three independent orthogonal axes that define shape and size a, b, and c. This expression is valid for cuboids in suspension at low packing fractions $\phi \to 0$ (hence high melt fractions) and up to the maximum packing fraction $\phi = \phi'$ (irrespective r_1 and r_2). The specific surface area calculated from the incremental growth steps of overgrown cuboid domains are used to constrain a new expression for s beyond the maximum packing $\phi = \phi'$.

We draw inspiration from the specific surface area equation for overlapping spheres $s = -3\,\phi \ln(\phi)/\delta$, where $\delta = R$ for a monodisperse size distribution and $\delta = \langle R^3\rangle/\langle R^2\rangle$ for a polydisperse size distribution, where $\langle R^n\rangle$ is the nth moment of $f(R)$ (Vasseur et al., 2022).

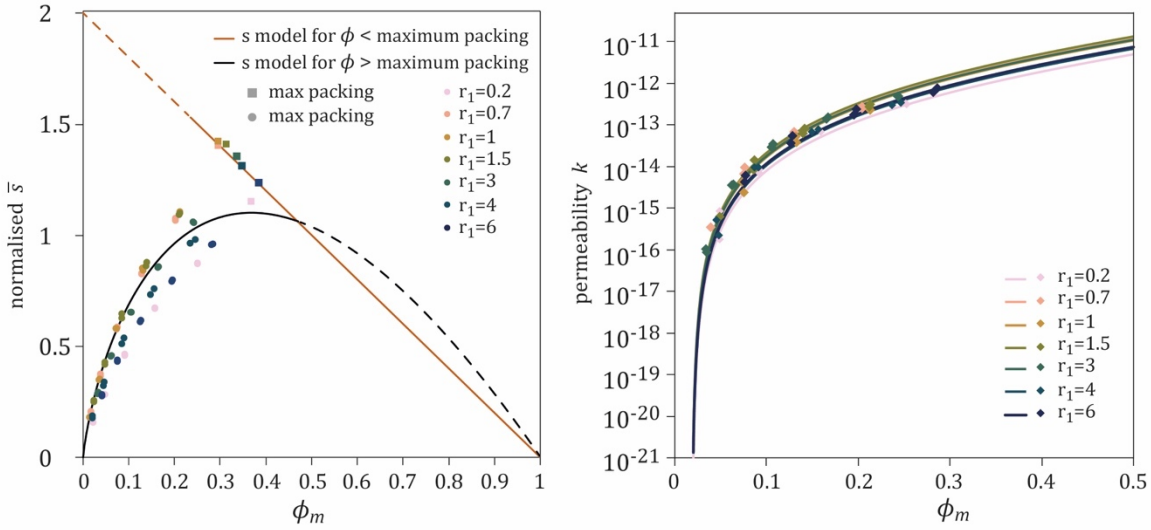

Figure 5.6: Analysis of the specific area data at each growth step and the associated permeability data, compared to theoretical models proposed herein. a) the scaled specific area data as a function of the melt fraction, compared to the s models (1) for melt fractions up to maximum packing fraction of the cuboids and (2) for melt fractions below the max. cuboid density. The maximum packing data are also shown for reference; b) sensitivity test of the s model for overgrown cuboids tested on the permeability, over the aspect ratio range. The measured permeability data are added for comparison.

Our specific surface area s data are normalised to $\bar{s} = s/s_r$, using a reference specific surface area $s_r = a/(1 + r_1^{-1} + r_2^{-1})$, a necessary step to ensure the data are expressed only as a function of the melt fraction ϕ_m. The normalised data are plotted in Fig. 5.6a and are compared to the following model for overgrown cuboids:

$$\bar{s} = \frac{s}{s_r} = -3\phi \ln(\phi) \qquad \text{Eq. 7}$$

This gives us a model for the specific surface area s, such that:

$$s = -\frac{3\,\phi \ln(\phi)}{a}\left(1 + \frac{1}{r_1} + \frac{1}{r_2}\right) \qquad \text{Eq. 8}$$

As we can see in Fig. 5.6a, the specific surface area model has a good fit for the s data at low melt fractions $\phi \to \phi'$ and the data fan away from the model towards maximum packing fraction $\phi \to \phi'$. The observed deviation from the model does not have a big impact on the permeability calculations (Figure .6b). The residuals between the modelled permeability data and the measured data remain low (<0.25 orders of magnitude) and are the highest for low melt fractions, around $\phi_m \approx \phi_c$.

We note two important observations about the specific surface area: (1) around the percolation threshold $\phi_m \to \phi_c$, the specific surface area data collapses to one value, so that the aspect ratios $r_1$and r_2 become irrelevant; and (2) the specific surface area model for overgrown cuboids is very similar to the model for overlapping spheres. These two points imply that the shape of overgrown mush becomes less and less important as the melt fraction nears the percolation threshold $\phi_m \to \phi_c$, and the initial shape of overgrown crystals can be approximated to spheres with little impact on the resulting permeability.

5.4 Discussion and implications

The similarities between the specific surface area analytical solution for overgrown cuboids (validated herein, Eq. 8) and the solution for overlapping spheres are striking and the collapse of the data to a single trend for low melt fractions $\phi_m \to \phi_c$ implies that, for low melt fractions ϕ_m, the initial shape of the crystals becomes irrelevant. This effect can be explained by the way the cuboids are overgrown in the incremental growth process: the addition of a voxel on each face, edge and corner of the initial geometry means that narrow spaces are filled up faster than the rest of the surface area. We see the same process in the natural samples (Figure e &

Figure f) where biotite fills in the narrower points of contact of the cumulate crystals, making the melt pockets rounder, hence the smaller percolation threshold than observed in the literature for intergrown cuboid simulations (Ballow et al., 2022). This implies that the overgrowth of cumulate crystal in this manner keeps the pore network open longer, i.e. beyond percolation threshold ϕ_c values predicted in the literature and enables melt percolation at late stages of mush crystallisation.

In this chapter, we verify the percolation part of our universal permeability model (Eq. 5) using flow simulations on incrementally overgrown cuboid packs, which are analogous to successive overgrowth steps on cumulate crystals. However, compared to crystal growth mechanisms, the numerical analogue we use herein are very simplified, and, in nature, this is not the only way that crystal fraction increases in a mush (e.g. Wager et al., 1960). In the literature, adcumulates and orthocumulates textures are presented as idealised end members of cumulus crystallisation but geochemical mapping of less diffuse elements, in plagioclase for example, show that crystal growth are likely to transition back and forth on a sliding scale between the two behaviours at the end of the spectrum (Humphreys, 2009). However, despite this oversimplification of natural crystal growth, the scaling law for percolation is validated for all geometries, hence, the way the cumulates grow will have little impact on the permeability predictions as long as the percolation threshold is known.

Suggested models of crustal growth by successive emplacement of sills (e.g. Annen et al., 2006; Karakas et al., 2017; Jackson et al., 2018) hinge on the mass transport of melt at crustal scale, relying on the permeability of the mush reservoir. The feasibility of this is tested herein, and accounts for the presence of a finite permeability of a mush at low melt fractions (i.e. $\phi_m \neq 1$), which Jackson et al. (2018) do not in their suggested melt percolation model.

We map the melt fraction ϕ_m dependant evolution of the permeability of a natural crystal mush using measured plagioclase crystal size data from natural samples (Fig. 5.7a). The plagioclase shapes were measured *in situ* by Duchêne et al. (2008) and have average shapes of $a:b:c = 1:6.5:9.6$. We assume a percolation threshold of $\phi_c = 0.035$, a similar value to values for packs of overlapping spheres (c.f. Table). As discussed above, the choice of percolation threshold is important but here we do not have the connectivity data to constrain an analytical ϕ_c and so, choose a theoretical ϕ_c value similar to sphere packs.

The transition from the percolation model (Eq. 5c) to the permeability model (Eq. 5b) is smooth and occurs around melt fractions of $\phi_m \approx 0.2$ (Figure a). The analytical transition point is hard to pinpoint exactly as the maximum packing density ϕ' depends on the aspect ratios and we do not have an existing model for maximum packing density of cuboids where $r_2 \neq 1$. Below the maximum packing ϕ', we observe the same data collapse toward $k \to 0$ at the percolation threshold ϕ_c. We compare the permeability models from Eq. 5 with a model that does not account for the isolated melt pockets (e.g Jackson et al., 2018).

We identify 3 stages of difference between the percolation model (Eq. 5) and the Jackson model: (1) for $\phi < \phi'$(i.e. high melt fraction ϕ_m), the Jackson et al. (2018) model underestimates the permeability of a mush and the two models diverge significantly where Jackson's plateaus out horizontally as opposed to the upward trend of Eq. 5 in the dilute domain $\phi_m \to 1$; in stage (2), defined as the area between the transition from Eq. 5b to 5c and the intersection of the Jackson et al. (2018) model and the model herein, we see that the Jackson model still underestimates the permeability but exists within an order of magnitude of our permeability model. The intersection of the two models occurs at different melt fraction ϕ_m, as the Duchêne et al. (2008) data is spread out as a function of the crystal shape. There are two notable intersection point, however, where the Jackson et al. (2018) model intersects the "low-bound" of the permeability data spread, and the "upper-bound" (highlighted by little stars in Fig. 5.7a). This is best shown in Fig. 5.7, which expresses the difference of the two models applied only to the "upper" and "lower" bound data. Stage (3) is defined as beyond the intersection until the melt fraction reaches the percolation threshold $\phi_m \to \phi_c$. In this last stage, the Jackson model overestimates the permeability and as Eq. 5 drops to the percolation threshold ϕ_c, the difference between the two models increases exponentially as shown by the difference of the two models in Figure b).

The isolated melt pockets in an overgrown mush, i.e the percolation threshold, may represent only 2% of the total volume of the mush, yet neglecting those isolated melt pockets can lead to very large errors in calculations. This is exhibited well in Fig. 5.7b where the difference with the Jackson et al. (2018) model tends to infinity because they do not account for the percolation threshold. This is all the more important because most natural mushes exist within that domain of low to very low melt fraction (e.g. Cashman et al., 2017; Huang et al., 2015; Paulatto et al., 2012; Cooper and Kent, 2014).

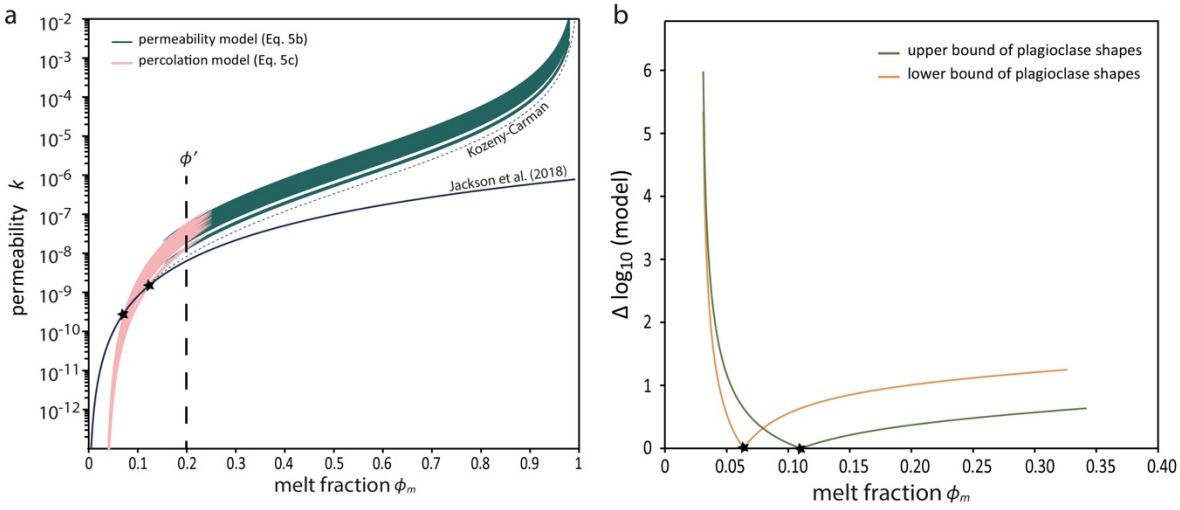

Figure 5.7: a) mapping the permeability for natural plagioclase shapes across all melt fraction using the percolation model until maximum packing fraction, the, transition to the permeability model. The plagioclase shape data is from Duchêne et al. (2008). b) The absolute value of the difference between the percolation model and the Jackson et al. (2018) model is shown as a function of the melt fraction. The difference shown here is log-based and is shows the "upper" and "lower" bounds of the permeability data obtained from the natural plagioclase shapes.

5.5 Conclusions

Constraining the time evolution of melt flow around crystals in a magma mush is essential to better understanding crystal-melt segregation, reactive transport and differentiation at crustal scale. In this contribution, we validate the percolation model by simulating fluid flow in numerical domains of overgrown cuboids, here representing a high crystalline mush. We use the permeability data to constrain the percolation threshold and subsequently propose a new analytical solution of the specific surface area for overgrown cuboids. We show that the isolated melt pockets, formed as the crystal packing of the mush increases, need to be accounted for to properly constrain the flow properties mushes. Without this, calculating the permeability at low melt fractions incurs large errors. Collating existing permeability data with the data in this contribution, we propose a universal permeability model for all melt fractions and that is valid for all crystal shapes. The implications for melt percolation in mushes for any melt fraction are important for large scale mush dynamics such as melt-crystal segregation and reactive flow that entrains crustal scale chemical differentiation. We propose a link with mush final crystalline textures, often the only field evidence left of these large-scale dynamics.

References

Annen, C., Blundy, J.D. and Sparks, R.S.J., 2006. The genesis of intermediate and silicic magmas in deep crustal hot zones. *Journal of Petrology*, *47*(3), pp.505-539.

Bachmann, O. and Bergantz, G.W., 2004. On the origin of crystal-poor rhyolites: extracted from batholithic crystal mushes. *Journal of Petrology*, *45*(8), pp.1565-1582.

Bachmann, O. and Bergantz, G.W., 2008. Rhyolites and their source mushes across tectonic settings. *Journal of Petrology*, *49*(12), pp.2277-2285.

Ballow, A., Linton, P. and Priour Jr, D.J., 2022. Percolation through Voids around Toroidal Inclusions. *arXiv preprint arXiv:2208.10582*.

Bergantz, G.W., Schleicher, J.M. and Burgisser, A., 2017. On the kinematics and dynamics of crystal-rich systems. *Journal of Geophysical Research: Solid Earth*, *122*(8), pp.6131-6159.

Carman, P.C., 1937. Fluid flow through granular beds. *Trans. Inst. Chem. Eng.*, *15*, pp.150-166.

Cashman, K.V., Sparks, R.S.J. and Blundy, J.D., 2017. Vertically extensive and unstable magmatic systems: a unified view of igneous processes. *Science*, *355*(6331), p. 3055.

Cooper and Kent, 2014

Duchêne, S., Pupier, E., De Veslud, C.L.C. and Toplis, M.J., 2008. A 3D reconstruction of plagioclase crystals in a synthetic basalt. *American Mineralogist*, *93*(5-6), pp.893-901.

Eichheimer, P., Thielmann, M., Fujita, W., Golabek, G.J., Nakamura, M., Okumura, S., Nakatani, T. and Kottwitz, M.O., 2020. Combined numerical and experimental study of microstructure and permeability in porous granular media. *Solid Earth*, *11*(3), pp.1079-1095.

Elam, W.T., Kerstein, A.R. and Rehr, J.J., 1984. Critical properties of the void percolation problem for spheres. *Physical review letters*, *52*(17), p.1516.

Feng, S., Halperin, B.I. and Sen, P.N., 1987. Transport properties of continuum systems near the percolation threshold. *Physical review B*, *35*(1), p.197.

Huang, H.H., Lin, F.C., Schmandt, B., Farrell, J., Smith, R.B. and Tsai, V.C., 2015. The Yellowstone magmatic system from the mantle plume to the upper crust. *Science*, *348*(6236), pp.773-776.

Humphreys, M.C., 2009. Chemical evolution of intercumulus liquid, as recorded in plagioclase overgrowth rims from the Skaergaard intrusion. *Journal of Petrology*, *50*(1), pp.127-145.

Jackson, M.D., Blundy, J. and Sparks, R.S.J., 2018. Chemical differentiation, cold storage and remobilization of magma in the Earth's crust. *Nature*, *564*(7736), pp.405-409.

Karakas, O., Degruyter, W., Bachmann, O. and Dufek, J., 2017. Lifetime and size of shallow magma bodies controlled by crustal-scale magmatism. *Nature Geoscience*, *10*(6), pp.446-450.

Kertesz, J., 1981. Percolation of holes between overlapping spheres: Monte Carlo calculation of the critical volume fraction. *Journal de Physique Lettres*, *42*(17), pp.393-395.

Liu, B. and Lee, C.T., 2021. Fast melt expulsion from crystal-rich mushes via induced anisotropic permeability. *Earth and Planetar*

Liu, T., Lin, B. and Yang, W., 2017. Impact of matrix–fracture interactions on coal permeability: model development and analysis. *Fuel*, *207*, pp.522-532.

Llewellin, E.W., 2010. LBflow: An extensible lattice Boltzmann framework for the simulation of geophysical flows. Part I: theory and implementation. *Computers & Geosciences*, *36*(2), pp.115-122.

Llewellin, E.W., 2010. LBflow: An extensible lattice Boltzmann framework for the simulation of geophysical flows. Part II: usage and validation. *Computers & geosciences*, *36*(2), pp.123-132.

Lorensen, W.E. and Cline, H.E., 1987. Marching cubes: A high resolution 3D surface construction algorithm. *ACM siggraph computer graphics*, *21*(4), pp.163-169.

Macente et al. (2022)

Martys, N.S., Torquato, S. and Bentz, D.P., 1994. Universal scaling of fluid permeability for sphere packings. *Physical Review E*, *50*(1), p.403.

Morse, S.A., 1998. Is the cumulate paradigm at risk?: an extended discussion of The cumulate paradigm reconsidered. *The Journal of geology*, *106*(3), pp.367-372.

Paulatto, M., Annen, C., Henstock, T.J., Kiddle, E., Minshull, T.A., Sparks, R.S.J. and Voight, B., 2012. Magma chamber properties from integrated seismic tomography and thermal modeling at Montserrat. *Geochemistry, Geophysics, Geosystems*, *13*(1).

Rabinowicz, M., Genthon, P., Ceuleneer, G. and Hillairet, M., 2001. Compaction in a mantle mush with high melt concentrations and the generation of magma chambers. *Earth and Planetary Science Letters*, *188*(3-4), pp.313-328.

Rintoul, M.D., 2000. Precise determination of the void percolation threshold for two distributions of overlapping spheres. *Physical Review E*, *62*(1), p.68.

Röding, M., Ma, Z. and Torquato, S., 2020. Predicting permeability via statistical learning on higher-order microstructural information. *Scientific reports*, *10*(1), pp.1-17.

Ryan, A.G., Heap, M.J., Russell, J.K., Kennedy, L.A. and Clynne, M.A., 2020. Cyclic shear zone cataclasis and sintering during lava dome extrusion: Insights from Chaos Crags, Lassen Volcanic Center (USA). *Journal of Volcanology and Geothermal Research*, *401*, p.106935.

Sangani, A.S. and Acrivos, A., 1982. Slow flow through a periodic array of spheres. *International Journal of Multiphase Flow*, *8*(4), pp.343-360.

Sparks, R.S.J., Annen, C., Blundy, J.D., Cashman, K.V., Rust, A.C. and Jackson, M.D., 2019. Formation and dynamics of magma reservoirs. *Philosophical Transactions of the Royal society A*, *377*(2139), p.20180019.

Torquato, S., 2013. *Random heterogeneous materials*. Springer

Vasseur, J. and Wadsworth, F.B., 2017. Sphere models for pore geometry and fluid permeability in heterogeneous magmas. *Bulletin of Volcanology*, *79*(11), pp.1-15.

Vasseur, J., Wadsworth, F.B., Coumans, J.P. and Dingwell, D.B., 2021. Permeability of packs of polydisperse hard spheres. *Physical Review E*, *103*(6), p.062613.

Vasseur, J., Wadsworth, F.B., Bretagne, E. and Dingwell, D.B., 2022. Universal scaling for the permeability of random packs of overlapping and nonoverlapping particles. *Physical Review E*, *105*(4), p.L043301.

Vasseur, J., Wadsworth, F.B. and Dingwell, D.B., 2020. Permeability of polydisperse magma foam. *Geology*, *48*(6), pp.536-540.

Wadsworth, F.B., Vasseur, J., Scheu, B., Kendrick, J.E., Lavallée, Y. and Dingwell, D.B., 2016. Universal scaling of fluid permeability during volcanic welding and sediment diagenesis. *Geology*, *44*(3), pp.219-222.

Wadsworth, F.B., Vasseur, J., Llewellin, E.W. and Dingwell, D.B., 2017. Sintering of polydisperse viscous droplets. *Physical Review E*, *95*(3), p.033114.

Wadsworth, F.B., Vasseur, J., Casas, A.S., Delmelle, P., Hess, K.U., Ayris, P.M. and Dingwell, D.B., 2021. A model for the kinetics of high-temperature reactions between polydisperse volcanic ash and SO2 gas. *American Mineralogist: Journal of Earth and Planetary Materials*, *106*(8), pp.1319-1332.

Wager, L.R., Brown, G.M. and Wadsworth, W.J., 1960. Types of igneous cumulates. *Journal of Petrology*, *1*(1), pp.73-85.

Table 1.3: raw data for the permeability of packs of overgrown cuboids

Growth step	side length [m]	Aspect ratio	Porosity	Specific surface area [m^{-1}]	Permeability X [m^2]	Permeability Y [m^2]	Permeability Z [m^2]
5	8.00E-05	0.2	0.0238	13886.03			
4	8.00E-05	0.2	0.0486	24976.05		8.6147E-16	
3	8.00E-05	0.2	0.0918	40826.67	6.89965E-15	6.92961E-15	3.5134E-15
2	8.00E-05	0.2	0.1588	59106.64	6.2089E-14	6.79549E-14	3.9218E-14
1	8.00E-05	0.2	0.2517	76533.15	2.78471E-13	3.15802E-13	1.926E-13
5	8.00E-05	0.2	0.0236	14059.83			
4	8.00E-05	0.2	0.0488	25111.06		1.75451E-16	
3	8.00E-05	0.2	0.0918	40319.77	3.32803E-15	8.10675E-15	2.86267E-15
2	8.00E-05	0.2	0.1583	58820.84	4.3346E-14	6.78688E-14	4.13649E-14
1	8.00E-05	0.2	0.2512	76662.32	2.48174E-13	3.2072E-13	2.34878E-13
5	6.00E-05	0.7	0.0177	12020.42			
4	6.00E-05	0.7	0.0392	21588.65		3.45758E-16	5.95155E-16
3	6.00E-05	0.7	0.0754	33763.52	4.83012E-15	9.63351E-15	1.14657E-14
2	6.00E-05	0.7	0.1295	47554.51	4.59926E-14	6.7278E-14	7.40098E-14
1	6.00E-05	0.7	0.2034	61656.24	2.16996E-13	2.74073E-13	2.97845E-13
5	6.00E-05	0.7	0.0183	11747.16			
4	6.00E-05	0.7	0.0394	21102.91			
3	6.00E-05	0.7	0.0752	33218.68	7.40023E-15	6.48506E-15	5.98419E-15
2	6.00E-05	0.7	0.1293	47280.19	6.67955E-14	5.36122E-14	5.10811E-14
1	6.00E-05	0.7	0.2035	61140.22	2.88758E-13	2.46893E-13	2.38544E-13
5	5.00E-05	1	0.0157	10912.29			
4	5.00E-05	1	0.0361	21123			
3	5.00E-05	1	0.0731	35101.71	8.40432E-15	4.3036E-15	3.38668E-15
2	5.00E-05	1	0.1314	51363.01	7.0146E-14	5.22738E-14	4.9928E-14
1	5.00E-05	1	0.2125	66444.82	3.09982E-13	2.59975E-13	2.52592E-13
5	5.00E-05	1	0.0172	11244.27			
4	5.00E-05	1	0.0379	21275.39			
3	5.00E-05	1	0.0749	34947.32	7.4615E-15	2.33788E-15	3.92629E-15
2	5.00E-05	1	0.1324	50653.93	6.24273E-14	3.72618E-14	4.6732E-14
1	5.00E-05	1	0.2127	66131.86	2.78071E-13	2.28138E-13	2.50694E-13
5	5.00E-05	1.5	0.025	13435.89			
4	5.00E-05	1.5	0.0484	22404.21			4.33507E-16
3	5.00E-05	1.5	0.0856	33568.73	8.33588E-15	8.20857E-15	1.17099E-14
2	5.00E-05	1.5	0.1395	46161.5	6.94238E-14	6.18442E-14	7.41733E-14
1	5.00E-05	1.5	0.2115	58406.84	2.9666E-13	2.71061E-13	2.96084E-13
5	5.00E-05	1.5	0.0244	13810.06			
4	5.00E-05	1.5	0.0481	23055.11	1.92871E-15	6.09031E-16	6.76573E-16
3	5.00E-05	1.5	0.0861	34585.36	1.66646E-14	1.39634E-14	1.43072E-14
2	5.00E-05	1.5	0.1408	46982.25	9.57557E-14	8.1732E-14	9.21212E-14

1	5.00E-05	1.5	0.2127	58753.63	3.54378E-13	3.07271E-13	3.45362E-13
5	4.00E-05	3	0.0334	16945.18		1.01717E-16	3.96178E-17
4	4.00E-05	3	0.0619	26717.02	2.49791E-15	3.57425E-15	2.88259E-15
3	4.00E-05	3	0.1053	38239.56	2.91839E-14	2.92526E-14	3.19512E-14
2	4.00E-05	3	0.1651	50125.82	1.38052E-13	1.40766E-13	1.512E-13
1	4.00E-05	3	0.242	61998.33	4.59359E-13	4.73799E-13	4.89336E-13
5	4.00E-05	3	0.0346	17308.36		8.52594E-17	2.05345E-16
4	4.00E-05	3	0.0635	26942.97	3.29596E-15	3.7395E-15	4.95301E-15
3	4.00E-05	3	0.1067	38251.27	3.07903E-14	3.47645E-14	3.57366E-14
2	4.00E-05	3	0.1664	50207.91	1.3568E-13	1.54015E-13	1.50788E-13
1	4.00E-05	3	0.2432	61776.83	4.4442E-13	4.94628E-13	4.99077E-13
5	3.00E-05	4	0.0212	13583.98			
4	3.00E-05	4	0.0454	24349.04	1.00253E-15	5.09671E-16	1.19916E-16
3	3.00E-05	4	0.0865	38553.62	1.28177E-14	9.31107E-15	7.36531E-15
2	3.00E-05	4	0.149	55168.53	7.91466E-14	6.75119E-14	6.27626E-14
1	3.00E-05	4	0.2359	72445.75	3.2739E-13	2.95994E-13	2.88352E-13
5	3.00E-05	4	0.0222	14198.43			
4	3.00E-05	4	0.0477	25736.6	4.50884E-16	2.17042E-16	4.14978E-16
3	3.00E-05	4	0.091	40437.68	1.3709E-14	9.44673E-15	9.93177E-15
2	3.00E-05	4	0.1563	57091.15	9.27668E-14	7.73726E-14	7.89016E-14
1	3.00E-05	4	0.2457	73703.76	3.73143E-13	3.32596E-13	3.44869E-13
5	3.00E-05	6	0.0422	20239.79			
4	3.00E-05	6	0.0759	31432.96	1.84471E-15	4.26107E-15	5.50123E-15
3	3.00E-05	6	0.1261	44247.54	2.74048E-14	3.58914E-14	5.45278E-14
2	3.00E-05	6	0.1946	57415.39	1.50676E-13	1.73106E-13	2.44731E-13
1	3.00E-05	6	0.2814	69331.38	5.29618E-13	5.94011E-13	7.66889E-13
5	3.00E-05	6	0.0425	20597.4			
4	3.00E-05	6	0.0768	31810.65	5.3158E-15	5.97056E-15	5.81544E-15
3	3.00E-05	6	0.1278	44685.55	4.4834E-14	5.34007E-14	4.69854E-14
2	3.00E-05	6	0.1973	57833.62	2.05317E-13	2.40562E-13	2.04311E-13
1	3.00E-05	6	0.2852	69572.68	6.63532E-13	7.71212E-13	6.47039E-13

Chapter 6 : General discussion and implications

The culmination of this thesis is to propose a universal scaling for permeability for any shape and for any melt fraction. The implication is that we can predict the permeability of any type of magma mush at any stage of crystallinity, which is a very powerful tool for constraining large and small-scale mush dynamics. Below we explore two wider implications of this work and tie together the findings outlined in this thesis.

6.1 Case studies of wider implications in the mush world

We suggest looking in more detail at two wider implications of the universal permeability model for magma mushes: (1) constraining the melt extraction timescales for melt-crystal segregation prior to eruption. And then at (2) using the percolation model to better understand the final mush textures that we see in the field and suggest a way of finding the percolation potential from final mush textures.

6.1.1. Melt extraction timescales in compacting mushes

(NB: This is to say, we do not believe that gravitational compaction is the sole driving force in melt segregation processes, however, this process potentially plays a key role and we use the principles of it here to highlight the importance of the accounting for the proper shape of the crystals)

Key outstanding problems are associated with constraining the timescales for melt extraction. The viscosity of hydrous melt stored between crystals in a mush is sufficiently high (10^4-10^5 Pa.s for silicic melt) to render extraction timescales by compaction, filter-pressing, or other percolative flow mechanisms long (up to 10^5 years, Shaw, 1975; McKenzie, 1984; Holness, 2018) compared with estimated cooling times of crustal mush bodies (thermal lifespan of mush ~10^5-10^6 years, Liu & Lee, 2020). Therefore, predictions show that in many cases mushes should freeze before the melt is extracted, contrary to the suggestion that melts are indeed extracted ahead of large silicic eruptions. Petrological and geochronological evidence suggests that melt extraction occurs in transient and episodic events rather than continuously over the thermal lifespan of the mush (e.g. Allan et al., 2013). Key proposed solutions to these problems all involve decreasing the predicted melt extraction times and include: (1) additional heat provided by mafic recharge magmas (e.g. Huang et al. 2015), or (2) applied directional stresses

(Clemens & Petford, 1999; Bachmann & Bergantz 2008; Holness 2018) resulting in anisotropic dilation of the mush (Liu & Lee, 2021).

In all cases, the rates of melt extraction are sensitive to the permeability of the crystal framework forming the mush (e.g. Bachmann & Bergantz, 2004), which in turn is controlled by the crystal shape, as we show herein. The simplest model for melt extraction is gravitational compaction (McKenzie, 2011; Liu & Lee, 2020), which, in 1D, is scaled by the Darcy percolation timescale $\lambda = \mu_f H/(k\nabla P)$ for which H is a characteristic length (e.g. the mush vertical half-thickness, assuming a uniform porosity; Liu & Lee, 2021). The flow is driven by gravity for which $\nabla P = \Delta\rho g$ with $\Delta\rho$ the density contrast between the melt and crystals, and g the acceleration due to gravity (e.g. Liu & Lee, 2021). The rate of decay of melt fraction by compactive processes – and equivalently the volume flux of melt from the mush – is then scaled as a Darcy flux $d(1-\phi)/dt \approx \lambda^{-1}$. Therefore, for typical input values, we can use our model to compute the melt extraction rate λ for a given crystal size and shape. The thickness of an eruptible melt layer is $\delta = H\phi_H$, where we use ϕ_H is the melt volume fraction that can be extracted (here we assume this is approximately $\phi_H \approx 1 - (\phi' - \phi_\tau)$ and that any further extraction would require deformation or reorganization of the crystal pack). We explore standard mush system inputs that range over $10^4 \leq \mu_f \leq 10^5$ Pa.s, $300 \leq \Delta\rho \leq 600$ kg.m^{-3} (Lesher & Spera, 2015), and $1 \leq a \leq 3$ mm, consistent with the range used previously for the same problem (Bachmann & Bergantz, 2004). Using these values, we find the maximum and minimum output λ for $H = 1$ km (i.e. a 2 km thick mush pile), and for $H = 3$ km (i.e. a 6 km thick mush pile; Figure 6.5).

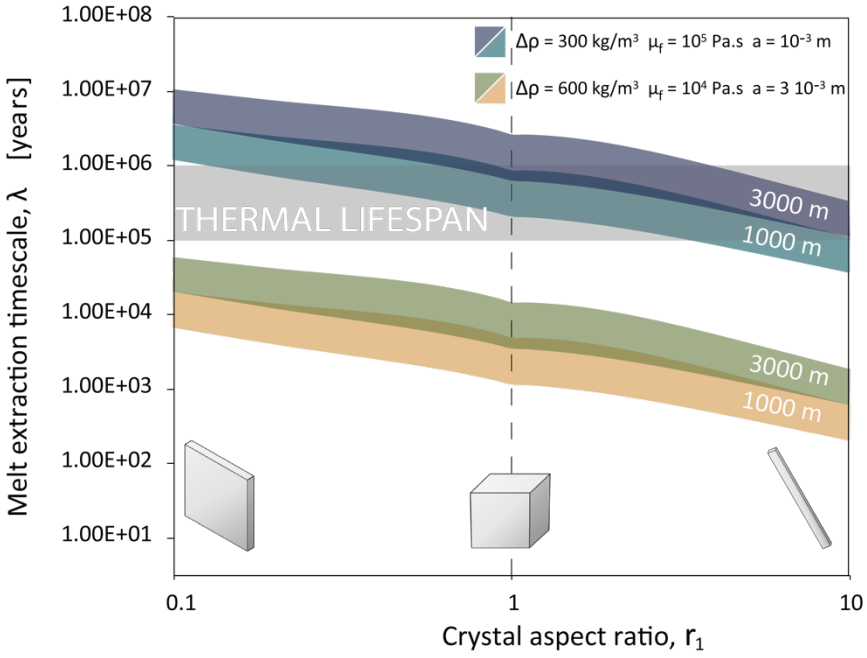

Figure 6.5: Calculated melt extraction timescales λ by compaction of a mush layer for mush of different crystal textures (captured by r_1). For each coloured region (i.e. set of conditions), the upper bounds of the domains are defined by the maximum random packing fraction ϕ' while the lower bound represents a loose mush ϕ_τ. For comparison, the maximum 'thermal lifespan' for a mush is approximately 10^5-10^6 years (Allan et al., 2013).

Our results show that melt extraction timescales for a mush composed of oblate (platy) crystals can be up to 1.5 orders of magnitude longer than for a mush made of prolate (needle-like) crystals (Figure 6.5). Using our shape-sensitive permeability model, we additionally find that mush with $\Delta\rho = 300$ kg. m^{-3}, $\mu_f = 10^5$ Pa. s, and $a = 1$ mm highly oblate crystals ($r_1 = 7 - 10$) can have melt extraction times that exceed the thermal lifetime. By contrast, for $\Delta\rho = 600$ kg. m^{-3}, $\mu_f = 10^4$ Pa. s, and $a = 1$ mm the melt extraction timescales are more rapid than the expected thermal lifespan for all r_1. Contrary to McKenzie (2011), our resulting timescales are still long compared with melt segregation timescales for natural systems (e.g. Allan et al., 2013), and other processes such as thermal rejuvenation shear strain are probably key (Holness, 2018; Wiebe et al 2004; Bachmann & Bergantz, 2003). Regardless of the processes involved, our results suggest that crystal shape plays a first-order role in melt extraction because the timescales involved are proportional to permeability $\lambda \propto k^{-1}$.

Jackson et al. (2018) have suggested that reactions between crystal frameworks and a buoyant percolating melt may be a central process for the differentiation of silicic magmas. Mush

permeability exerts a first order control over the rates of this process, and hence crystal shape effects need to be accounted for.

6.1.2. Link between percolation regime and final textures of crystallised mush

The mush textures that we can observe in the finished igneous product (i.e. when the mush is entirely crystallised) depend for the most part on whether the melt can percolate around the cumulate crystals that form the solid framework of the mush. Humphreys (2009) and Wager et al. (1960) acknowledge that the melt convection potential will depend on the physical properties of the melt, such as the viscosity and density, and the permeability of the mush crystal framework. We show in Chapter 5 that the percolation is controlled by the connectivity of the mush and, importantly, the percolation threshold.

Mush textures can be classified into two idealised endmembers of cumulus crystallisation (Wager, 1960; McBirney and Hunter, 1995; Grant and Chalokwu, 1998; Morse, 1998): (1) adcumulate textures characterised by constant re-equilibration of the interstitial melt composition with the wider reservoir and necessitates a high connectivity of the melt fraction for to maintain compositional convection (e.g. Kerr and Tait, 1986, Tait and Jaupart, 1992). The resulting textures are unzoned overgrowth rims on existing cumulate crystals (c.f. Figure 6.6b). At the opposite end of the spectrum is (2) the orthocumulate texture which corresponds to the *in-situ* crystallisation of melt trapped between the cumulate crystals with no chemical or physical exchange with the wider mush reservoir (e.g. Wager et al., 1960; Morse 1998). This results in the growth of inter-cumulus crystals that fill the space occupied by the interstitial melt (c.f. Figure 6.6c).

This classification is based solely on the melt percolation potential and the connectivity of the melt phase. It does not, however, consider the crystallisation and melt transport as dynamic processes. This implies that outside forcing (i.e. not intrinsic to the mush) could effectively affect the percolation potential of the crystal framework without changing the intrinsic properties of the mush (i.e. the permeability and percolation threshold). To that effect, we introduce the notion of the Darcy timescale $\lambda_D = (\mu_f L/k)\,\nabla P$ as the time, λ_D, a melt of a certain viscosity, μ_f, would take to travel a fixed distance L under a pressure gradient ∇P in a mush of permeability k (Heap and Wadsworth, 2016). We also introduce the notion of a competing timescale, the crystallisation timescale, λ_x.

We highlight two scenarios of the competing timescales, where the pressure gradient can be induced by external forcing, or a volume change due to the crystallisation process that creates a melt flux (Figure 6.6a). In the first scenario, the crystallisation process is longer than the melt percolation timescale $\lambda_D < \lambda_x$, consequently, the melt is able to flow around the cumulate phase and we get adcumulate type textures (Figure 6.6b). The second scenario is defined by crystallisation being quicker than the Darcy time for the melt, $\lambda_D < \lambda_x$. This implies that the interstitial melt does not move fast enough before it is trapped by crystallisation, consequently, the mush behaves in an impermeable manner, despite a high connectivity of the melt fraction. The second scenario is linked to orthocumulate textures where the interstitial melt crystallises *in situ* (Figure 6.6c).

While we can efficiently predict the mush type of textures that will crystallise if we know the permeability of the mush, the opposite work is more tricky. Crystallised mush the textures can tell us a lot about the mush's history, but we need to account for the dynamic timescales that control the percolating of the melt, lest one draws the wrong conclusions from the textural analysis.

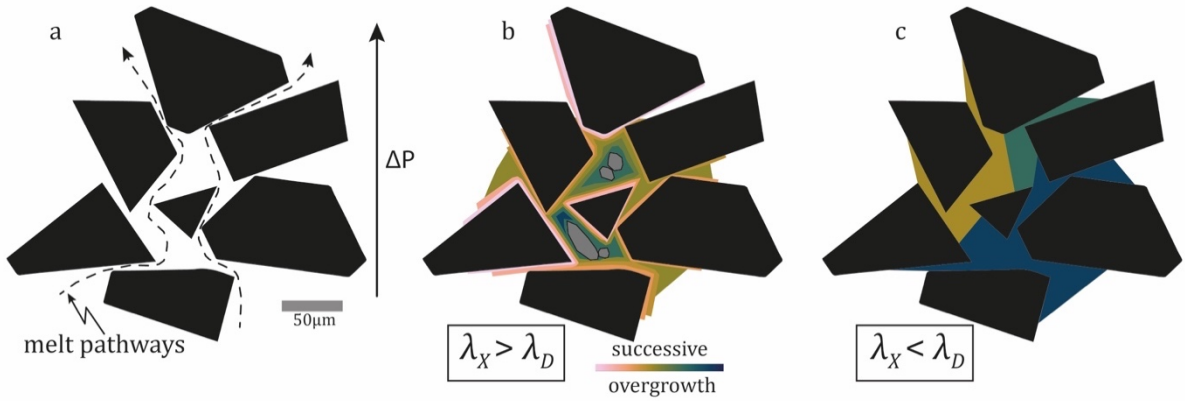

Figure 6.6: cartoon mush growth scenarios depending on the dominant time scale: a) initial mush at maximum packing fraction ϕ', represented here by the square-edged cuboids in the numerical packs. The flow pathways are highlighted with dashed arrows as the pressure gradient is $\nabla P \neq 0$; b) scenario where the crystallisation timescale λ_x is larger than the Darcy time for melt mobilisation, λ_D and crystallisation consists of overgrowths on the initial crystal shapes, here represented by the colourful overgrowths. We also add crystallisation of accessory phases in the melt pockets (grey shapes); c) this cartoon shows the scenario where the crystallisation timescale λ_x is shorter than the time for the melt to leave the cumulate crystal framework λ_D, hence the mush behaves as an impermeable medium. The interstitial melt crystallises in place as intercumulate phases (here represented but the colourful areas in-between the crystals)

References

Allan, A.S.R., Morgan, D.J., Wilson, C.J.N. and Millet, M.A., 2013. From mush to eruption in centuries: assembly of the super-sized Oruanui magma body. *Contributions to Mineralogy and Petrology*, *166*(1), pp.143-164.

Bachmann, O. and Bergantz, G.W., 2008. Rhyolites and their source mushes across tectonic settings. *Journal of Petrology*, *49*(12), pp.2277-2285.

Bachmann, O. and Bergantz, G.W., 2004. On the origin of crystal-poor rhyolites: extracted from batholithic crystal mushes. *Journal of Petrology*, *45*(8), pp.1565-1582.

Bachmann, O. and Bergantz, G.W., 2003. Rejuvenation of the Fish Canyon magma body: A window into the evolution of large-volume silicic magma systems. *Geology*, *31*(9), pp.789-792.

Clemens, J.D. and Petford, N., 1999. Granitic melt viscosity and silicic magma dynamics in contrasting tectonic settings. *Journal of the Geological Society*, *156*(6), pp.1057-1060.

Grant, N.K. and Chalokwu, C.I., 1998. The cumulate paradigm affirmed. *The Journal of geology*, *106*(5), pp.641-644.

Heap, M.J. and Wadsworth, F.B., 2016. Closing an open system: pore pressure changes in permeable edifice rock at high strain rates. *Journal of Volcanology and Geothermal Research*, *315*, pp.40-50.

Holness, M.B., 2018. Melt segregation from silicic crystal mushes: a critical appraisal of possible mechanisms and their microstructural record. *Contributions to Mineralogy and Petrology*, *173*(6), pp.1-17.

Huang, H.H., Lin, F.C., Schmandt, B., Farrell, J., Smith, R.B. and Tsai, V.C., 2015. The Yellowstone magmatic system from the mantle plume to the upper crust. *Science*, *348*(6236), pp.773-776.

Humphreys, M.C., 2009. Chemical evolution of intercumulus liquid, as recorded in plagioclase overgrowth rims from the Skaergaard intrusion. *Journal of Petrology*, *50*(1), pp.127-145.

Jackson, M.D., Blundy, J. and Sparks, R.S.J., 2018. Chemical differentiation, cold storage and remobilization of magma in the Earth's crust. *Nature*, *564*(7736), pp.405-409.

Kerr, R.C. and Tait, S.R., 1986. Crystallization and compositional convection in a porous medium with application to layered igneous intrusions. *Journal of Geophysical Research: Solid Earth*, *91*(B3), pp.3591-3608

Lesher, C.E. and Spera, F.J., 2015. Thermodynamic and transport properties of silicate melts and magma. In *The encyclopedia of volcanoes* (pp. 113-141). Academic Press.

Liu, B. and Lee, C.T., 2021. Fast melt expulsion from crystal-rich mushes via induced anisotropic permeability. *Earth and Planetary Science Letters*, *571*, p.117113.

Liu, B. and Lee, C.T., 2020. Large silicic eruptions, episodic recharge, and the transcrustal magmatic system. *Geochemistry, Geophysics, Geosystems*, *21*(9), p.e2020GC009220.

McBirney, A.R. and Hunter, R.H., 1995. The cumulate paradigm reconsidered. *The journal of Geology*, *103*(1), pp.114-122.

McKenzie, D., 2011. Compaction and crystallization in magma chambers: towards a model of the Skaergaard intrusion. *Journal of Petrology*, *52*(5), pp.905-930.

McKenzie, D., 1984. The generation and compaction of partially molten rock. *Journal of petrology*, *25*(3), pp.713-765.

Morse, S.A., 1998. Is the cumulate paradigm at risk?: an extended discussion of The cumulate paradigm reconsidered. *The Journal of geology*, *106*(3), pp.367-372.

Shaw, H.R., 1985. Links between magma-tectonic rate balances, plutonism, and volcanism. *Journal of Geophysical Research: Solid Earth*, *90*(B13), pp.11275-11288.

Tait, S.R. and Jaupart, C., 1992. Convection and macrosegregation in magma chambers. In *Interactive Dynamics of convection and solidification* (pp. 241-260). Springer, Dordrecht.

Wager, L.R., Brown, G.M. and Wadsworth, W.J., 1960. Types of igneous cumulates. *Journal of Petrology*, *1*(1), pp.73-85.

Wiebe, R.A., Manon, M.R., Hawkins, D.P. and McDonough, W.F., 2004. Late-stage mafic injection and thermal rejuvenation of the Vinalhaven granite, coastal Maine. *Journal of Petrology*, *45*(11), pp.2133-2153.

Chapter 7 : Conclusions and further work

7.1 Conclusions

1. Crystal shape, expressed as the aspect ratio, exerts a first order control on both the permeability of a mush and the melt fraction at maximum packing density of the cumulate crystals.
2. We generalise the Kozeny-Carman permeability law for a better shape descriptor and validate the new model for magma mush, using numerical packs of cuboids as an analogue for crystal mush.
3. The permeability model is validated for anisotropic shapes of natural crystal mush, using confectionary cake toppings as mush analogues
4. Anisotropic crystal shapes are well approximated by cuboids, the shape of which is defined by the three orthogonal axes, either measured in 3D (ct scan) or in 2D (thin section)
5. The permeability of a mature mush that displays overgrowth textures and is characterised by low melt fractions is controlled by the percolation threshold of the mush
6. In a mature mush (i.e.at low melt fractions), the initial shape of the crystals in the mush are hidden beneath layers of overgrowth and become irrelevant for the permeability predictions
7. We propose a universal scaling law for the permeability of a magma mush composed of crystals of any shape and spanning the entire melt fraction range, i.e. from a melt dominated mush to an entirely crystallised mush. In the case that the specific surface area cannot be measured, the crystals can be approximated to cuboids whose principal axes can either be measured from a 3D scan of the rock or a thin section and then projected with the appropriate software. The following table (Table 7.1) is meant for users of the permeability model, providing details of which model to use depending on the melt fraction and the data available, i.e. whether the user has 3D data available or not.

Table 7.1: User table for permeability model depending on the melt fraction and data available to user. k_r is defined as $k_r = 2\big(1-(\phi_m-\phi_c)\big)/s^2$. For all cases, it is necessary to know the melt fraction. ShapeCalc is a 3D shape converter available from Mangler et al. (2022)

Melt fraction range, ϕ_m	Specific surface area s is known	Specific surface area s is not known, 3D shape data available a, b, c such that $r_1 = c/a, r_2 = b/a$	Specific surface area s is not known, 2D shape data available l_i, w_i
$\phi_m \gtrsim 0.4$	$k = k_r\left(\sum_{i=0}^{30} c_i \left(\frac{\phi}{1-\phi'}\right)^{\frac{i}{3}}\right)^{-1}$	Substitute for s $s = \frac{2(1-\phi_m)}{a}\left(1+\frac{1}{r_1}+\frac{1}{r_2}\right)$	Input measured l_i, w_i into ShapeCalc, output s, i, l, convert using: $a \approx w_i$ $b = i\, w_i$ $c = l\, w_i$
$0.2 \lesssim \phi_m \lesssim 0.4$	$k = \frac{{\phi_m}^3}{Cs^2}$		
$\phi_m \lesssim 0.2$	$k = k_r(\phi_m - \phi_c)^y$	$s = -\frac{3\,\phi\ln(\phi)}{a}\left(1+\frac{1}{r_1}+\frac{1}{r_2}\right)$	

7.2 Future work: going beyond the scope of this thesis

1. We have proposed a universal scaling for permeability which is validated for numerical simulations. A further work idea would be to test the validity of our findings using analogue modelling at laboratory scale. We would test the permeability of packs of spherical beads and then, graduate to more complex shapes. It could be interesting to introduce anisotropy in the "crystal" pile in the form of a layer of different crystal shapes or of a different material.
2. In this thesis, we consider the crystals in the mush immobile with melt flowing around them. This is however not always true, and cumulate crystals are commonly displaced by dynamic movement in the mush reservoir. Schleicher et al. (2016) have studied the textures that are created from basal intrusion of magma into a mush layer and find that the percolation-crystal entrainment boundary is sensitive to the permeability. An application of our permeability model could be to further map the evolution of textures in the mush layer using analogue materials at laboratory scale.

3. In this work we study the mobilisation of crystal poor material (i.e. mobilisation of melt only) but there is a lot of work yet still to do on wholescale mobilisation of mush. One avenue of exploration would be the influence of gas exsolution in the melt and subsequent bubble growth on the bulk viscosity of the mush and its effective mobility.

References

Mangler, M.F., Humphreys, M.C., Wadsworth, F.B., Iveson, A.A. and Higgins, M.D., 2022. Variation of plagioclase shape with size in intermediate magmas: a window into incipient plagioclase crystallisation. *Contributions to Mineralogy and Petrology*, *177*(6), p.64.

Schleicher, J.M., Bergantz, G.W., Breidenthal, R.E. and Burgisser, A., 2016. Time scales of crystal mixing in magma mushes. *Geophysical Research Letters*, *43*(4), pp.1543-1550.

Chapter 8 Appendices

Appendix 1

DATA REPOSITORY

This data repository is composed of the following sections:

(1) The conditions of the numerical flow experiments;
(2) The derivation of the specific surface area for a pack of cuboids;
(3) Considerations of anisotropy;
(4) An assessment of the resolution and node distribution in the fluid spaces;
(5) The raw data unique to this manuscript and required to reproduce the results.

1. Using LB flow to simulate fluid flow through numerical volumes

In order to determine permeability we use the *LBflow* lattice-Boltzmann fluid flow simulator (Llewellin, 2010a; 2010b), which has been calibrated over a wide range of porosity against explicit models for the permeability of body-centered cubic (Llewellin, 2010b) and simple cubic (Wadsworth et al. 2017) packs of spheres. The *LBflow* model takes the segmented pore phase in the total domain as an input and discretizes the pore phase into a lattice of fluid nodes (one fluid node per voxel). Fluid mass parcels are numerically propagated through the lattice positions with time and the result of collisions are computed on a D_3Q_{15} lattice. In this framework, we apply a numerical pressure gradient of $\nabla p = 0.01$ Pa. m^{-1} using a pore fluid with viscosity $\mu_f = 1.8205 \times 10^{-5}$ Pa. s and density $\rho_f = 1.2047$ kg. m^{-3}, corresponding to air at ambient conditions. The simulation converges at steady state flow determined via a criterion that the average fluid speed across the lattice not vary by more than a 10^{-5} factor over 50 iterations twice. In all fluid flow simulations, we use a sub-domain with edge length L, placed within the full domain, and we keep the spatial position of this sub-domain fixed throughout the back-stripping process.

The result of the *LBflow* algorithm is the spatial distribution of fluid velocities at steady state, u. The average fluid velocity in the direction of the applied pressure gradient is given by $\langle u \rangle = \phi_t u$, where ϕ_t is the porosity. The output $\langle u \rangle$ can be used as an input to Darcy's law to determine the permeability k in a given direction via $k = -\nabla p \mu_f / \langle u \rangle$. Importantly, the input properties μ_f and ρ_f and condition ∇p are all checked to ensure that the flow is in the creeping low-Reynolds number regime and low-Mach number regime and therefore the result is insensitive to our choice of μ_f and ρ_f. The Reynolds number is given by $\mathrm{Re} = \rho_f L \langle u \rangle / \mu_f$ and the Mach number is given by $\mathrm{Ma} = \langle u \rangle / c$ where L is the domain edge length and c is the speed of sound in the fluid medium. We find that $10^{-8} \leq \mathrm{Re} \leq 10^{-5}$ and $10^{-12} \leq \mathrm{Ma} \leq 10^{-9}$; regimes in which Darcy's law is valid and in which k does not depend on the fluid properties chosen. This workflow is repeated for each domain and in each principal direction.

1. The specific surface area of a cuboid pack

A cuboid has 3 axes, a, b, and c. First, if we take $a = b$, then the we have the aspect ratio of the cuboid $r_1 = c/a$. The surface area A_c and volume V_c of a single cuboid is then

$$A_c = 2a^2 + 4r_1a^2 = 2a^2(1 + 2r_1)$$
$$V_c = r_1a^3. \quad \text{Eq. S1}$$

The number of cuboids in a pack of cuboids is n and so the cumulative surface area and volume of the cuboids are $A = nA_c$ and $V = nV_c$. The cuboid volume fraction ϕ is the ratio of V to the total system volume V_T, so that $V_T = nr_1a^3/\phi$. The specific surface area s is the ratio of the surface area to the total volume $s = A/V_T$ so that

$$s = \frac{n\phi 2a^2(1 + 2r_1)}{nr_1a^3} = \frac{2\phi}{a}\left(2 + \frac{1}{r_1}\right). \quad \text{Eq. S2}$$

Second, if we take a, b and c to be independent values, then we have two possible aspect ratios $r_1 = c/a$ and $r_2 = b/a$. And following the approach given above, we find

$$s = \frac{2\phi}{a}\left(1 + \frac{1}{r_1} + \frac{1}{r_2}\right) \quad \text{Eq. S3}$$

which reduces to Eq. S2 when $r_1 = r_2$, which is the case when $a = b$. To be general, and to be able to compare systems of any size, Eq. S3 suggests that the natural scaling factor for s is $1/a$, so that a dimensionless specific surface area is $\bar{s} = sa/\phi$, which makes Eq. S3

$$\bar{s} = 2\left(1 + \frac{1}{r_1} + \frac{1}{r_2}\right). \quad \text{Eq. S4}$$

An equivalent to Eq. S3 for the situation where we only use the 3 axes directly is given by the following identities

$$A_c = 2ab + 2ac + 2bc$$
$$V_c = abc$$
$$V_T = \frac{nabc}{\phi} \quad \text{Eq. S4}$$
$$A = 2n(ab + ac + ad)$$
$$s = \frac{2\phi n(ab + ac + ad)}{nabc} = 2\phi\left(\frac{1}{a} + \frac{1}{b} + \frac{1}{c}\right)$$

2. Anisotropy

Permeability is a tensor quantity. However, in this contribution we make an assumption that we can approximate the permeability as a scalar quantity, equivalent to assuming that the off-diagonal components of the tensor are zero and the diagonal components are all equal (i.e. the permeability in the x Cartesian direction is the same as in y and z). This is consistent with the origin of the data we use (Liu et al. 2017) for which statistical isotropy is confirmed in their simulations (and therefore in the data we present herein too). However, in nature, anisotropy is

possible (Liu & Lee 2021). Therefore, there is an opportunity for future work to extend our results to anisotropic systems and to explore the magnitude of the intrinsic error in our scalar approximation (c.f. Lang et al. 2014). Full dynamic models for mush evolution are likely to solve for the fabric development as a function of the stresses acting on the mush. However, in the majority of scaling approaches and models that solve for compaction or percolation through mush, a single permeability value must be attributed to the mush as a whole, and therefore our approach serves this purpose.

3. Fluid node spacings in the pore space and the accuracy of LBflow permeability determinations

When using lattice-Boltzmann techniques, it is important to consider the effects of boundaries, especially in tight pore spaces. Here we render the pore space (solid phase is invisible) for some small sub-domains of the total domain, effectively 'zooming in' on the pore spaces. This is to make a qualitative assessment of the pore space resolution in the gaps between cuboids. The apparent roughness on the cuboid-pore walls (the flat surfaces in the visualisation below) can be used to make a visual assessment of the number of voxels in each pore space gap. In all cases, the vast majority of pore spaces have >6 voxels from edge-to-edge (i.e. from cuboid to cuboid). The LBflow algorithm places one fluid node per voxel, and so this is a direct assessment of the resolution used here. We note that this density of fluid nodes is similar or greater to those used previously to compare LBflow outputs with direct calculations of fluid permeability using derived analytical expressions (for simple cubic sphere packs, Wadsworth et al. 2017; for body-centred cubic sphere packs, Llewellin 2010b).

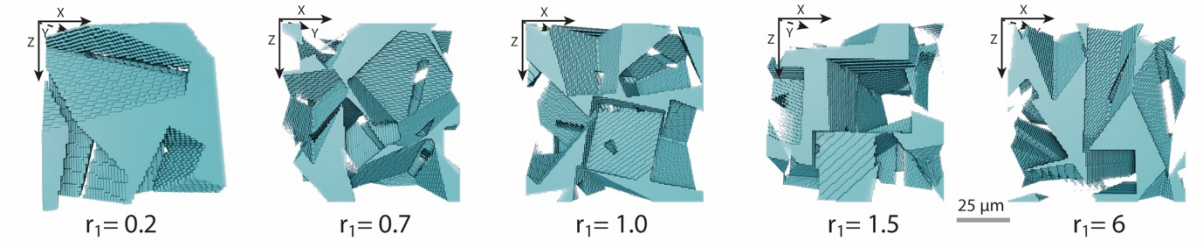

4. Raw data for simulations presented here

Melt fraction, 1-ϕ	Axis length, a [m]	Aspect ratio, r_1	Specific surface area, s [m^{-1}]
0.5917	0.00029	0.2	26804.54
0.5934	0.00029	0.2	26702.68
0.5896	0.00029	0.2	26176.84
0.593	0.00029	0.2	26123.4
0.588	0.00029	0.2	26427.92
0.6227	0.00026	0.3	24846.34
0.626	0.00026	0.3	24390.79
0.6296	0.00026	0.3	24688.47
0.6243	0.00026	0.3	24396.67
0.6282	0.00026	0.3	24893.31
0.6464	0.00024	0.4	23959.45
0.6427	0.00024	0.4	23985.76
0.6463	0.00024	0.4	23919.94
0.6462	0.00024	0.4	23818.73
0.6444	0.00024	0.4	24010.97
0.6595	0.00022	0.5	23709.64
0.6616	0.00022	0.5	24101.44
0.6637	0.00022	0.5	24061.13

0.66	0.00022	0.5	24438.85
0.6616	0.00022	0.5	23868.81
0.668	0.00021	0.6	23530.06
0.6681	0.00021	0.6	23445.55
0.6661	0.00021	0.6	23598.85
0.6679	0.00021	0.6	23277.5
0.6679	0.00021	0.6	23336.88
0.6691	0.0002	0.7	23464.5
0.671	0.0002	0.7	23284.91
0.6752	0.0002	0.7	23655.54
0.6689	0.0002	0.7	23006.78
0.6712	0.0002	0.7	23425.48
0.6693	0.00019	0.8	23378.28
0.6674	0.00019	0.8	23371.65
0.6694	0.00019	0.8	23616.05
0.6675	0.00019	0.8	23670.5
0.6695	0.00019	0.8	23569.29
0.6579	0.00018	0.9	23612.58
0.6617	0.00018	0.9	23832.72
0.6617	0.00018	0.9	23364.1
0.6556	0.00018	0.9	23146.85
0.6618	0.00018	0.9	23710.59
0.6536	0.00018	1	22601.68
0.6535	0.00018	1	22555.47
0.6517	0.00018	1	22558.26
0.657	0.00018	1	22332.68
0.6534	0.00018	1	22235.31
0.6573	0.00017	1.1	23389.96
0.6612	0.00017	1.1	23548.29
0.6575	0.00017	1.1	23403.56
0.6594	0.00017	1.1	23342.4
0.6594	0.00017	1.1	23238.91
0.6643	0.00017	1.2	22799.75
0.6664	0.00017	1.2	23334.1
0.6625	0.00017	1.2	22602.04
0.6645	0.00017	1.2	22979.36
0.6644	0.00017	1.2	22905.02
0.6693	0.00016	1.3	23722.93
0.6715	0.00016	1.3	23903.1
0.6652	0.00016	1.3	23543.64
0.6674	0.00016	1.3	23803.58
0.6692	0.00016	1.3	23677.48
0.6691	0.00016	1.4	23057.93
0.6713	0.00016	1.4	23277.48

0.6711	0.00016	1.4	23177.38
0.6673	0.00016	1.4	23287.64
0.6693	0.00016	1.4	23402.21
0.6727	0.00016	1.5	22619.62
0.6707	0.00016	1.5	22673.01
0.6708	0.00016	1.5	22552.95
0.6671	0.00016	1.5	22573.76
0.6688	0.00016	1.5	22506.85
0.6688	0.00015	1.6	23710.01
0.6669	0.00015	1.6	23933.65
0.6667	0.00015	1.6	23522.58
0.6669	0.00015	1.6	23757.86
0.6689	0.00015	1.6	23836.58
0.6678	0.00015	1.7	23524.46
0.6641	0.00015	1.7	23443.65
0.6659	0.00015	1.7	23310.84
0.6676	0.00015	1.7	23115.92
0.6659	0.00015	1.7	23325.53
0.6596	0.00015	1.8	22437.11
0.6616	0.00015	1.8	22884.51
0.6617	0.00015	1.8	22923.74
0.6634	0.00015	1.8	22714.06
0.6653	0.00015	1.8	22763.76
0.6618	0.00014	1.9	24281.55
0.6596	0.00014	1.9	24012.12
0.6598	0.00014	1.9	24095.88
0.6618	0.00014	1.9	24325.65
0.6578	0.00014	1.9	24149.33
0.6583	0.00014	2	23682.79
0.6584	0.00014	2	24115.84
0.658	0.00014	2	23650.22
0.658	0.00014	2	23497.29
0.6583	0.00014	2	23924.37
0.636	0.00012	3	25396.36
0.634	0.00012	3	25012.45
0.634	0.00012	3	25139.42
0.6338	0.00012	3	24730.88
0.6304	0.00012	3	25035.96
0.6145	0.00011	4	24935.15
0.6061	0.00011	4	25304.26
0.6147	0.00011	4	25125.83
0.613	0.00011	4	25189.52
0.6111	0.00011	4	25095.4
0.6024	0.0001	5	26511.89

0.6007	0.0001	5	26486.68
0.5987	0.0001	5	26031.53
0.5989	0.0001	5	26201.63
0.6008	0.0001	5	26787.93
0.5822	0.0001	6	24743.51
0.5778	0.0001	6	25007.88
0.5793	0.0001	6	24875.88
0.5779	0.0001	6	25013.13
0.5812	0.0001	6	25248.25